Molecular dynamics study of water and carbon dioxide separation by means of nanotubes

A new method to capture CO2

Master thesis in Process Technology

Department of Physics and Technology
University of Bergen, Norway

August 2018

Sjur Sato Fimreite

“That's when I said:
Wow, engineering lets you
build things that solve problems”
- Steve Wozniak

Abstract

Anthropogenic carbon dioxide (CO2) emissions are a huge concern these days. Arguably, but widely accepted, the apparent global climate changes are due to the increasing CO2 concentrations in the atmosphere. Carbon dioxide released into the atmosphere from combustion of fossil fuel (coal, oil and gas) can impact both local and global climate significantly. New technological solutions to capture the CO2 which are more energy efficient and less costly are necessary to mitigate the CO2 emissions.

Substantial amount of CO2 can be distributed into water by high-shear hydrodynamic forces generated, for instance, by venture nozzles. In this process, supercritical components in flue gas, like nitrogen and oxygen, will easily be flushed off from the water/CO2 mix. Nanotube filtering of the remaining water/CO2 mix is an interesting alternative to conventional CO2 capture technology since water needs substantial space in order to arrange large hydrogen bonded network. This space is not available in small nanotubes. In this research project, molecular dynamics simulation of modelled systems is utilized to investigate separation of an inhomogeneous system of water and CO2 through nanotube filtering (separation). In order to accomplish this, a non-uniform system consisting of a container with aqueous water-CO2 mixture connected with a nanotube to a receiving tank with initially pure CO2 gas is modelled. This non-equilibrium system is thermostatted with a same reference temperature for both containers. The basic idea of the non-equilibrium system set-up is that the thermodynamic driving forces related to mechanical work and chemical work in the free energy for nanotube plus receiving tank will approach zero as quasi-equilibrium conditions are reached. At this stage, the pressure at the end of the nanotube and the receiving tank will be the same and the chemical potential for CO2 at the end of nanotube and tank will be equal. In addition of being a method for calculating chemical potential for CO2 in the nanotube, this setup is utilized to investigate capacity (flux) and selectivity for CO2 through the nanotubes.

The new method to capture CO2 that will be presented in this master is based on separating the CO2 with carbon nanotubes from a non-equilibrium water-CO2 mixture (super-high concentrations of CO2 initially distributed in water). The simulations conducted in this research project are divided into two parts. In the first part, the selectivity and risk of water entrainment are evaluated as a function of nanotube size and initial pressure gradient across the nanotube. The second part uses a more idealized simulation system to evaluate the capacity of the nanotubes. The capacity of the nanotubes is quantified by CO2 flux through the nanotube as well as introducing an approach (briefly described above) that will be used to estimate the chemical potential of CO2 in the nanotube as a function of nanotube size and driving forces in the water-CO2

mixture container.

By analysis of the simulation results in part 1, this new method to capture CO2 showed promising results with good CO2 selectivity and low water risk under the constraints of the simulation system. The CO2 molecules had a strong preference relative to water to be separated from the inhomogeneous water-CO2 mixture with adsorption into the non-polar carbon nanotube. The good CO2 selectivity was found to be highly governed by strong water-water hydrogen bonding network interactions, strong CO2-nanotube interactions and a high excess CO2 concentration in water bulk. By increasing the initial pressure (by reducing the initial volume of the water-CO2 mixture), the result was a higher flux of CO2 into the nanotube, but also a higher risk of water entrainment, but still, the water was highly discriminated by the nanotube.

In part 2, it was found that a large increase in the thermodynamic driving forces resulted in a much higher flux through the nanotube as well as a dramatically higher number of CO2 molecules in the receiving tank. This is a very encouraging result because it shows the high potential (with high flux) of nanotube for the separation process if there is a high-density region of CO2 in the water-CO2 mixture near the nanotube entrance. A simulation system was successfully designed to give a first time ever estimation of the chemical potential of CO2 in the nanotube under the constraints of the system.

In both part 1 and 2, two 6 nm long nanotubes were investigated. That is: a (10,10) nanotube (1.3 nm in diameter) and a (20,20) nanotube (2.5 nm in diameter). Due to the small margin in the results and the constraints of the system, the results cannot be used to conclude which nanotube size that resulted in the best CO2 selectivity and flux through the nanotube. However, in part 2, the (20,20) nanotube yielded a much faster CO2 flux the first ~5 ns of simulation, but in the end, both nanotubes ended up with about the same amount of CO2 molecules passing through the nanotube for the same driving force conditions.

Acknowledgements

I would like to express my sincere gratitude to my supervisor professor Bjørn Kvamme for his guidance with my master thesis and for letting me work on this research project. He has very much knowledge in this field of science. He always had time for a meeting to discuss the project, even though his time schedule is quite busy.

A large gratitude to professor Tatiana Kuznetsova for her guidance, her critical thinking and for our discussions of the simulation results.

Thanks to researcher Bjørnar Jensen and PhD student Juri Selvåg for our discussions about molecules dynamics simulations and for their advices on this topic.

Furthermore, thanks to Petter Gjerstad for our enjoyable master student office environment.

Contents

Abbreviations

CNT	Carbon Nanotube
MD	Molecular Dynamics
MC	Monte Carlo
CO2	Carbon dioxide
H2O	Water
H2S	Hydrogen sulfide
CO	Carbon monoxide
EOR	Enhanced Oil Recovery
nm	nano meters (1 nm = 10^{-9} m)
Å	Ångstrom meters (1 Å = 10^{-10} m)
ns	nano seconds (1 ns = 10^{-9} s)
fs	femto seconds (1 fs = 10^{-15} s)
P	pressure
T	temperature
μ	chemical potential
ρ	density
G	Gibbs free energy
A	Helmholtz free energy
S	entropy
H	enthalpy
N_{CO2}	number of CO2 molecules
N_{water}	number of water molecules
V	volume
EoS	Equation of State
EPM2	Elementary Physical CO2 Model 2
SPCFw	Simple Point Charge Flexible Water Model

1 Introduction

1.1 Background

The world is experiencing an increasing global energy demand. In 2017, the global energy demand increased by 2.1% and 76% of that increase was covered by fossil fuel energy resources [1]. In the last decade, there has been a large appearance of new technological innovations and investments in renewable energy resources. Renewable energy resources are likely to be the leading energy resource in the future with an upcoming global energy transition, but for now, fossil fuels are still the highest demanded commodity in the global energy market, according to *BP Statistical Review of World Energy 2017* [2-4].

Oil and gas are produced from underground petroleum reservoirs. The crude oil and natural gas are then transported to a refinery/processing facility where they are refined into marketable products. The human use of petroleum has its drawbacks though, with e.g. micro-plastic contamination in the ocean [5], Nitrogen Oxide (NOx) air pollution [6-7] and global warming effects due to increasing concentrations of CO2 in the atmosphere [8-11]. In December 2015, on a climate conference in Paris, 195 countries signed an agreement to pursue to reduce the global CO2 emissions [12]. This agreement illustrates the international willingness to cooperate and solve the global climate change problem [13]. Carbon Capture Storage (CCS) is an important part of reducing the global CO2 emissions today and is expected to be so also in the future [14]. CCS involves the capture, transportation and storage of CO2. Current technologies to capture CO2 do exist. For example, Equinor (Statoil) runs a CCS program where they capture CO2 gas, then transport it before they inject it for storage in offshore petroleum reservoirs, e.g. Sleipner gas field, Snøhvit gas field and Utsira aquifer [15]. Equinor (Statoil) also capture CO2 as part of the liquefied natural gas (LNG) processing where there is a maximum content of CO2 that can be allowed in the produced natural gas before it is liquefied [16]. The captured CO2 can also be stored in gas hydrates to produce methane gas from hydrate fields [17]. Yet another mechanism associated with storage of the captured CO2 is storing the CO2 in coalbeds and simultaneously produce methane gas [18].

Most CO2 capture technologies that exist today are just in the research phase and have yet to be commercialized. The number of patents and publications on methods to capture CO2 are growing yearly, but most of them have never been scaled up on industrial level [20,21-23]. The technology used to capture the CO2 highly depends on the process plant and gas stream. For new technological methods to capture CO2, the possibility of implementing it on an already existing processing plant could save costs [24]. The most common industrial method to capture CO2 today is the conventional amine scrubber method [19-21]. The reactive monoethanolamines (MEA) are used as absorbing agents

that absorb the CO2 molecules in a scrubber tower where the flue gas is exposed to the liquid amine solution. The amine method to capture CO2 has its weakness with being costly and highly energy demanding in the regeneration process [25]. Also, the amines become corrosive at high pressures and in the presence of oxygen [26]. With the growing concern that the CO2 emissions contribute to global warming, more energy-efficient technologies to capture CO2 are necessary to reduce the global CO2 emissions.

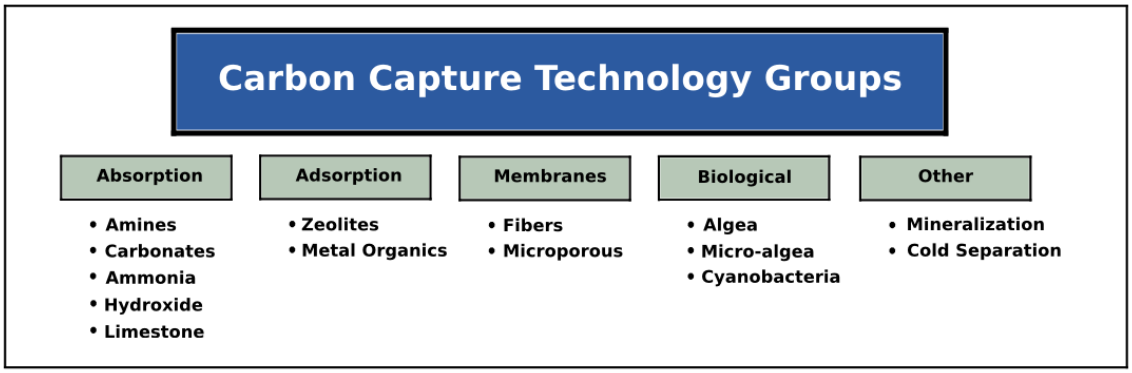

Figure 1.1: Categories the current post-combustion CO2 capture technologies can be divided into [26].

1.2 Current CO2 capture technology

Originally, the CO2 capture technologies were developed for other purposes in mind than the reduction of anthropogenic CO2 emissions [27]. For example, CO2 is captured so as to use it as part of Enhanced Oil Recovery (EOR), where CO2 is injected into depleted oil and gas reservoirs to improve the sweep efficiency. Yet another importance is to remove toxic gases such as CO2 and hydrogen sulfide (H2S) to prevent corrosion during transport of natural gas in pipelines. CO2 and H2S are both corrosive in contact with liquid water due to their dissociation reactions that releases H+. With the large Carbon Capture Storage (CCS) projects and the large-scale CO2 capture the governments talk about today, more energy-efficient technologies are needed to increase the CO2 capture capacity.

The technology used to capture CO2 in the industry today can be divided into three groups of technology. They are: post-combustion methods, oxy-fuel combustion methods and pre-combustion methods.

Post-combustion methods

The post-combustion CO2 capture technology is based on burning the fuel in a natural way before the CO2 is separated from the other flue gas mixture components. As figure 1.1 illustrates, the amine absorption solution method is a post-combustion method. Conventional amine scrubber technology is the most used technology to capture CO2 today. It is very efficient in terms of high purity in the separation process. Another advantage is the possibilities to retrofit this CO2 capture method to existing power plants. A challenge though with the amine method, is that it requires a lot of heat energy to regenerate the amines. In the regeneration process, the amine solution containing chemically absorbed CO2 is heated to a temperature where the CO2 molecules are released from the amines so that the amines can be reused. Generally, there are several drawbacks with the post-combustion methods. For example, the low concentration of CO2 in the flue gas (3-15 % CO2, 70% N2) makes it harder to separate [28]. Another example is the low-pressure conditions (ambient pressures) of the flue gas which is a disadvantage regarding compression costs for further transportation of the captured CO2 and the sequestration requirements.

Oxy-fuel combustion methods

With oxy-fuel combustion methods, the fuel is mixed with very oxygen-rich air (usually above 95% oxygen) and recycled flue gas before it is burned [28]. This kind of combustion process results in a decreased flue gas volume and a higher concentration of CO2, making it easier to separate the CO2. Much like the post-combustion method, the oxy-fuel method can be retrofitted to existing plants. However, there are some challenges with this method as well. The great amount of oxygen that is used in the combustion process results in high expenses due to the costs of oxygen production. In addition, the flue gas recycling can be expensive.

Pre-combustion methods

With the pre-combustion methods, the CO2 is captured prior to the combustion of fuel. The process is made by gasification of the fuel under high temperature and pressure (e.g. 473K,65bar) with the presence of oxygen [28]. The product is synthesis gas (syngas), a type of flue gas consisting of hydrogen gas (H2), carbon monoxide (CO) and CO2. The syngas production is followed by a reaction of the syngas with steam in a shift converted so as to convert CO and steam to CO2 and H2. By using e.g. conventional washing steps, the CO2 can be separated from H2 [28]. The main attraction with the pre-combustion CO2 capture is the high CO2 concentration of the CO2/H2 mixture. The high total pressure of that mixture facilitates the further transport and sequestration of the captured CO2. However, this advantage is balanced by the cost of oxygen separation from air and the expenses related to gasification. Originally, the pre-combustion method has been used in large-scale industrial processes to produce hydrogen and other chemical commodities, where CO2 is a by-product that is being removed [29].

1.3 The CO2 capture method evaluated in this project

The new method to capture CO2 presented in this master thesis can be placed in the post-combustion adsorption category, together with the zeolites, as illustrated in figure 1.1. The zeolite materials are typically combined with a binding material so as to produce pellets with embedded zeolite channels. Carbon nanotubes can be arranged in a similar fashion. The pore channels of zeolites are often 0.2-2 nano meters in diameter [30]. Today, zeolites are used to capture small volumes of CO2 from flue gas streams. They are also used to separate water from natural gas before e.g. transport and cryogenic processing. The research on zeolites often focuses on functionalized groups that can attract CO2 to enter the zeolite from a gas mixture with other components [31-32]. The CO2 separation with zeolites in the presence of water is not effective enough due to challenges with such as the high preference for water to adsorb to the net positively charged cations on the zeolites and hence blocking the access for CO2 molecules [33]. In this work, however, the focus will mainly be on how a non-polar carbon nano channel structure will discriminate the long-range nature of liquid water and adsorb the non-polar CO2.

This new approach to capture CO2 is based on the CO2 molecules in the flue gas distributed into the aqueous phase. At a saturation pressure of 100 bar and a 298K temperature, the equilibrium concentration of CO2 in water is 2.4 mole% [34]. Lee & Aluru published in 2013 a paper where they showed that CO2 is more soluble in water than other flue gas components, such as oxygen and nitrogen gas [35]. Another thing to mention about this new method to capture CO2 is that, next, after the CO2 is distributed into water from the flue gas, the CO2 will be separated from the water via the use of nano channels. Simulations conducted in this project investigated the efficiency of carbon nanotubes (CNTs) for the purpose of separation of CO2 from water. Furthermore, Lee & Aluru utilized molecular dynamics simulations to evaluate the separation process of CO2 from water with CNTs, with CO2 dissolved in water at equilibrium concentration [35]. The main difference between Lee & Aluru's research and studies conducted in this project is the concentration of CO2 in water. For this new method to capture CO2, the main idea is that an inhomogeneous, non-equilibrium water-CO2 mixture will be used. So, the idea is that if it is possible to have e.g. 5 or 10 times higher concentrations of CO2 in water compared to the equilibrium concentrations at that (T,P), then the hope is to achieve a very high flux of CO2 molecules into the nanotube in the separation process. Achieving 5 or 10 times higher concentration of CO2 in water is possible, with for example venture nozzles creating high hydrodynamic shear that will force the CO2 gas to distribute into water in the form of bubbles. For flue gas, most of the components, like nitrogen and oxygen, are highly supercritical components with low partial densities in the gas mixture. They likely be flushed off during a subsequent stage of rest before the water with distributed gas (mainly CO2) is exposed to a nanotube filter. The basic idea is to separate the CO2 from water with nanotubes by discrimination of the water molecules due to strong water-water hydrogen bonds.

2 Goals and motivation

The primary goal of this work was to investigate fundamental properties and thermodynamic driving forces involved in the selective separation of carbon dioxide from an aqueous system containing both dissolved CO2 as well as CO2 distributed as bubbles of various sizes, from nano scale and up. To achieve this goal, we have designed a non-equilibrium molecular dynamics simulation that makes it possible evaluate the fundamental aspects of the nanotube separation process of CO2 molecules from a non-equilibrium water-CO2 mixture.

Simulations conducted in this master thesis have been divided into two parts based on two fundamental characteristics of an adsorbent material: selectivity and capacity.

Part 1: Simulation study of nanotube selectivity and risk of water entrainment
The main goal of part 1 was to model a simulation system to evaluate the CO2 selectivity and water risk entrainment of the nanotube separation process as a function of nanotube size and initial pressure gradient across the nanotube.

Part 2: Simulation study focusing on nanotube capacity
The main goal of part 2 was to model a simulation system to evaluate the capacity of the nanotubes in terms of both CO2 flux and chemical potential as a function of nanotube size and driving forces in the water-CO2 mixture container.

3 Choice of scientific method

The nature of the phenomena addressed in this work is by definitions on a nano scale in dimension. The primary tool of investigation will therefore have to be on a nano scale to match. There are three primary simulation tools that naturally could have been chosen for a nano scale system. The first one was quantum mechanics (QM) ab-initio simulations. The quantum mechanics method was rejected because ab-initio calculations will be far too consuming in terms of Central Processing Unit (CPU) and time-expensive. Ab-initio calculations will as such only be used as a tool for assisting in calculating average atomistic interactions (force fields) for nano scale modeling tools. The second one was Monte Carlo (MC) simulations. MC methods will have the advantage of large systems and long-time scales since the steps can be substantially larger than typical motion scale in a Molecular Dynamics (MD) study. But, this fact was also one of the drawbacks of Monte Carlo – there is no time information. The third possible choice was Molecular Dynamics (MD) simulations. MD methods have the advantage of being able to follow the time evolvement of the system, which is an essential part of ensuring proper generation of entropy and ergodic distributions. Ergodicity means that the simulation sampling should reproduce the theoretical statistical distribution for the actual ensemble. For a molecular dynamics simulation at constant volume and constant number of particles, this would require that exchange of heat to keep the average temperature constant has to be done in a way to ensure that the sampled Boltzmann distributions reproduces that of the canonical ensemble. This will never be totally true, but at least it is possible to set thermostat parameters that bring the simulation system as close to ergodicity as possible.

The main scientific tool used to investigate the separation process has therefore been chosen to be Molecular Dynamics simulations combined with classical non-equilibrium thermodynamics for interpretation of the results. All the simulations in this research project were conducted with LAMMPS molecular dynamics simulator software [36]. LAMMPS is an efficient tool due to the abilities to separately control various sections of the non-equilibrium model system and general capabilities in terms of built-in thermostats and barostats needed for establishing realistic model systems.

4 Theory

4.1 Thermodynamics

Thermodynamics is a branch of physics that focuses on temperature and energy. Though thermodynamics is based on a set of four axiomatic laws, this discipline has been originally developed by engineers whose goal was to maximize efficiency of steam engines. Thermodynamics can successfully be applied to common everyday processes. For example, thermodynamics can be applied to the Carnot cycle that makes the refrigerator cool the beverages based on a refrigerant that follows a cycle where it at one point condenses into liquid and then evaporates. Thermodynamics can also be used to understand the meaning of an ice cube, where the phase transition of solid ice to liquid water occur at constant temperature and is due to energy absorbed by the ice cube. Another example of a thermodynamic system is the combustion engine where mechanical work is generated by compression and ignition of fuel.

4.1.1 First and second law of thermodynamics

The first and second laws of thermodynamic are two very useful statements. They will in this chapter be used to quickly derive an expression for both entropy and Gibbs free energy that can be used to evaluate the thermodynamic equilibrium conditions of a thermodynamic system. Consider a tank of a gas phase and a liquid phase, as shown in figure 4.1. There are N number of components in both phases. The tank (the system) is isolated from the rest of the universe (the surroundings), meaning that no heat or mass can be released/added to the tank. The gas phase and liquid phase are touching each other at the gas/liquid interface. Molecules can exchange between the two phases across the gas/liquid interface, as indicated by the two arrows.

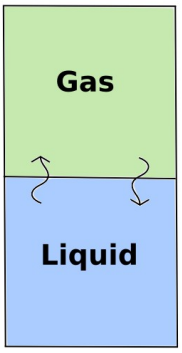

Figure 4.1: Gas/liquid tank

The first law of thermodynamics states that the internal energy of an isolated system is always conserved. Energy can transfer from one substance to another, but it will never disappear. The energy can be transferred from a substance to another as either work or heat. Applied to the tank in figure 4.1, the first law of thermodynamics for liquid phase can be stated as:

$$dU^{liquid} = dQ^{liquid} + dW^{liquid} + \Sigma \mu_i^{liquid} dN_i^{liquid} \tag{4.1}$$

And same for the gas phase:

$$dU^{gas} = dQ^{gas} + dW^{gas} + \Sigma\mu_i^{gas} dN_i^{gas} \tag{4.2}$$

dU^{liquid} is the change in internal energy for liquid phase, dQ^{liquid} is the change in heat for liquid phase, the term $dW^{liquid} = -P^{liquid} dV^{liquid}$ is the change in mechanical work for liquid phase and the term $\Sigma\mu_i^{liquid} dN_i^{liquid}$ is the change in chemical work for liquid phase for a multicomponent system where i is the component. Same notation for gas phase.

The change in heat dQ in equation (4.1) and (4.2) is related to the change in entropy dS and the absolute temperature T in the following way:

$$dS = \frac{dQ_{reversible}}{T} > \frac{dQ_{irreversible}}{T} \tag{4.3}$$

A reversible process is a change that always is in equilibrium with the surroundings and have no net entropy generation, meaning that equation (4.3) holds equality. Such process is possible to achieve if infinitesimal small changes are made as the system go from initial state to final state. Thus, for a reversible process, the system maintains equilibrium with the surroundings for each infinitesimal small change. An irreversible process on the other hand, is performed in a such a way that the change results in both energy leaving the system and an generation of entropy, meaning that equation (4.3) holds unequality. All processes in nature are irreversible. The reversible process is used just as an ideal case and a reference. For example, a combustion engine can be 100% efficient for a reversible process, but in real life, it is never 100% efficient due to e.g. frictions and heat losses.

The second law of thermodynamics states that for an irreversible process, the total entropy of the universe is always increasing. It also implies that heat cannot be transferred directly from low temperature to high temperature. Applied to the tank in figure 4.1, the second law of thermodynamics can be expressed as:

$$dS^{tot} \geq dS^{gas} + dS^{liquid} \geq 0 \tag{4.4}$$

The infinitesimal change in entropy for each phase can be defined as:

$$dS^{liquid} = \frac{dQ^{liquid}}{T^{liquid}} \qquad \text{and} \qquad dS^{gas} = \frac{dQ^{gas}}{T^{gas}} \tag{4.5}$$

For a thermal isolated system, $dQ^{liquid} = -dQ^{gas}$, meaning that no heat can be released or added to the tank system, equation (4.5) becomes:

$$dS^{liquid} = -\frac{dQ^{gas}}{T^{liquid}} \qquad \text{and} \qquad dS^{gas} = -\frac{dQ^{liquid}}{T^{gas}} \tag{4.6}$$

Combining equation (4.4) – (4.6) with equation (4.1) – (4.2), the internal energy for both phases can be expressed as:

$$d\,U^{liquid} \leq T^{gas}\,dS^{liquid} - P^{liquid}\,dV^{liquid} + \Sigma\mu_i^{liquid}\,dN_i^{liquid} \tag{4.7}$$

$$d\,U^{gas} \leq T^{liquid}\,dS^{gas} - P^{gas}\,dV^{gas} + \Sigma\mu_i^{gas}\,dN_i^{gas} \tag{4.8}$$

For an isolated system, the volume is conserved, meaning that $dV^{liquid} = -dV^{gas}$. The total internal energy is also conserved, meaning that $dU^{liquid} = -dU^{gas}$. And so is the number of molecules, which gives $dN^{liquid} = -dN^{gas}$. Those three conservation laws combined with the expressions for internal energy for each phase in equation (4.7) – (4.8) and with equation (4.4) gives an interesting expression for the change in total entropy:

$$dS^{tot} \geq \left[\frac{1}{T^{liquid}} - \frac{1}{T^{gas}}\right] dU^{gas} + \left[\frac{P^{gas}}{T^{liquid}} - \frac{P^{liquid}}{T^{gas}}\right] dV^{gas} - \Sigma\left[\frac{\mu_i^{gas}}{T^{liquid}} - \frac{\mu_i^{liquid}}{T^{gas}}\right] dN_i^{gas} \geq 0 \tag{4.9}$$

By combining equation (4.7) – (4.8) with the relation between Gibbs free energy *G,* enthalpy *H* and entropy *S* and *dG = dH – d(TS)* (the so called Legendre transformation), it is possible to obtain a very interesting term for the change in Gibbs free energy for the liquid phase:

$$dG^{liquid} \leq -S^{liquid}\,dT^{gas} + V^{liquid}\,dP^{liquid} + \Sigma\mu_i^{liquid}\,dN_i^{liquid} \leq 0 \tag{4.10}$$

And the same for the gas phase:

$$dG^{gas} \leq -S^{gas}\,dT^{liquid} + V^{gas}\,dP^{gas} + \Sigma\mu_i^{gas}\,dN_i^{gas} \leq 0 \tag{4.11}$$

Equation (4.10) and (4.11) are very useful. They relate the change in Gibbs free energy to easy accessible properties of the system, and they contain the three thermodynamic driving forces that drive a thermodynamic system towards equilibrium. $-SdT$ describes the thermal driving force, related to change in temperature. VdP describes the mechanical pressure driving force, related to change in pressure. $\Sigma\mu_i dN_i$ describes the chemical driving force, related to the exchange of particles.

4.1.2 Criteria for thermodynamic equilibrium

The change in total Gibbs free energy is the sum of the change in Gibbs free energy for each phase.

$$dG^{tot} = dG^{liquid} + dG^{gas} \tag{4.12}$$

A system is driven towards equilibrium by $dG^{tot} < 0$ and $dS^{tot} > 0$. When a system reaches equilibrium conditions due to mitigation of driving forces, then $dG^{tot} = 0$, which can be stated as:

$$dG^{tot} = dG^{liquid} + dG^{gas} = 0 \tag{4.13}$$

and

$$dG^{liquid} = -dG^{gas} \tag{4.14}$$

This implies that at thermodynamic equilibrium conditions, the total Gibbs free energy is minimized. At the same time, an infinitesimal small change in Gibbs free energy of the liquid phase is the same as the negative of the change in Gibbs free energy of the gas phase. At equilibrium conditions, there is no change in temperature or pressure, so $dT = 0$ and $dP = 0$. Therefore, by combination of equation (4.10)-(4.11) and (4.13), the total Gibbs free energy can written as:

$$dG^{tot} = \Sigma \mu_i^{liquid} dN_i^{liquid} + \Sigma \mu_i^{gas} dN_i^{gas} = 0 \tag{4.15}$$

The total change in quantity N_i (can be a change in e.g. number of molecules or number of moles) is:

$$dN_i^{tot} = dN_i^{liquid} + dN_i^{gas} \tag{4.16}$$

So, at equilibrium conditions, the transfer of molecules between the liquid phase and the gas phase, from one to the other, occur at the same rate. It is just the same as in reaction kinetics. When the reaction is at equilibrium, the forward and backward reactions occur at the same rate. Thus, at equilibrium:

$$dN_i^{tot} = 0 \quad \text{and} \quad dN_i^{liquid} = -dN_i^{gas} \tag{4.17}$$

Finally, the change in total Gibbs free energy can be written as:

$$dG^{tot} = \left(\Sigma \mu_i^{liquid} - \Sigma \mu_i^{gas} \right) dN_i^{liquid} = 0 \tag{4.18}$$

Equation (4.18) implies that $\mu_i^{liquid} = \mu_i^{gas}$ at equilibrium.

When a system reaches equilibrium conditions, also $dS^{tot}=0$:

$$dS^{tot}=[\frac{1}{T^{liquid}}-\frac{1}{T^{gas}}]dU^{gas}+[\frac{P^{gas}}{T^{liquid}}-\frac{P^{liquid}}{T^{gas}}]dV^{gas}-\Sigma[\frac{\mu_i^{gas}}{T^{liquid}}-\frac{\mu_i^{liquid}}{T^{gas}}]dN_i^{gas}=0 \qquad (4.19)$$

At equilibria the two phases in figure 4.1 can co-exist, which is a result from minimization of the total Gibbs free energy and maximization of the total entropy. Therefore, both $dG^{tot}=0$ and $dS^{tot}=0$, and the three thermodynamic equilibrium conditions between liquid and gas phase can be expressed as:

$$T^{liquid}=T^{gas} \qquad \textit{Thermal equilibrium} \qquad (4.20)$$

$$P^{liquid}=P^{gas} \qquad \textit{Mechanical equilibrium} \qquad (4.21)$$

$$\mu_i^{liquid}=\mu_i^{gas} \qquad \textit{Chemical equilibrium} \qquad (4.22)$$

No system can really reach thermodynamic equilibrium [37]. That is because there will always be some fluctuations in the temperature, pressure and number of molecules between the phases. Often, when applying thermodynamic equilibria in the description of a real process, the process is defined as a quasi-equilibrium process. For a quasi-equilibrium process, the changes as the system goes from state 1 to state 2 are so small that the system can be assumed to always be in equilibrium for each small change. Hence, the term “quasi-equilibrium” will be used when the simulations conducted in this project are assumed to have reached equilibrium.

4.1.3 Free energy calculation

Equation (4.10) and (4.11) include three thermodynamic driving forces: thermal, mechanical and chemical. Both temperature and pressure can easily be measured in many thermodynamic systems, including those vital for our daily lives. For instance, almost all homes have a thermostat that measures the outdoor temperature. Knowledge of the pressure and temperature of fluids in the operating units is essential for successful operation of oil and gas refineries, and therefore numerous pressure and temperature sensors are installed in the pipeline systems. On the other hand, chemical potential cannot be measured in a straightforward manner.

Still, methods to calculate the chemical potential have been developed. Two examples are Widom particle insertion method and the technique of thermodynamic integration method. They are both computational methods able to calculate chemical potential of a substance. In this research project, thermodynamic integration method was chosen because it can be relatively straightforward to implement within a purely molecular dynamics simulation of arbitrary density. The Widom particle insertion method will require additional sampling and is not guaranteed to work for simulations involving dense phases [38].

In brief, the Widom particle insertion technique is based on sampling the probability of inserting a test particle into the system. More comprehensively explained, the thermodynamic integration method is based on finding a reversible path that the system follows from its initial state to its final state. The system is a closed one-component system with a constant number of particles at constant temperature. Finding this path can be done by simulating the system for different constant temperatures and measure the potential energy per molecule for each simulation. Then, a plot can be made of potential energy per molecule vs 1/T. The potential energy per molecules in the simulation system is to be measured for temperatures ranging from normal conditions (e.g. 298 K) to infinity large temperature. Next, a polynomial function can be fitted to the data series in the potential energy per molecule vs. 1/T plot. The obtained polynomial fit function describes the path the system uses to go from its initial to final state. The initial state is the potential energy per molecule at normal system temperature, while its final state is the potential energy per molecule at theoretical infinity temperature. At the final state, the system will behave as an ideal gas. For an ideal gas, the free energy and the chemical potential is known. A basic integration technique can be used to solve the polynomial fit function. The integrated function can be expressed as [38, 39]:

$$\mu^{residual} = T_{initial} \int_{T_{final}}^{T_{initial}} U^{residual} \, d(1/T) \tag{4.23}$$

where $\mu^{residual}$ is the residual chemical potential and $U^{residual}$ is the residual potential energy per molecule [38].

The total chemical potential μ^{tot} can be expressed as:

$$\mu_i^{tot} = \mu_i^{residual} + \mu_i^{ideal\ gas} \tag{4.24}$$

The thermodynamic integration method, with equation (4.23), makes it possible to calculate the residual chemical potential of the substance of a real system. The ideal gas chemical potential can be calculated analytically. Usually, it is the total chemical potential that is used to compare the chemical potentials of different substances [40].

The chemical potential can also be defined in terms of thermodynamic state functions. Some examples are (at constant N_j where $j \neq i$):

$$\mu_i = \left(\frac{\partial G}{\partial dN_i}\right)_{T,P} \quad , \quad \mu_i = \left(\frac{\partial A}{\partial dN_i}\right)_{V,T} \quad , \quad \mu_i = \left(\frac{\partial H}{\partial dN_i}\right)_{S,P} \quad , \quad \mu_i = \left(\frac{\partial U}{\partial dN_i}\right)_{S,V} \tag{4.25}$$

They all tells us how the state variables Gibbs free energy G, internal energy U, enthalpy H and Helmholtz free energy A change when one more particle is added to the system by holding the respective state variables temperature T, pressure P, entropy S, volume V constant. Therefore, the chemical potential can be defined as the work required to add one more particle to the system. The chemical has an energy *SI* unit in *kJ/mole*.

Generally speaking, heat flows from a system with high temperature to a system with low temperature, a rock falls from high to lower height, and molecules diffuse from a region with high chemical potential to a region with lower chemical potential.

4.1.4 Gibbs phase rule

The Gibbs phase rule is a postulate for a multi-component heterogeneous (consisting of several phases) system that can be used to describe the number of independent thermodynamic variables F that needs to be specified to fully determine the system as a thermodynamic equilibrium system. The Gibbs phase rule can be stated as:

$$F = C - P + 2 \tag{4.26}$$

where F often is said to be the number of degrees of freedom, C is the number of components of the system and P is the number of phases in thermodynamic equilibrium with each other.

The best is to explain the Gibbs phase rule with some examples. A system of one component and one phase (pure liquid water for example) has two degrees of freedom: temperature and pressure, which can be varied independently. If the system has one component and two phases (liquid water and vapor for instance), then one degree of freedom is lost, and there is only one possible pressure for each temperature (described by the equilibrium curve in a pure water phase diagram). Add yet one more phase to the system (solid ice, liquid water and vapor), then the result is only one degree of freedom, described by a fixed temperature and pressure (the triple point) [41].

4.2 Statistical mechanics

The backbone of statistical mechanics is probability distributions. The statistical approach is used to describe physical phenomena because of the extremely large number of molecules. The large number of molecules is reflected by Avogadro's number, $N_A = 6.023 \cdot 10^{23}$ molecules/mole. An example on how probability theory is applied in statistical mechanics is the Maxwell-Boltzmann velocity distribution. Maxwell and Boltzmann explored that for each temperature, there is a probabilistic distribution of the velocity of the molecules. This means that the molecules don't move with the same velocity, but for each temperature, each velocity that the molecule can have has a certain probability. This principle is illustrated in figure 4.2, with the number of molecules (proportional to probability) on the y-axis and velocity on the x-axis. The distribution is for ideal gases, meaning that the molecules do not interact with each other except for collisions. As an example on molecular velocity, the most probable Maxwell-Boltzmann velocity of a nitrogen (N2) molecule in air is 422 m/s.

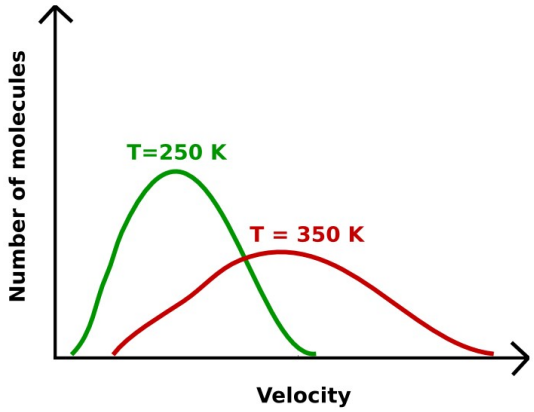

Figure 4.2: Illustration of Maxwell-Boltzmann velocity distribution.

4.2.1 Ensembles in statistical mechanics

The main goal with statistical mechanics is to find the macroscopic properties of a system by looking it from a molecular point of view. An ensemble consists of a set of microstates that all are constrained by some macroscopic properties. In the explanation of what a statistical ensemble is, let's begin by imagine a system of a large box with four walls that contains gas molecules. In figure 4.3, the gas molecules are illustrated as green dots. Figure 4.3 illustrates the idea behind statistical ensembles and microstates. The idea is that if we follow a system in time, with e.g. molecular dynamics simulations, the system will be in a new microstate for each time frame due to molecular interactions and motion. Each microstate in the ensemble are constrained by some fixed macroscopic properties of the system. The atomic and molecular properties can be different for each microstate, which is just natural because the molecules change their position and momentum each time frame. In a), the time is t_1. At this time frame, the system is in a certain microstate. In b), the time is t_2. From t_1 to t_2, the system changes its microstates because the xyz-position and the momentum of the molecules are updated. The microstate that the system is in at both time t_1 and t_2 are constrained by the governing statistical ensemble. In this case, each microstate have to correspond to the NVT ensemble. For the NVT ensemble, each microstate must have the same number of molecules N, the same volume V and give the ensemble temperature T.

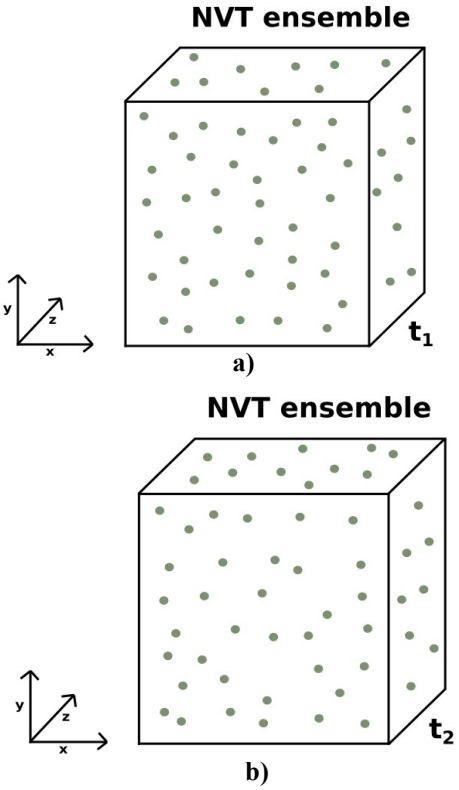

Figure 4.3: Illustration of NVT ensemble and microstates. a) time t_1. b) time t_2.

Many statistical ensembles exist. Some of them are listed in table 4.1 with the corresponding constant macroscopic properties that defines the ensemble. The macroscopic properties that are fixed for each system in an ensemble can be controlled by adjusting the boundaries the system has with its surroundings. For example, for a system in the canonical ensemble, the temperature can be kept constant on average by making the system a closed system surrounded by a heat bath so that heat energy can be applied to the system to adjust the temperature.

Table 4.1: Some examples on statistical ensembles and their fixed macrosopic properties.

Ensemble	Constant macroscopic variables
Canonical	*N, V, T*
Isothermal-Isobaric	*N, P, T*
Microcanonical	*N, V, E*
Grand canonical	*N, μ, T*

4.2.2 Phase space

Figure 4.3 illustrates just the position of the gas particles in the system. In both classical and statistical mechanics, each particle also has a momentum $p=mv$, where m is the mass of the particle and v is the velocity of the particle. The xyz-position and momentum for each particle are generally described by a phase space. The dimension of the phase space is $6N$, where N is the number of particles in the system. That is, 3 dimensions for the Cartesian xyz-coordinates and 3 dimensions for each component of the momentum of the particles.

The Hamiltonian is highly related to the phase space. The Hamiltonian is the total energy of the system. It is the sum of potential energy and kinetic energy and can be expressed as:

$$H(q,p,t)=U+KE=U(q_1,q_2,...,q_N)+\sum_{i=1}^{N}\frac{p_i^2}{2m_i} \tag{4.27}$$

where particle i with mass m_i will have the position q_i and momentum p_i in the phase space. The potential energy U is a function of only the position of the particles, while the kinetic energy KE is a function of only the momentum of the particles. A microstate can be thought of as a point in phases space, characterized by (q_i,p_i).

4.2.3 Coupling between microscopic and macroscopic properties

A partition function can be derived for each statistical ensemble. The partition function can give information about accessible microstates for the system in a given ensemble, and it is a function of thermodynamic state variables. It can also be expressed as the volume that the system occupies in the phase space. Thus, the partition functions are a link between microscopic and macroscopic properties. The microstate is a point in phase space while the macrostate is a probability distribution over the phase space. Related to the application use of the partition functions, a drawback is that they are highly advanced to solve. As an example, the partition function for the microcanonical ensemble can be written as:

$$\Omega(N,V,E)=M_N\int\delta(H(q,p,t)-E)\,d\Gamma \tag{4.28}$$

Q is the number of microstates belonging to the microcanonical ensemble, M_N is the microcanonical ensemble normalization factor, E is the microcanonical ensemble energy and Γ is the phase space volume [42].

Furthermore, the partition function for the canonical ensemble can be derived from the microcanonical ensemble by coupling the system to an infinite large external heat reservoir, and it can be expressed as:

$$Q(N,V,T)=C_N\int e^{-H(q,p,t)/k_BT}\,d\Gamma \tag{4.29}$$

where Ω is the number of microstates belonging to the canonical ensemble, C_N is the canonical normalization factor and k_B is the Boltzmann constant [42].

In the case of the microcanonical ensemble, each microstate with a total energy $H(q,p)$ within a certain range of the ensemble energy E can be assumed to have the same probability. All the microstates that do not satisfy this ensemble energy can be assumed to have 0 probability. Thus, for the microcanonical ensemble, at equilibrium conditions, the probability P_v for finding the system in a particular microstate v is:

$$P_v=\frac{1}{\Omega(N,V,E)} \tag{4.30}$$

And the entropy can be defined as:

$$S=k_B\log\Omega(N,V,E) \tag{4.31}$$

In molecular dynamics simulation studies, usually the Ergodicity theorem is used as a link between the microscopic and the macroscopic properties. In molecular dynamics simulation, we follow the time evolution of the system on a microscopic level. We know the initial start configuration of the molecules in the system and use classical mechanics Newtonian equations of motion to follow the trajectories and evolution of the system.

The Ergodicity theorem states that for both large enough time and large number of molecules, the ensemble average $\langle A \rangle$ is assumed to be the same as the time average $\overline{A(t)}$. The theorem can be expressed as:

$$\lim_{t \to \infty} \overline{A(t)} = \langle A \rangle \tag{4.32}$$

The ensemble average can be thought of as the average over all microstates in phase space. Preferably, the system throughout the simulation time will cover the whole phase space by visiting all the possible microstates for the given fixed thermodynamic properties of the ensemble, but in reality this is not possible due to e.g. information losses. The time average can be thought of as the average of all the microstates the system visits during the simulation run.

4.3 Molecular dynamics

A huge advantage inherent to molecular dynamics simulations is the possibility to have a molecular level of control, visualization and numerical analysis. In many applications of research and optimization, this is an absolute necessity, e.g. for adsorption processes where selectivity and diffusion only can be truly understood on a molecular level. The aim of molecular dynamics simulations is to obtain a deep understanding of molecular interactions and trajectories that could not be understood otherwise. Nevertheless, the simulations aim to be as realistic and physical as possible, and to imitate a real experiment. Molecular dynamics simulations can be seen as a bridge between the microscopic molecular level world of statistical mechanics and the macroscopic thermodynamic world [43].

4.3.1 Governing equations

The illustration of the system consisting of a box of gas molecules in figure 4.3 can be related to molecular dynamics simulation. In molecular dynamics simulation, by knowing the initial start configuration and with some governing equations of motion, the time evolution of the particles in the system can be approximated. Based on equation 4.33, the total force acting F on each atom in the system can be found by the negative gradient of the potential energy $U(r)$ between two atoms separated by a distance r:

$$F = -\nabla U(r) \tag{4.33}$$

The classical mechanics Newton's equations of motion are used to calculate numerically, step by step, the total force acting on each atom in the system. The initial start configuration of the components in the simulation system is known, and then equation (4.33) is used to calculate the total force acting on each atom in the system and their accelerations.

This gives a time evolution of the system, and the position and momentum of each atom is updated each time step. As mentioned previously, the position of an atom in phase space is a function of (q,p).

4.3.2 Integration of the equations of motion

Newton's second law can be stated as:

$$F_i = m_i a_i = \frac{d^2 q_i}{dt^2} \tag{4.34}$$

where F_i is the total force on particle i, m_i is the mass, a_i is the acceleration, q_i is the position vector and t is the time.

By combining equation (4.33) and (4.34), the acceleration of each particle can be calculated each time frame. In a molecular dynamics simulation, it is necessary to have an integration algorithm to advance the system in time. A variety of such algorithms exist. Two examples are the Verlét algorithm and the Leapfrog algorithm. The Verlét algorithm will be used to time integrate the simulations in this project and is derived shortly below.

Equation (4.34) is a second order differential equation. It would be more feasible to write it as two first order differential equations to more easily access the velocity vector v_i and the position vector q_i:

$$F_i = m_i \frac{d v_i}{dt} \tag{4.35}$$

$$v_i = \frac{d q_i}{dt} \tag{4.36}$$

The Verlét algorithm

One of the best developed time integration algorithms is the Verlét algorithm. The derivation of the Verlét algorithm starts by considering the Taylor expansion for the position q_i for particle i for time $(t +- \Delta t)$:

$$q_i(t+\Delta t) = q_i(t) + \left(\frac{dq_i}{dt}\right)_t \Delta t + \frac{1}{2}\left(\frac{d^2 q_i}{dt^2}\right)_t (\Delta t)^2 + \frac{1}{6}\left(\frac{d^3 q_i}{dt^3}\right)_t (\Delta t)^3 + O(\Delta t)^4 \tag{4.37}$$

$$q_i(t-\Delta t) = q_i(t) - \left(\frac{dq_i}{dt}\right)_t \Delta t + \frac{1}{2}\left(\frac{d^2 q_i}{dt^2}\right)_t (\Delta t)^2 - \frac{1}{6}\left(\frac{d^3 q_i}{dt^3}\right)_t (\Delta t)^3 + O(\Delta t)^4 \tag{4.38}$$

where Δt is the timestep [43,44]. By adding equation (4.37) and (4.38), the result is:

$$q_i(t+\Delta t) = 2 q_i(t) - q(t-\Delta t) + \left(\frac{d^2 q_i}{dt^2}\right)_t (\Delta t)^2 + O(\Delta t)^4 \tag{4.39}$$

Equation (4.39) is called the Verlét algorithm. $O(\Delta t)^4$ is the trunctation error of the algorithm and is the difference between the approximated Taylor expansion and the true smooth function. By choosing a large timestep Δt, the trunctation error will be greater than if a small timestep was chosen. Notice that in equation (4.39), the velocity term $v_i = (dq_i/dt)_t$ is cancelled out. By applying the numerical finite difference method, the velocity can be obtained:

$$v_i(t) = \left(\frac{q_i(\Delta t) - q_i(t - \Delta t)}{2\Delta t} \right) \tag{4.40}$$

The Verlét algorithm makes it possible to calculate the new position q_i at time $(t+\Delta t)$ for all the particles of the system, and to do this, both the position q_i and velocity v_i at current time t as well as the position at previous time $(t-\Delta t)$ are required. The timestep Δt is often chosen to be *1 femtoseconds (10^{-15} seconds)* in molecular dynamics simulations.

4.3.3 Force fields

Force fields are the backbone and the foundation of molecular dynamics simulations. They provide the input parameters used by the governing equations of motion to calculate the position of the atoms in phase space. Each atom in the system are described by a set of force field parameters. There exist many force fields and choosing the "correct" one for the simulation system and conditions can be critical for the results.

The total potential energy U_{tot} is often divided into two groups:

$$U_{tot} = U_{bonded} + U_{nonbonded} \tag{4.41}$$

4.3.4 Bonded interactions

The first constituents of the total potential energy in equation (4.41) is the bonded interactions U_{bonded}. It can be expressed as:

$$U_{bonded} = U_{bond} + U_{angle} + U_{dihedrals} + U_{impropers} \tag{4.42}$$

The bonded interactions are also called intramolecular interactions because they keep the atoms within a molecule together. The two molecules that will be used in this project (water and CO2), they both have bond stretching and angle bending potentials, but not dihedrals or improper potentials due to their simple triatomic molecular structure. Therefore, only bond stretching and angle bending will be explained in the following section.

Bond stretching

The length of the chemical bonds between two atoms in a molecule varies due to vibrations. The variations of the bond length are often described with a harmonic bond stretching potential. Hook's law is usually used to describe how the bond stretching potential energy $U_{bond}\ (r)$ changes as the bond length oscillates around its equilibrium length r_{eq}:

$$U_{bond}(r)=\frac{1}{2}k_{bond}(r-r_{eq})^2 \tag{4.43}$$

where r is the distance between the two atoms from atomic center to atomic center, k_{bond} is the bond stretching constant. A higher bond stretching constant would result in more rigid bonds.

Figure 4.4 illustrates this concept, showing two balls connected with a spring. Each ball is analogy to an atom, and the spring is analogy to the bond between them. Some force field models consider the chemical bonds as rigid, meaning that the bonds cannot stretch, and the bond lengths are constant with simulation time.

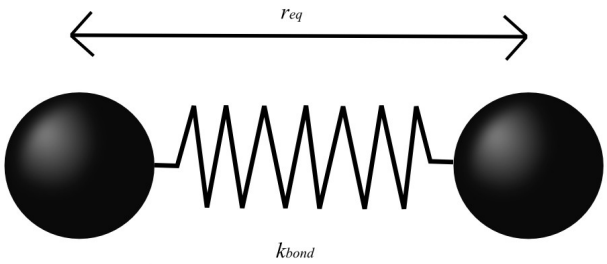

Figure 4.4: Illustration of intramolecular harmonic bond stretching between two atoms that makes up a molecule. Ball/spring model.

Angle bending

Similar to the bond length between two atoms, the angle between three atoms will often vary with time due to molecular vibrations, as illustrated in figure 4.4. The potential energy as a function of angle can be expressed with a harmonic potential by Hook's law:

$$U_{anglebending}(\theta)=\frac{1}{2}k_{angle}(\theta-\theta_{eq})^2 \tag{4.44}$$

where θ is the angle between three atoms in the same molecule, θ_{eq} is the equilibrium angle and k_a is the angle bending constant.

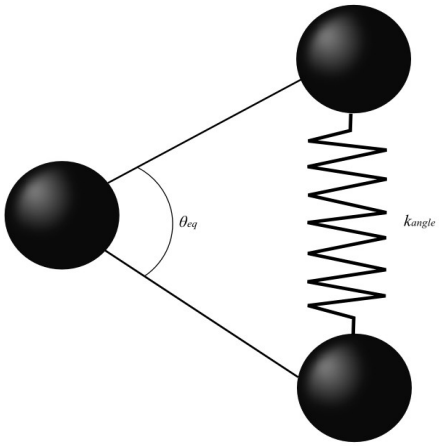

Figure 4.5: Illustration of intramolecular harmonic angle bending between three atoms that makes up a molecule. Ball/spring model.

4.3.5 Non-bonded interactions

The non-bonded interactions are both intra -and intermolecular, and they can include the interactions with all the other atoms in the system. They can be divided into two types: long-range and short-range. The long-range interactions are electrostatic forces, generally described in simulations by Coulombs law. The short-range interactions are vdw (van der Waal) interactions and are typically described by a Lennard-Jones model or a Buckingham model. The non-bonded interactions $U_{non\text{-}bonded}$ can be expressed as:

$$U_{non-bonded} = U_{electrostatic} + U_{vdw} \tag{4.45}$$

van der Waals interactions

The van der Waal interactions constitute of three forces, namely Keesom forces, Debye forces and London dispersion forces, as shown in equation (4.46).

$$U_{vdw} = U_{Keesom} + U_{Debye} + U_{London} \tag{4.46}$$

The three parts of the van der Waal forces are due to different electrostatic interactions:

Keesom forces: Permanent dipole – permanent dipole interactions
Debye forces: Permanent dipole – induced dipole interactions
Londons dispersion forces: Induced dipole – induced dipole

The Keesom forces are the interactions between two permanent polar molecules. The polarity of the molecules could be e.g. dipole-dipole interactions or quadrupole-quadrupole interactions. The polarity of a molecule comes from the difference in electronegativity between atoms in the molecule.

The Debye forces are the interactions between a molecule with a permanent dipole and a molecule with an induced dipole. The induced dipole moment of a molecule is due to temporary polarization of that molecule that happens in the presence of a polar molecule.

The London dispersion forces are interactions between two non-polar molecules. This interaction force is due to a temporary polarization of the non-polar molecules because of movement and different concentrations of the electrons in the electron cloud surrounding the atoms of the molecule.

The van der Waal interactions are short-range and considered as weak forces. They can be written as:

$$U_{vdw} = U_{repulsion} + U_{attraction} \tag{4.47}$$

The Keesom, Debye and London dispersion forces are the attractive contribution of the vdw forces and can be expressed as:

$$U_{attraction} = U_{Keesom} + U_{Debye} + U_{London} \tag{4.48}$$

The most common mathematical model that describes the short-range vdw forces is the Lennard-Jones 12-6 potential:

$$U_{LJ}(r) = 4\varepsilon\left[\left(\frac{\sigma}{r}\right)^{12} - \left(\frac{\sigma}{r}\right)^{6}\right] \tag{4.49}$$

where ε is the well depth of the potential and σ is the van der Waal radius. ε and σ are the parameters that makes the Lennard-Jones potential unique for each component of a simulation system. They can be fitted to experimental data or approximated with advanced quantum mechanics calculations.

There is a certain distance between atoms where the force between them is 0. For a greater distance than that point, an attractive Lennard-Jones force is yielding. For a less distance, a repulsive Lennard-Jones force is yielding. This is illustrated in figure 4.6. For the Lennard-Jones 12-6 potential, given by equation (4.49), the attractive forces decrease as a function of $1/r^6$ and the repulsion contribution of the vdw force fall off as $1/r^{12}$. The repulsion happens when two intermolecular atoms are too close and the electron clouds overlap. As the electron clouds overlap, the positively charged nuclei of the atoms results

in repulsion according to Paulie's exclusion principle.

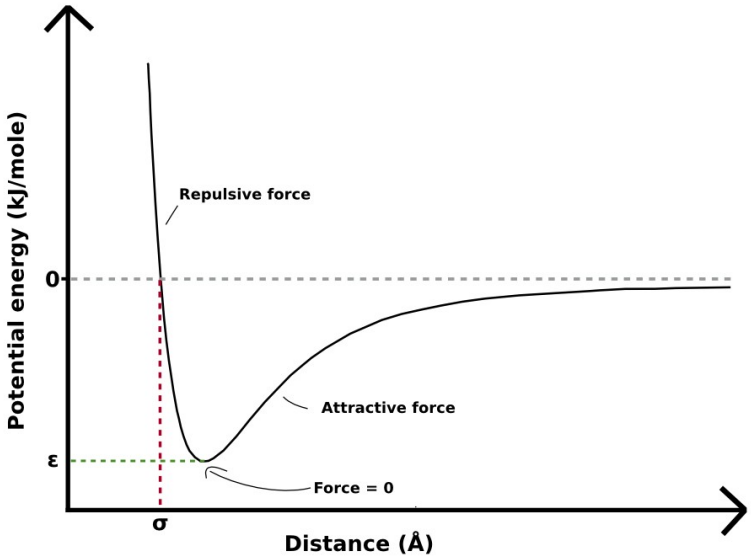

Figure 4.6: A general form of the Lennard-Jones 12-6 potential interactions between two similar atoms. Potential energy *U(r)* vs distance between the atoms *r*.

The Lennard-Jones 12-6 interaction potential is maybe the most popular, but also Buckingham potential is widely used [44]. The Buckingham potential has a softer repulsion [44], meaning that the repulsive curve will not be as steep as the Lennard-Jones repulsive interaction curve in figure 4.3. The Buckinghamp potential have three parameters, that is *A, B,* and *C,* compared to the two parameters ε, σ in the Lennard-Jones potential. The Buckingham potential can be written as [44]:

$$U_{Buckingham}(r) = A \times \exp(-B \times r) - \frac{C}{-r^6} \tag{4.50}$$

Note that the attractive part of the Buckingham potential also falls off as $1/r^6$. The Buckingham potential has the advantage that the repulsive part is expressed in an exponential form because it makes it more physical than the repulsive part for the Lennard-Jones 12-6 potential [44]. But, on the other hand, the three interaction parameters for the Buckingham potential makes it computational more expensive.

Eloctrostatic interactions

The electrostatic non-bonded interactions act on long-range and are considered as strong forces. For many force fields, the partial charges assigned to each atom are computed based on quantum mechanics and electronegativity differences. This makes it possible to replicate e.g. the dipole moment of water. The partial charge of each atoms are located at the center of each atoms, hence, electrostatic interactions can also be called simple point charge interactions. By reducing the electrostatic interactions to simple point charge interactions, Coulomb's law can be used to calculate the electrostatic forces between two atoms. The Coulomb's law can be expressed as:

$$U_{Coulomb} = \frac{1}{4\prod \varepsilon_0 \varepsilon_r} x \frac{Q_i Q_j}{|r_{ij}|} \tag{4.51}$$

where Q_i and Q_j are the partial simple point charges for atom of type i and j, $|r|$ is the absolute distance vector between the two atoms, ε_0 is the permittivity of vacuum and ε_r is the relative permittivity [44].

4.3.6 Periodic boundary conditions

Consider a system consisting of a box of atoms, as illustrated in figure 4.7. Imagine that the system is open, so the six surface walls of the box don't have mass or interactions. This means that as the simulations starts, and the atoms starts to interact and traject, some of them will most likely traject out of the box volume. When those atoms traject out the box, they cross the boundaries of the open system. Thus, the number of atoms in the system is not conserved and the density of the atoms in the box will decrease.

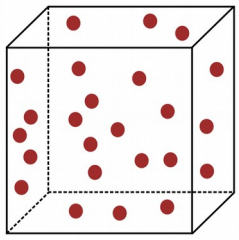

Figure 4.7: A box of atoms.

To account for this issue, periodic boundary conditions (PBC) are applied to the simulation system to make it a periodic system. Figure 4.8 illustrates the concept of periodic boundary conditions. In figure 4.8, the box in figure 4.7 is drawn in 2-dimensions for simplicity. The original box is the box in the middle with dark-red colored atoms. In a 2-dimensional space like this, when the periodic boundary conditions are applied correctly to the simulations system, there will be a copy of the original box on

each side of the original box. The atoms of the copied boxes are colored in light-red. So, the idea with periodic boundary conditions is that each of the boxes, the 9 boxes in this example, they will have the exact same movement as the neighbouring box when an atom trajects upwards and into the neighbouring box. When this happens, also a copy of that atom will traject into the box where it came from, from the neighbouring box below. This implies that the atom that trajects from the original box and into the box above, that atom will traject back into the original box from below. Thus, by applying periodic boundary conditions to the system, it is possible to maintain the density of the system constant with time. It also makes it possible to simulate an infinite large bulk system in the periodic directions, even with small amounts of atoms.

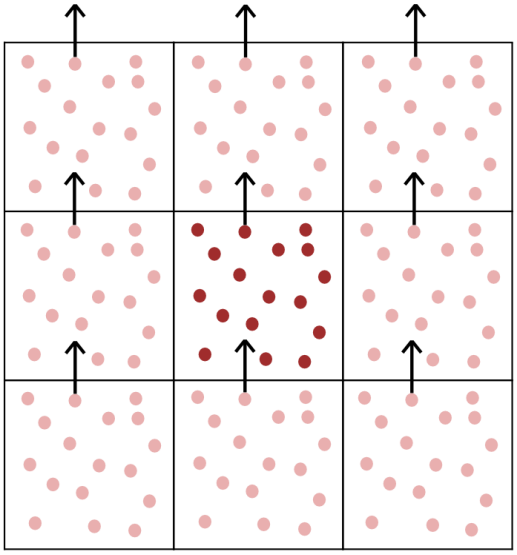

Figure 4.8: Illustration of a periodic system.

4.3.7 Cut-off radius and Ewald summation

The non-bonded interactions have two contributions: the short-range vdw forces and the long-range electrostatic forces. In molecular dynamics simulations, an usual approach is to use cut-off distance for the vdw forces. The attractive part of Lennard-Jones potential increases asymptotically (as seen in figure 4.6) and often the attractive part is cut off when the slope starts to flatten out. After the cut-off distance, the interaction force is sat to 0.0, and the attractive force is assumed to be very minor and to have a small effect on the total non-bonded interactions. The cut-off distance is made to save computational time because there will be much less interactions for the computer to calculate. A drawback with using cut-off radius is that it could result in discontinuity, but typically, if the cut-off is in the range (8-12 Å) it should not be any problem [38].

For the electrostatic forces on the other hand, it would be a very bad assumption to use cut off the forces. The reason is that the electrostatic forces do not fall off as quickly as the vdw forces. The vdw forces fall off as as $1/r^6$ (for the Lennard-Jones 12-6 potential), but the electrostatic fall off as only $1/r$. If a cut-off distance was to be used, then information would be lost and the computed interactions would be too inaccurate. The electrostatic forces are usually calculated with Coulombs law, and they give a significant large computational time compared to the vdw forces. A system can contain a numerous of particles that all have a potential that contribute to the total potential. Thus, something must be done with the electrostatic forces to save computational time.

Ewald summation is a numerical method that was developed to save computational time while still calculate the electrostatic potential accurate enough. The idea is to divide the calculation of electrostatic forces into two part: a short-range part and a long-range part. For a system with periodic boundary conditions, the total electrostatic interaction potential can be expressed as:

$$U_{electrostatic} = U_{short-range} + U_{Fourier} + U_{self} \tag{4.52}$$

Let's assume a simulation box containing N particles. Each particle is a point in space with charge q_i. We assume that the system as a whole is neutrally charged. Within the radial distance R, there exist a neighbour list for particle i where equation (4.53) is used to calculate the electrostatic pair interactions. Those interactions are considered as short-range and can be calculated using a modified version of Coulombs law:

$$U_{short-range} = \frac{1}{2}\sum_{i \neq j}^{N} \frac{q_i q_j erfc\left(\sqrt{\alpha r_{ij}}\right)}{r_{ij}} \tag{4.53}$$

where *erfc()* is a function that is introduced to make the interaction potential between the short-range part and long-range part of the electrostatic interaction smoother. α is related to the compensating Gaussian distribution screening cloud that is surrounding each point charge. For a greater radial distance than R, the electrostatic interactions $U_{Fourier}$ can be approximated by using Poissons law in combination with Fourier transformation. Those interactions are long-range, and they will act on an infinite distance. The system must be periodic. The term U_{self} in equation (4.52) is a correction for self-interaction [45].

In molecular dynamics simulations, an alternative to the traditional Ewald summation is often used to make it even more computational efficient. That is the Particle-Particle Particle-Mesh (PPPM) method by Hockney & Eastwood [38, 46-47]. Briefly explained, the PPPM algorithm handles the Fourier part more efficiently by distributing the particle charges into mesh grids so as to solve the Poisson equation much more efficiently [38]. The size of the mesh grids has a huge impact on the computational efficiency. Large mesh grids will give fast computation, but the approximated electrostatic forces in Fourier

space (k-space) will then be less accurate.

4.3.8 Temperature control

From the illustration of the Maxwell-Boltzmann velocity distribution of ideal gases in figure 4.1, it can be seen that a higher temperature gives a higher probability of having molecules with higher speed. This is gives rise to a relation between temperature and average kinetic energy $\langle KE \rangle$:

$$\langle KE \rangle = \frac{1}{2} \sum_i m_i \langle v_i^2 \rangle = \frac{3}{2} k_b T \tag{4.54}$$

where m_i is the mass of particle i, v_i is the velocity of particle i, k_b is the Boltzmann constant and T is the temperature.

The most natural ensemble in molecular dynamics simulations would be to use the microcanonical (NVE) ensemble due to energy conservation and the Newton's equations of motion. But, in real life, most experiments are carried out under the conditions of constant temperature, not constant energy. When the canonical ensemble (NVT) is used in molecular dynamics simulations, it is necessary to use a thermostat to keep the temperature constant. There exist many computational algorithms for that purpose. Three examples are: the Nosé-Hover thermostat, the Berendsen thermostat and the Anderson thermostat.

The goal with a thermostat is to keep the average temperature of the system constant. For each timestep, the system will be in a new microstate with a new instantaneous kinetic energy. If the kinetic energy each time step had been kept constant, then it would have affected the system too much. Thus, in molecular dynamics simulations, when a thermostat is applied, the temperature will fluctuate around the average thermostat temperature. An important thing to be aware of though, is that the fluctuations usually is smaller for a system with a larger number of particles.

The Berendsen thermostat

The Berendsen thermostat uses velocity scaling to control the temperature [48]. The velocities are scaled each time step, and the temperature of the system is controlled by the equation:

$$\frac{dT(t)}{dt} = \frac{1}{\tau}(T_0 - T(t)) \tag{4.55}$$

where $T(t)$ is the temperature of the system at time t [48, 49]. T_0 is the temperature of an

external hypothetical heat bath that the Berendsen thermostat uses to maintain the temperature of the system by coupling the two thermostats with the coupling parameter τ. Both T_0 and τ are often used as input parameters in a run script for a molecular dynamics simulation. The magnitude of the coupling parameter determents how active the thermostat is and how much the thermostat affects the system. On average, the goal is that the temperature of the system is the same as the desired temperature T_0. The Berendsen thermostat has shown good tendencies to drive a non-equilibrated system towards equilibrium [50]. Another advantage with the Berendsen thermostat is the simplicity in the code, hence, easy to implement. But, it does have some drawbacks: it is often said to not be able to generate canonical partition function (cannot produce correct statistical ensemble) [50], it can generate discontinuity in the phase space trajectories, it is non-ergotic and it is not time-reversible [50]. However, in practice, the amount of deviation from the canonical distribution is usually quite small [50].

The Nosé-Hoover thermostat

Nosé came up with a set with equations in 1984 [51] before Hoover in 1985 improved and simplified those equations to make the the Nosé-Hoover thermostat [52].

The equations used in the Nosé-Hoover algorithm contain some modifications on the Newton's equations of motion. An external heat bath is added to the system, which gives the atoms one extra degree of freedom. Due to this heat bath, the total energy of the simulation system is changed. Thus, an extra kinetic energy and potential energy are added to the total energy [44,50]. Heat energy can transfer between the system and the heat bath. Briefly explained, an equation of motion for the extra degree of freedom is solved. This equation can be expressed as an expansion of the Hamiltonian, with an extra degree of freedom [44,50]:

$$H_{Nosé-Hoover} = \sum_i^N \frac{p_i^2}{2m_i} + U(q_i, \ldots, q_N) + \frac{\zeta^2 Q}{2} + (3N)\frac{\ln(s)}{\beta} \qquad (4.56)$$

In equation (3.51), the two first terms are the kinetic energy and potential energy previously defined for the classical Hamiltonian. The two next terms are added by Nosé and Hoover, and all together, they make up the Hamiltonian used in the Nosé-Hoover thermostat. ζ is the thermodynamic friction coefficient and s is a time scale variable and is associated with the external heat bath reservoir.

The Nosé-Hover has the advantage of producing the canonical distribution as well as being deterministic and time-reversible for equilibrium systems [50]. But, as a drawback, it can result in a non-ergodic system if becoming trapped in a subspace [50].

4.3.9 Pressure control

For an isothermal – isobaric (NPT) ensemble, it is necessary to use a barostat to control the pressure. Two examples of such barostats are: the Nosé-Hoover barostat and the Berendsen barostat.

Briefly explained, both the Berendsen and the Nosé-Hoover barostat control the pressure of the system by adjusting the volume of the box. The Virial pressure is calculated and then the volume of the simulation box is allowed to fluctuate (hopefully to give the statistical ensemble pressure) so that the desired pressure is reached.

5 Set-up of the simulation systems

The simulation studies conducted in this work were aiming at imitating the selective nanotube separation of water and CO2. The overall goal was to evaluate the potential for nanotube separation in terms of CO2 selectivity and nanotube capacity (flux and chemical potential). Unlike many other separation methods, this method focuses on the fact that these nano-tubes gives very limited space for water molecules to establish long-range water hydrogen bonded structures.

Section 5.1 presents the simulation systems investigated in part 1 of this work, where the selectivity and water risk for the separation process with nanotubes from a non-equilibrium water-CO2 mixture (with super-high concentrations of CO2 initially distributed in water) have been evaluated. For this purpose, a non-equilibrium system was set up and analyzed. The left chamber (water-CO2 mixture container) of the set-up was aimed to reproduce a system of hydrodynamically stirred liquid water with CO2 in form of both nano bubbles and dissolved CO2. The right side chamber (the receiving tank), connected to the left side chamber via the nanotube, was initially filled with CO2 gas. In part 1, water and CO2 molecules in the water-CO2 mixture container were initially randomly distributed to reduce the bias effect for favourising initial positions in the separation process. The system was initially out of equilibrium, with two graphene walls used to separate the two containers.

In chapter 5.2, the simulation system employed in part 2 will be presented. The simulation performed in part 2 focused on evaluating the nanotube capacity. The system set-up in part 2 was very similar to that of part 1. However, two changes related to initial conditions have been made. The first one concerned the initial configuration of water/CO2 molecules in the water-CO2 mixture. In the system set-up for part 2, the water and CO2 molecules were separated into two layers for better control of the driving forces and mitigation of the water flux through the nanotube. The second change involved the movement of the left hand side graphene wall in the water-CO2 mixture container to enable control over the driving forces (by keeping the density of CO2 in the water-CO2 mixture container constant). Systems modelled for part 2 were designed on the assumption that the filling of the right side chamber will stop by itself when the chemical potential for CO2 in the connecting end of the nanotube will be equalized with chemical potential of CO2 in the right tank. At this point, the mechanical work exchange between tube and the right chamber should vanish as well. This assumption will be used to estimate the chemical potential of CO2 inside the nanotube.

5.1 Initial conditions used in the study of nanotube selectivity

This section presents the simulation systems used in part 1. A major part of work done in this project has been focusing on designing a simulation set-up enabling to evaluate the separation process in a realistic way. The goal of part 1 of this project was to investigate the separation process in terms of selectivity and risk of water entrainment as a function of nanotube size and initial pressure gradient across the nanotube.

As mentioned in chapter 1, this new technique to capture CO2 proposed in this master thesis is a post-combustion adsorption method. The combustion of fossil fuel (coal, oil and gas) give rise to flue gases. This new method to capture CO2 is based on the fact that it is possible to dissolve substantial amounts of CO2 in water from flue gas with, for example, venture nozzles. CO2 dissolves much more easily in water than the other flue gas components, and hence, impurities of other flue gas components are neglected in this work. This work focuses on the nanotube separation of CO2 from the water-CO2 mixture obtained from the venture nozzles. The venture nozzles work by making a massive hydrodynamic effect that can give both a massive mass flow of CO2 molecules into the water and an increase in the water/CO2 surface contact area, making it possible to distribute a substantial amount of CO2 in water. The water-CO2 mixture evaluated in this work constituted a non-equilibrium system, with the CO2 aqueous concentrations substantially exceeding the solubility limit at the relevant pressure and temperature. A hypothesis investigated in this work stated that this non-equilibrium water-CO2 mixture can be used to achieve high effective selectivity and flux of CO2 through the nanotubes.

5.1.1 Description of the system set-up used to study selectivity and water risk

Figure 5.1 shows the simulation system set-up modelled in part 1 of this project. There are four graphene walls in the systems. The only reason for including the graphene walls was to separate the water-CO2 mixture container (waterCO2box) and the receiving tank (CO2box) so as establish pressure and chemical gradients across the nanotube. The nanotube extended 60 Å in z-direction. Two regions are defined to make it easier to discuss the system. The water-CO2 mixture container (waterCO2box) is the region between the two graphene walls to the left of the nanotube. The waterCO2box initially contained 10 mole% of CO2 distributed in water, which is 5-10 times higher than its solubility limit. The receiving tank (CO2box) is a 52 Å region between the two graphene walls to the right of the nanotube. The CO2box was, initially, exactly the same in all simulations performed in both parts 1 and 2. The receiving tank initially contained 146 CO2 molecules, corresponding to density of 84.0 kg/m3, which makes the CO2 a gas phase at 298K. The only differences between the system in figure 5.1 a) and b) is the nanotube size (diameter) and the initial number of CO2 molecules in the nanotube. The system in a) consisted of a (10,10) nanotube while system b) contained a (20,20) nanotube.

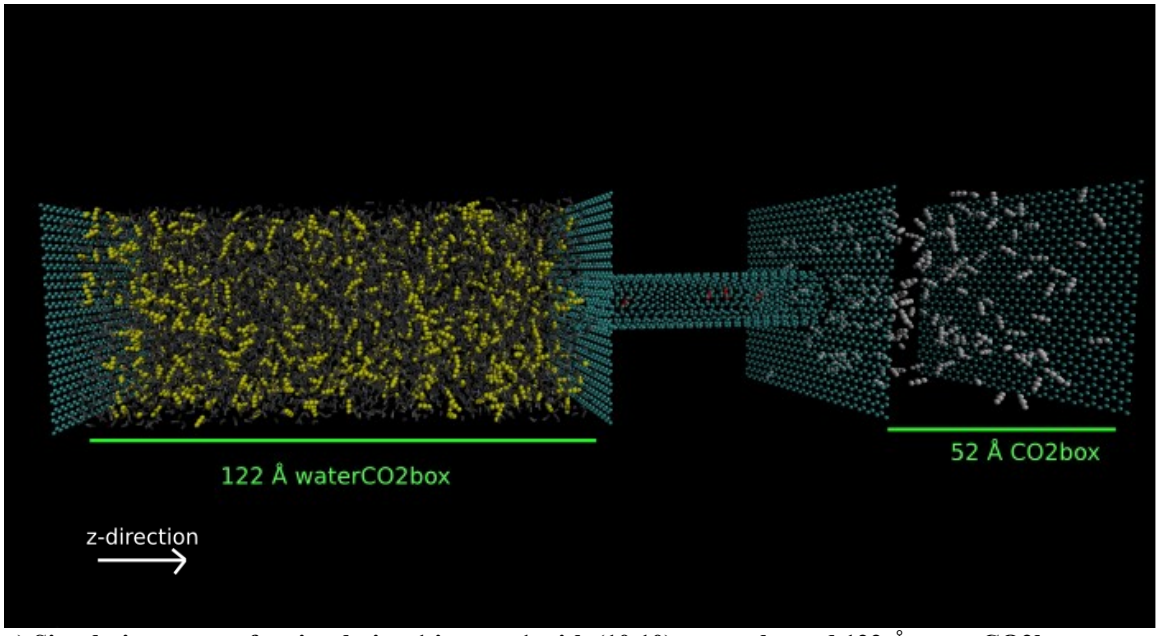

a) Simulation system for simulation 1 in part 1 with (10,10) nanotube and 122 Å waterCO2box.

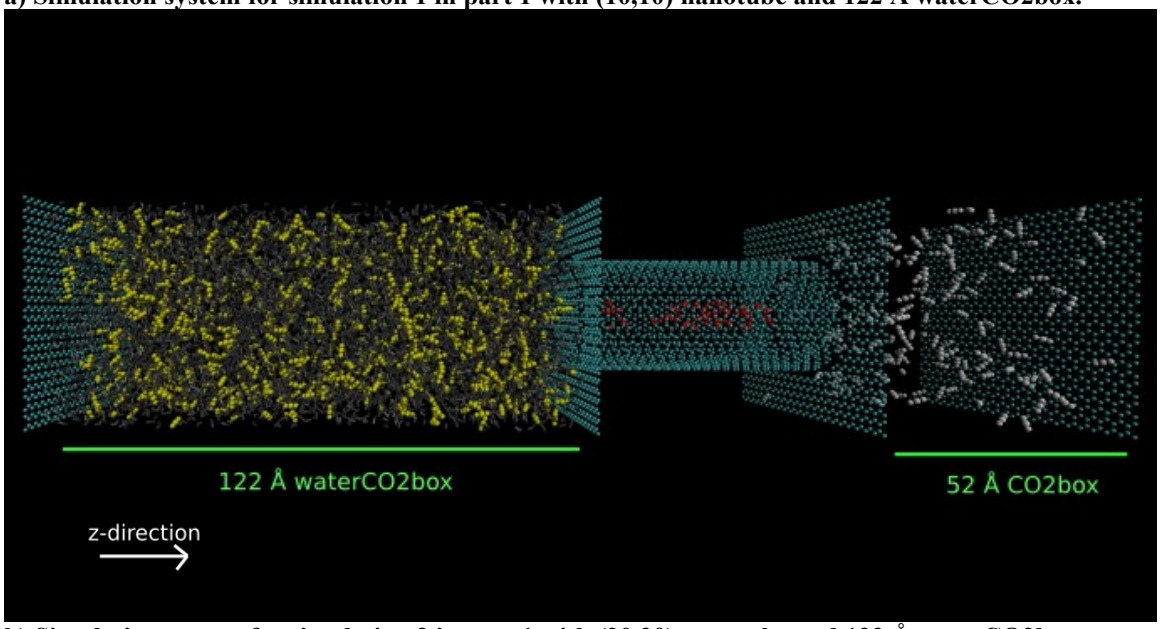

b) Simulation system for simulation 2 in part 1 with (20,20) nanotube and 122 Å waterCO2box.

Figure 5.1: Initial system set-up in part 1 at simulation time 0. Gray colored molecules are water. Yellow, red and white colored molecules are all CO2 molecules, but in different region of the system. The blue atoms are carbon in the nanotube and the graphene walls.

Figure 5.2 illustrates the xyz-directions for all the main simulations in both part 1 and 2. The z-direction will always be normal to the radial cross-sectional area of the nanotube and normal to the graphene walls. The z-direction is also illustrated in figure 5.1 a) and b). The xy-axes will be centered in the origin of the graphene walls.

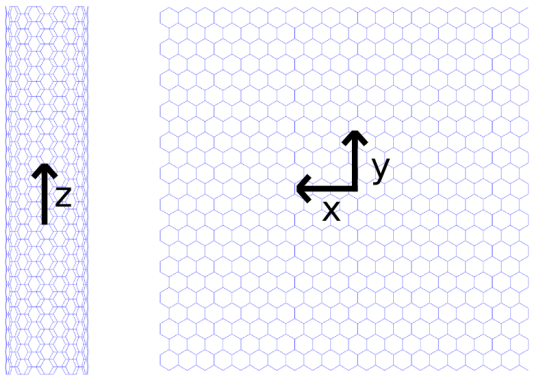

Figure 5.2: Illustration of the xyz-direction relative to the nanotube and the graphene walls used in all the main simulations in both part 1 and 2.

5.1.2 The four simulations in part 1

Four main simulations were performed as part 1 of this research project, with two variables independently varied across the four simulations. The first parameter was the nanotube size. Two nanotube sizes were used: a (10,10) nanotube and a (20,20) nanotube. The second independent variable was the length of the water/CO2 mixture container (waterCO2box) in z-direction. The z-size of the waterCO2box is used as an independent variable because changing it will also change the initial pressure gradient across the nanotube (the initial pressure in the water/CO2 mixture is increased if the z-size of the waterCO2box is reduced). The four simulations with the corresponding nanotube size and z-size of the waterCO2box are listed in table 5.1. In simulation 1 and 2, the z-size of the waterCO2box is 122 Å, and they are shown in figure 5.1 for illustration of the set-up in part 1. This z-size was chosen based on the results from a numerous of NPT simulations, discussed in section 5.1.4. The 122 Å z-size of the water-CO2 mixture is more like the natural with minor compression of the water and minor CO2 gas expansion. In the next simulations, simulation 3 and 4, the z-size of the waterCO2box is 112 Å. The choice of the z-size of the waterCO2box in simulations 3 and 4 were based on the results obtained in simulations 1-2 which produced very good selectivity and a small risk of water entrainment. We have chosen to simulate a smaller initial volume of the water-CO2 mixture in simulations 3-4 to have a higher initial pressure gradient and have a wider evaluation of the selectivity and water risk.

Table 5.1: The four simulations conducted in part 1 with the corresponding two independent variables - nanotube size and z-size of the waterCO2box.

Simulation nr.	Nanotube size	z-size of waterCO2box
Simulation 1	(10,10)	122 Å
Simulation 2	(20,20)	122 Å
Simulation 3	(10,10)	112 Å
Simulation 4	(20,20)	112 A

The number of water and CO2 molecules initially in the different regions of the system in all the four simulations conducted in part 1 is shown in table 5.2.

Table 5.2: The number of water and CO2 molecules initially in the different regions of the system in all the four simulations conducted in part 1.

Simulation nr.	N_{water} in waterCO2box	N_{CO2} in waterCO2box	N_{CO2} in nanotube	N_{CO2} in CO2box
Simulation 1	7932	882	4	146
Simulation 2	7932	882	35	146
Simulation 3	7932	882	4	146
Simulation 4	7932	882	35	146

5.1.3 Challenges in controlling pressure in water/CO2 mixtures

All the four simulations conducted in part 1 used 10 mole% of CO2 initially distributed in water. This CO2 concentration is way above the equilibrium concentration of CO2 in water at 298 K and pressure ranging from 1 to 600 bar [53]. As two extreme points, at 298 K and 1 bar, the saturation concentration of CO2 in water will be roughly equal to 1 mole%, and ~3 mole% at 600 bar. In the design and optimization of e.g. an amine scrubber process unit or a zeolite separation process unit, the operational pressure and temperature are critical properties to know. The same would hold true when designing a process unit where nanotubes are used to separate CO2 from the non-equilibrium water-CO2 mixture. But, at this early stage of researching on this new method to capture CO2, the lack of this knowledge is not all that critical. Ideally, the opportunity to measure a realistic pressure in molecular dynamics simulation would have been the best, but given the overall complexity of the non-equilibrium water-CO2 mixture, any pressure during

the simulation would be difficult to relate to industrial operating conditions. Based on operational amine scrubber data, the pressure and temperature of the inlet flue gas that enters the amine absorption tower is 1 atm and 313K [54-55]. The zeolite CO2 adsorption process unit also usually operate with an inlet flue gas at 1 atm [54-55]. In this case, for the new method to capture CO2 that is investigated in this project, it is very difficult to predict and measure what the operating pressure will be because the water will be super-saturated with CO2 way above equilibrium concentrations. As we will see later from the simulations, the non-equilibrium water-CO2 mixture is very complex. It can consist of different local concentrations, such as nanobubbles that break and forms. As a consequence, in part 1 of this research project, the values of the pressure of the water-CO2 mixture were disregarded (but they were of course interpreted during the simulation runs to ensure that the pressure is neither too high or low). Furthermore, in part 1, the volume of the water-CO2 mixture was used as a variable to simulate for two different pressures of the non-equilibrium water-CO2 mixture, as illustrated in table 5.1.

10 mole% CO2 initially in water was chosen due to two reasons. Firstly, the 10 mole% is a high enough concentration to evaluate the primary goals with this research project. Secondly, it was found from numerous pre-study simulations that exceeding this concentration (i.e. using 15 mole%) will result in a phase separation of CO2 and water into two different layers, which is unfortunate since water should be the continuous phase in part 1. The vigorous phase separation that happened at very high concentrations of CO2 in water illustrated that it is not possible to include the venture nozzle effect in LAMMPS molecular dynamics simulations. But still, this is a pioneer project and a lot of information can be obtained from the LAMMPS simulations conducted in this project, even without this effect.

Related to an industrial process unit, the water-CO2 mixture in the water-CO2 mixture container can be thought of as a water-CO2 mixture that just have reached the nanotube entrance. The ideal scenario can be defined as a separation process with a 100% efficiency regarding the selectivity and water risk, meaning that only CO2 molecules and no water molecules are transported from the water-CO2 mixture, through the nanotube and into the receiving tank. In a real, industrial separation process, the receiving tank may not be present, but just a very long nanochannel. In this work, the receiving tank (CO2box) was just used as a reservoir to evaluate the water and CO2 flux through the nanotubes. It is difficult to predict exactly in details how the nanotube system will look like in an experiment or in industrial use. This is just a pioneer research project, with the results aimed to be used in further studies. The nanochannels can perhaps be thought to have a similar structure as the pores in zeolites, and perhaps they could be used in relation to a fluidized beds. Most likely, the graphene walls will not be present in a real-life experiment or an industrial process since their only purpose was to separate the two containers.

5.1.4 NPT simulations to find volume of water-CO2 mixture

As mentioned previously, the 10 mole% CO2 distributed in water-CO2 mixture is very complex, and there have been some challenges in controlling the pressure. The pressure was found to be very difficult to control because there are too much going on in the water-CO2 mixture with e.g. phase separation and a non-uniform mixture. Nevertheless, it was found necessary to find a volume of the water-CO2 mixture that is as realistic as possible with neither too high or too low pressures. With this purpose in mind, 5 NPT simulations were ran with different barostat pressures to see at what volume the mixture stabilizes. The NPT simulations were ran with an anisotropic barostat in z-direction. The system was simulated for five different barostat pressures, shown in table 5.3 with the resulting z-size of the water-CO2 mixture. The xy-size of the box was kept constant because the graphene wall is rigid and had to be connected perfectly with "itself" over periodic boundary conditions in xy-direction.

The procedure for those 5 NPT simulations was as following. First, for a box with volume *(51.577x51.048x100.0) Å³*, the number of water molecules with a density of 1000.3 kg/m3 was calculated. The density was taken from NIST at 298K and 100bar [56-57]. Then, one water molecule was removed for each CO2 molecule added until 10 mole % CO2 was reached. This resulted in 7932 water and 882 CO2 molecules. The resulting box of water and CO2 molecules from the calculations is not physical at all due to the larger size of the CO2 molecules compared to the water molecules. The calculations were done with full awareness. For a real mixture, the partial volume of each component is not the same as for the mixture. Thus, 5 NPT simulations were run with different barostat pressures to see at what volume the mixture stabilizes. All the simulations were run for 10ns. A snapshot of the NPT simulation of the water-CO2 mixture with a 300 bar anisotropic barostat is shown in figure 5.3. The figure shows the 10 mole% CO2 water-CO2 mixture and a 1/10 scale down graphene wall in the middle. In the figure, there is just one graphene wall. But, the water/CO2 molecules actually feel two graphene walls due to the periodic boundary conditions in the z-direction, making the system in figure 5.3 the same as the water-CO2 container (waterCO2box) in figure 5.1.

In figure 5.3, it can be seen how the system have evolved after 10 ns simulation. At this point in time, the liquid water is the continuous phase. Phase separation has occurred. A few CO2 molecules seem to be dissolved in the water, while the majority of the CO2 molecules either enrich near the graphene wall or is part of the CO2 nano bubble. The formation of the CO2 nano bubble and the CO2 enrichment near the graphene wall happens due to the high concentration of CO2 in water. With 10 mole% CO2 in water, there is a lot of excess CO2 molecules above the equilibrium concentration of CO2 dissolved water. It is favorable for both water and CO2 to minimize the surface area between water/CO2, which is exactly what happens when a nano bubble is formed and when CO2 enrich near the graphene wall.

Conducting the 5 NPT simulations with different pressures were necessary to have an understanding on how the model volume of the water-CO2 mixture is for different pressures. The z-size of the 300 bar NPT simulations was 122 Å, and this is the z-size of the water-CO2 mixture (waterCO2box) that will be used in simulation 1 and 2 in part 1, as shown in table 5.1. The 122 Å z-size box of the water-CO2 mixture is more like its natural model volume, with a pressure that is not too high because the density of the CO2 enrichment layer was not too compressed, thus the water is not too compressed. Also, as seen from the density profile in figure 5.4, the peak of the CO2 density near the graphene wall is about 730 kg/m3. This above the 712 kg/m3 dew-point density of CO2, meaning that the CO2 have a liquid density, but the graphene surface might affect the phase transition. The 200 bar simulation was very similar to the 300 bar simulation, but the 100 bar gave a density peak of about 320 kg/m3, meaning that the CO2 is close to the bubble point density of 240 kg/m3. It is vital that CO2 is in liquid phase (or aqueous phase) to be able to imitate a real water-CO2 mixture. It is also critical to avoid CO2 gas expansion during the separation process that may happen as a result of the CO2 enrichment. Another interesting observation from the 5 NPT simulations is that the volume of the water-CO2 mixture does not change much. It is the density of the CO2 enrichment layer near the graphene wall that changes as the pressure is adjusted. This could be because water is more incompressible than CO2. Water is highly incompressible due to hydrogen bonds, meaning that a small change in volume would result in a large change in pressure.

The pressures in table 5.3 will not be used in this thesis anymore. They were used just as barostat-pressures to find the proper model volume of the non-equilibrium water-CO2 mixture (to be used in the waterCO2box).

Table 5.3: NPT simulations for different anisotropic barostat pressures in z-direction of a water/CO2 mixture containing 10 mole% CO2, and the resulting z-size of the water/CO2 mixture.

Barostat pressure	z-size
100 bar	(160.4 +- 0.9) Å
200 bar	(131.2 +- 0.8) Å
300 bar	(122.3 +- 0.6) Å
500 bar	(117.5 +- 0.5) A
1000 bar	(112.9 +- 0.3) Å

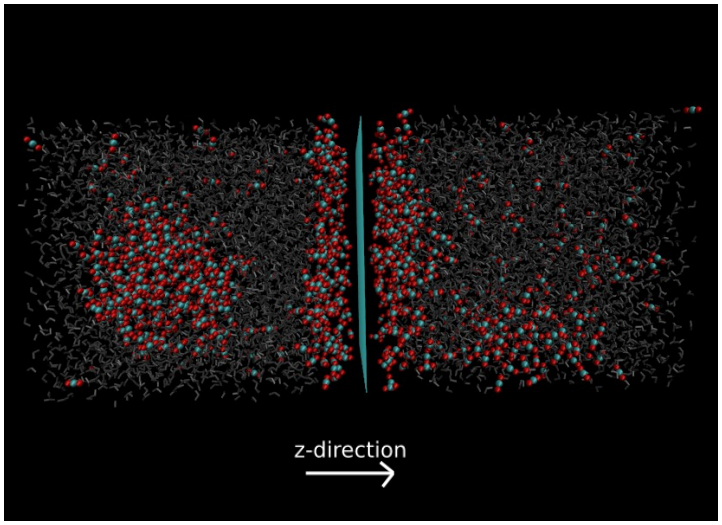

Figure 5.3: NPT simulation of the 10 mole% CO2 in water-CO2 mixture with a 300 bar anisotropic barostat in z-direction. Gray coloring are water molecules and the red/blue are CO2 molecules. The blue wall in the middle is a graphene sheet.

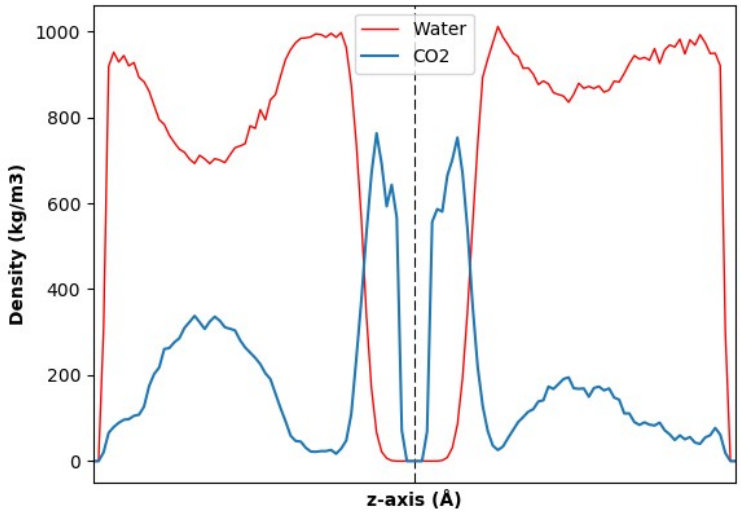

Figure 5.4: Density profile of the snapshot in figure 5.3. The dashed line represents the graphene wall.

5.2 Initial conditions used to investigate nanotube capacity

This section presents the system set-up that is designed so as to evaluate the goals in part 2 of this project. The goal with part 2 is to evaluate the capacity of the nanotube as a function of nanotube size and driving forces in the water-CO2 mixture container.

5.2.1 Description of the system set-up used to study nanotube capacity

Figure 5.5 shows the system set-up that was designed for the simulations in part 2. A result from the simulations in part 1, was the CO2 limitation in the water-CO2 mixture so that the desired quasi-equilibrium conditions could not be reached. The desired quasi-equilibrium conditions is a steady-state condition where the net flow of CO2 molecules from the waterCO2box, through the nanotube and into the CO2box stops while there is still plenty of CO2 molecules available in the water/CO2 mixture (waterCO2box). Therefore, the simulation system used in part 1 needed to be modified. In part 2, two changes were made on the simulation systems compared to part 1.

The first change is that in part 2, the water and CO2 molecules in the water-CO2 mixture container are initially packed into two layers. The first layer consists of pure water and the second layer of pure CO2. This is done so that there is a layer of pure CO2 near the nanotube entrance to have enough CO2 molecules available while there still is a water layer in contact with the CO2 layer to preserve the water/CO2 interface. By doing so, a neglectable amount of water molecules trajected into the receiving tank.

The second change is that in the simulations in part 2, the left graphene wall of the water-CO2 container moves each time step. This is done to control the driving forces in the waterCO2box. The main idea by moving the moveable wall each time step is that as CO2 molecules flow from the waterCO2box, through the nanotube and into the CO2box, something must replace those molecules, otherwise both the mechanical and chemical driving force in the water-CO2 mixture container would mitigate. Thus, the moveable wall moves each timestep to compress the CO2 molecules in the CO2layer control region so that the density in the CO2layer control region is maintained. Note that there is a difference between the “CO2 layer” and the “CO2layer”, as seen in figure 5.5. The CO2layer is the 20 Å control region while the CO2 layer is the whole layer of CO2 molecules that stretches from right graphene wall of the water-CO2 mixture container to the water/CO2 interface.

A mass flow rate conservation equation was used to move the wall. Moving the wall based on this principle made it possible to keep the density of CO2 molecules in the CO2layer control region in the waterCO2box constant. Keeping the density of the CO2layer constant was necessary for the system to fully saturate the receiving tank (CO2box) with CO2 molecules as a function of nanotube size and driving forces in

water-CO2 mixture container. And hence, the system could reach the desired quasi-equilibrium conditions. The CO2layer is defined in figure 5.5 b) as a 20 Å control region where the mass flow rate is calculated. Same for the 20 Å nanotube control region. Both the CO2layer region and nanotube region are dynamic regions. This means that the current CO2 molecules present in the region were updated each time step, implying that both the density and the mean velocity varied with time in the two regions. The idea was to try to control the density of CO2 in the CO2layer control region in such a way that it fluctuated naturally around a constant average density. The mass flow rate conservation equation that was coded into the LAMMPS input run script is defined as:

$$\rho_1 \bar{\bar{v}}_1 A_1 = \rho_2 \bar{\bar{v}}_2 A_2 \tag{5.1}$$

where *1* represents the CO2 molecules in the CO2layer control region and *2* represents the CO2 molecules in the nanotube control region. ρ is density and $\bar{v}$ is mean velocity of the CO2 molecules in the respective control regions. A_1 is the xy-area of the CO2layer, which is the same as the surface area of the graphene walls with an area of 51.577x51.048 Å^2. A_2 is the cross-sectional area of the nanotube. In equation (5.1), $\bar{v}_1$ is the velocity the wall must have to compress the CO2 molecules in the CO2layer region to keep the density this region constant. The 20 Å nanotube control region was located at 1 Å inside the nanotube and stretched for 20 Å into the nanotube in z-direction. Margins of 1 Å and 20 Å were kept so that the calculated mean velocity and density in the nanotube would not be so affected by fluctuations in/out of the left nanotube entrance. In addition, a 20 Å margin between the CO2layer and the nanotube was kept because within that 20 Å margin, the flow dynamics highly affect the density of the CO2 molecules. The CO2layer is more like CO2 bulk, but still, it is affected by e.g. flow dynamics, water/CO2 interface and graphene walls.

There are two reasons why equation (5.1) and the two control regions were applied to make the wall move. The first reason was to keep the CO2 density in CO2layer constant on average. The density will fluctuate, and it will always fluctuate because this is a molecular simulation system, but the simulation results show that the mean density actually is very constant (for 3 out of 4 simulations). This will be discussed in the next chapter. The second reason to move the wall this way, is that with this method to keep the density of CO2 in CO2layer constant, the wall has a decrease in velocity and it eventually stops (or just fluctuate around the same z-position) as the quasi-equilibrium conditions are reached. When the quasi-equilibrium point is reached, there will be no net flow of CO2 molecules in the nanotube, thus the mean velocity of the CO2 molecules in the control region in nanotube is net almost zero.

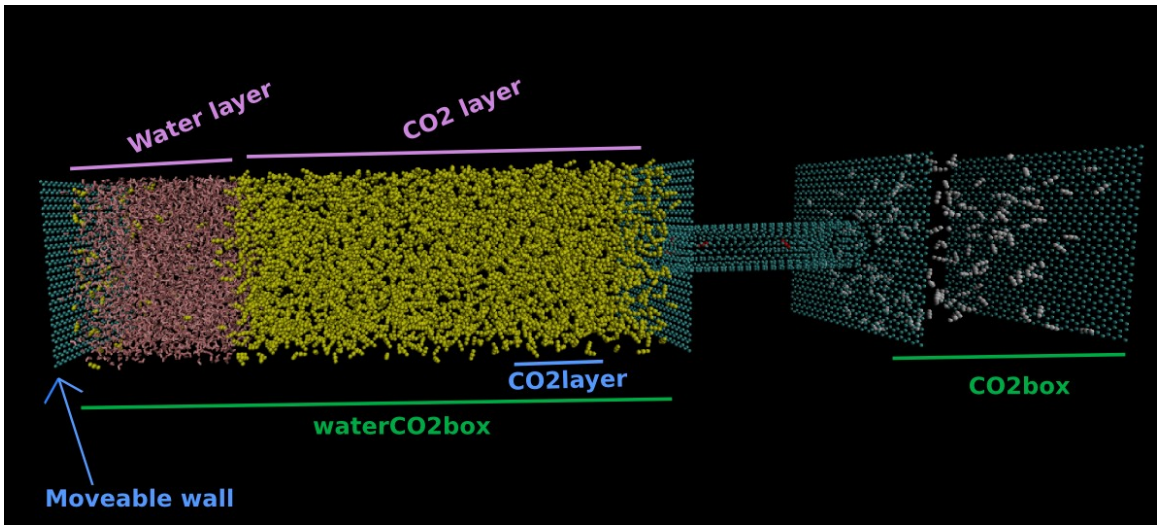

a) Simulation system set-up in part 2. The initial start configuration (after 20 ns equilibration). Simulation time: 0 ns. Regions are defined, making it easier to discuss the system.

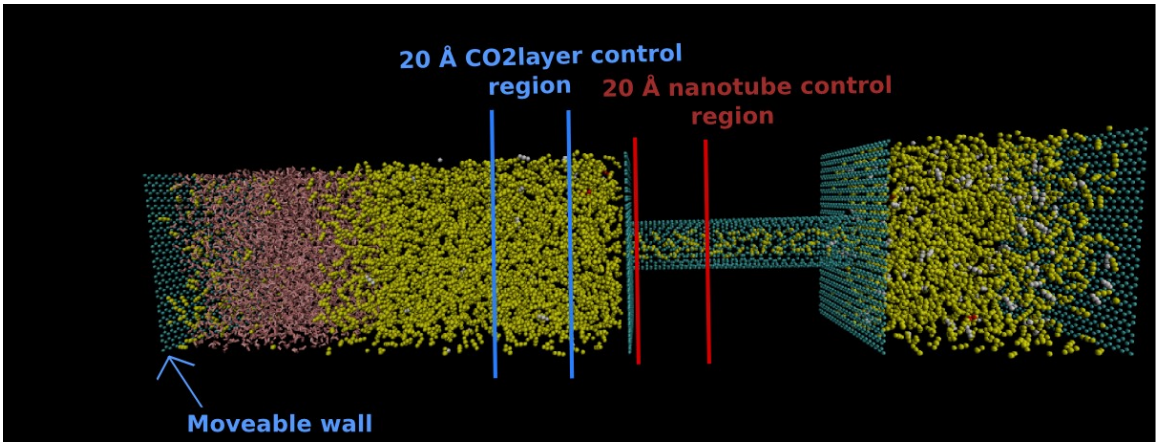

b) Simulation system set-up in part 2. Simulation time: 30 ns. The moveable wall has moved net towards nanotube. Shows the two control regions where the mass flow rate was calculated to move the movable wall.

Figure 5.5: Visualization of the system set-up in part 2. CO2 molecules are colored in yellow, red and white, based on initial position in different regions. Water molecules are colored in pink. Carbon atoms in the nanotube and the graphene walls are colored blue.

Chapter 5.2.2: The four simulations in part 2

Table 5.4 shows the four simulations conducted in part 2 of this research project with the corresponding two independent variables. The first factor was the nanotube size. Two nanotube sizes have been simulated: a (10,10) nanotube and a (20,20) nanotube. The second independent variable was the density of the CO2 in the CO2layer control region in the water-CO2 mixture container. This density was constant on average with a mass flow rate conservation principle using equation (5.1). By using the density of CO2 in CO2layer as a independent variable, the idea is that the system can be simulated for different driving forces in the water-CO2 mixture container to see how they affect the flux of CO2 through the nanotube into the receiving tank and also the chemical potential of CO2 in nanotube. The driving forces in the water-CO2 mixture container are assumed to be controlled by the density of CO2 in the CO2layer control region.

Table 5.4: Declaration of the two independent variables for the four simulations in part 2 - nanotube size and driving force in the water-CO2 mixture container.

Simulation nr.	Nanotube size	Driving force of CO2 in water-CO2 mixture container
Simulation 1	(10,10)	Liquid CO2 in CO2layer
Simulation 2	(10,10)	Liquid CO2 in CO2layer
Simulation 3	(20,20)	Gas CO2 in CO2layer
Simulation 4	(20,20)	Gas CO2 in CO2layer

The two densities of CO2 in the CO2layer that are simulated are a density of ~800 kg/m^3 and a density of ~150 kg/m^3. Those two densities were chosen because they represent two extreme scenarios. With a density of ~800 kg/m^3 at 298K, the CO2 will be in liquid phase. With a density of ~150 kg/m3 at 298K, the CO2 will be in gas phase. This phase behavior can be seen in figure 5.6. The bubble point density of CO2 at 298K is 712 kg/m^3 while the dew point density is 240 kg/m^3. Thus, for both of the simulated densites, there is a margin from the gas/liquid phase transition densities. And keeping a good margin is

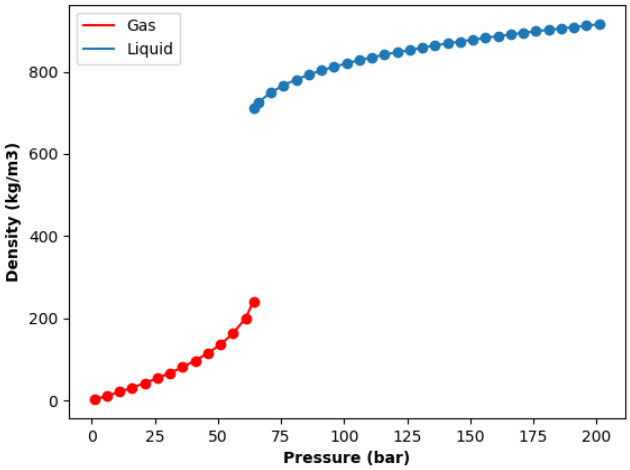

Figure 5.6: Plot of CO2 density vs pressure at 298K. From Span and Wagner EoS [56-57].

important because the density will fluctuate. It is also worth mentioning that the critical point for CO2 is at *(P,T)=(73bar,304K)*. Above the critical point for CO2, the CO2 will be in supercritical phase. The critical point will most likely be avoided in the simulation because the temperature is kept constant at 298K with a thermostat. Or, more precisely, because this is molecular dynamics simulation, the applied thermostat algorithm will keep the temperature fluctuating around the mean value 298K, with minor fluctuations.

Table 5.5 lists the number of water and CO2 molecules used in each simulation in part 2. The z-size of the waterCO2box for all the four simulations were 170 Å in z-direction.

Table 5.5: The number of water and CO2 molecules initially in the different regions of the system in all the four simulations conducted in part 2.

Simulation nr.	N_{water} in waterCO2box	N_{CO2} in waterCO2box	N_{CO2} in nanotube	N_{CO2} in CO2box
Simulation 1	3670	3500	4	146
Simulation 2	3670	3500	35	146
Simulation 3	3670	900	4	146
Simulation 4	3670	900	35	146

The initial pressure gradients listed in table 5.6 can give an indication on the relative pressure gradient across the nanotube for simulation 1-2 compared to simulation 3-4 in part 2. They are calculated using Span and Wagner equation of state [56-57] on both the water-CO2 mixture container and the receiving tank with their respective initial CO2 densities. Most likely, this is not the real driving force pressure in the simulation because there are so much happening in the waterCO2box with e.g. phase separations, water-CO2 interface and graphene wall surfaces.

Table 5.6: Initial pressure gradient across the nanotube for the four simulations in part 2. Calculated with Span and Wagner equation of state [56-57].

Simulation nr.	Initial pressure gradient
Simulation 1	55 bar
Simulation 2	55 bar
Simulation 3	17 bar
Simulation 4	17 bar

All the four simulations in part 2 were simulated with the same procedure. First, the water and CO2 molecules in the waterCO2box were packed into a water layer and a CO2 layer with Packmol [58]. Also, the CO2 molecules in nanotube and CO2box were packed randomly with Packmol. Then, the four systems were equilibrated for 20 ns with a blocked nanotube. The equilibration simulation was necessary to let the water and CO2 layer stabilize. The result from the 20ns equilibration process for system 1 is shown in figure 5.5 a). Then, the simulation was restarted from the 20 ns time frame, but this time with an open nanotube. What the blocked and open nanotube means, is illustrated in figure 5.7. A small, radial graphene sheet, colored red, is located at each nanotube entrance in the inner nanotube diameter. In the equilibration process with blocked nanotube, the small, radial graphene sheets block the nanotube for molecular flow. Thus, no water or CO2 molecules can enter/leave the nanotube. With blocked nanotube, the small, radial graphene sheets have the same 1/10 tune down interaction parameters as the large blue graphene walls. With open nanotube, molecules can traject in/out of the nanotube. This is because the Lennard-Jones interaction parameters of the small, radial graphene sheets are turned off, sat to 0.0, so that they have no interactions with any components of the system.

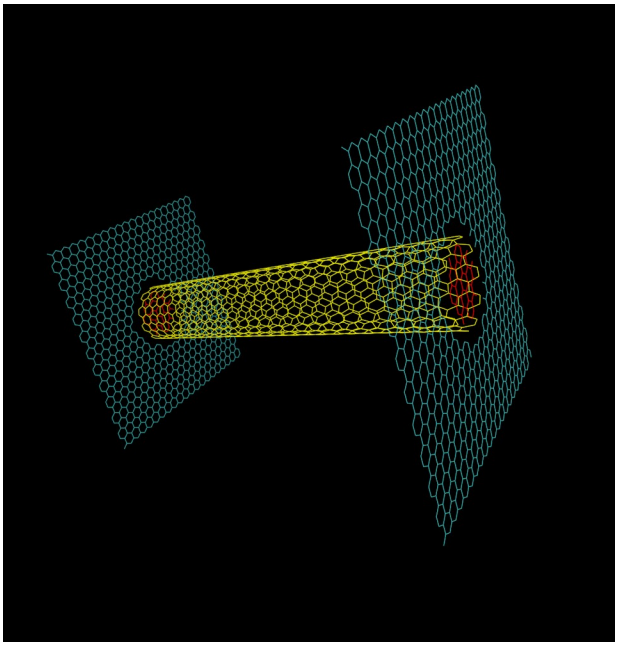

Figure 5.7: A zoom in on the (10,10) nanotube in figure 5.5 a) to illustrate open/blocked nanotube, a concept used to equilibrate the systems in part 2. The coloring represents one yellow nanotube, one blue graphene sheet at each nanotube entrance, and one red radial graphene sheet at each nanotube entrance.

6 Molecular interaction models

In the main simulation systems conducted in this project, there were three components: water, CO2 and graphene. For each of those components, a large variety of molecular interaction models (force fields) exist, and sometimes it is not so easy to know what model to use. The simulation models that are chosen in this project are chosen because they are recognized in the research community and they have also shown good results with experimental data on areas that are considered to be important for this project. No simulation model is good at everything. Each model has its set of strengths and weaknesses.

6.1 CO2 model

The CO2 force field interaction parameters were taken from the EPM2 semiflexible Harris & Yung 1995 CO2 model [59]. The EPM2 semiflexible CO2 model is a recognized CO2 model, and it has given good simulation replication to experimental vapor-liquid phase equilibrium conditions for CO2 up to the critical point [60]. It also accurately reproduces the zero-coverage isosteric heat of CO2 adsorption in carbon nanotubes [61]. The EPM2 CO2 model is a three-site model, meaning that each site is described by a Lennard-Jones potential and that each site has a partial Coulombic charge.

Figure 6.1 shows an illustration of the EPM2 semiflexible CO2 molecule, visualized in Visual Molecular Dynamics (VMD) [62]. The two red atoms are oxygen and the green atom is carbon. There are double bonds between the oxygen and carbon atoms. This is a snapshot of a CO2 molecule from one of the simulations done in this project. The bonds are slightly bent, thus the angle is not exactly 180 degrees, illustrating how the angle bending of the EPM2 semiflexible model works. The angle will oscillate slightly around the equilibrium angle of 180 degrees. The bond lengths are rigid.

In table 6.1 and 6.2, the EPM2 semiflexible CO2 model parameters are listed. The EPM2 semiflexible has rigid bonds. By using the *fix shake* algorithm it is possible to keep the bonds in a CO2 molecule rigid in LAMMPS.

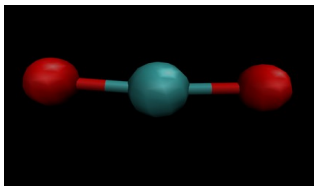

Figure 6.1: Visualization of a EPM2 semiflexible CO2 molecule.

Table 6.1: EPM2 semiflexible CO2 model force field interaction parameters [59].

Lennard-Jones 12-6 Parameters			Charge Distribution	
Atom	**ε [K]**	**σ [Å]**	**Atom**	**q [e]**
C_{CO2}	28.129	2.757	C_{CO2}	+0.6512
O_{CO2}	80.507	3.033	O_{CO2}	-0.3256

Table 6.2: Angle parameters for EPM2 semiflexible CO2 model [59].

Bond parameters		Lennard-Jones 12-6 parameters		
Bond	**r [Å]**	**Angle**	**K_θ [kJ/mol/rad^2]**	**θ [degrees]**
C_{CO2}-O_{CO2}	1.049	O_{CO2}-C_{CO2}-O_{CO2}	1236	180

6.2 Water model

For the water molecules, the SPC flexible water model [63] was chosen. This is a flexible simple point charge water model, meaning that each atom has a charge that is located in the center of the atom. This water model is fully flexible, meaning that the angle between the atoms can bend and the bonds can stretch. The SPCFw is recognized and has been widely used in MD simulations with good replications of experimental data [64-65].

In figure 6.2, the SPC flexible water molecule is visualized in VMD. The two gray atoms are hydrogen and the red atom is oxygen. There is a single bond between the hydrogen and oxygen atoms. The SPC flexible water model parameters are shown in table 6.3 and 6.4.

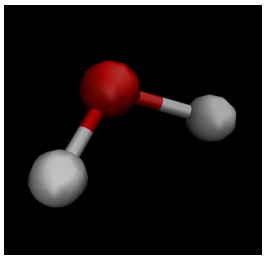

Figure 6.2: Visualization of a SPC flexible water molecule.

Table 6.3: SPC flexible water model force field interaction parameters [63].

Lennard-Jones 12-6 Parameters			Charge Distribution	
Atom	**ε [K]**	**σ [Å]**	**Atom**	**q [e]**
O_w	0.65	3.165	O_w	-0.82
H_w	0.0	0.0	H_w	+0.41

Table 6.4: Bond and angle parameters for SPC flexible water model [63].

Bond parameters			Angle parameters		
Bond	**Kr [kJ/mol/Å^2]**	**r [Å]**	**Angle**	**K_θ [kJ/mol/rad^2]**	**θ [degrees]**
O_w-H_w	4421.53	1.012	H_w-O_w-H_w	317.57	113.24

6.3 Graphene and carbon nanotube model

In 1991, Sumio Iijima from Japan discovered the first carbon nanotube [66-67]. A quote said by Iijima himself:

"In June, 1991, I found an extremely thin needle-like material when examining carbon materials under an electron microscope. Soon thereafter the material was proved to have a graphite structure basically, and its details were disclosed. I named these materials "carbon nanotubes" since they have a tubular structure of carbon atom sheets, with a thickness scaled in less than a few nanometers." [67]

Since then, researchers have had great attention to nanotubes because of their unique fluid transport properties. They have also shown excellent mechanical strength and conductivity [68-69]. Researchers have considered nanotubes for a wide range of industrial applications: e.g. in batteries, as transistors and as gas sensors [70]. Nanotubes have also previously been evaluated in different molecular selectivity and separation processes with great success in areas such as gas separation, water purification and water desalination [71].

Both the nanotube and graphene sheet have just one component, namely carbon atoms. The diameter of a nanotube is determined by its chiral factors (m,n), which determines how the one-atom thick graphene sheet is rolled into a one-atom thick nanotube and the resulting nanotube diameter. In this work, armchair nanotube was used. A produced nanotube used in experiments or industrial applications always has some defects. It will never be perfect. For example, both the produced radial sizes and the hexagonal structure

of the carbon atoms vary. However, in the simulations conducted in this project, ideal nanotubes with no defects were used.

Figure 6.3 a) shows a (10,10) nanotube and b) shows a (5,5) graphene sheet. They are both created in and visualized in VMD. They are visualized with lines, where all the intersects of the hexagonal structure are carbon atoms. The (10,10) nanotube contains 1000 carbon atoms, has a diameter of 13.54 Å and, in this case, is 60 Å long. The (5,5) graphene sheet contains 1008 carbon atoms and has a xy-surface area of ~(50.0x50.0) $Å^2$. The force field parameters used for graphene was taken from [72], and they are shown in table 6.5. Those parameters have been widely used among other researchers in the study of systems where carbon nanotubes and graphene surfaces are present [73-74]. In this work, both the graphene sheets and nanotubes were simulated as rigid structures, meaning that their carbon atoms do not move while they still will have Lennard-Jones 12-6 potentials with the other components of the system.

Note that the carbon atoms in the nanotube and graphene sheet are neutrally charged, thus they do not have any electrostatic interactions. They only interact with the other system components through vdw forces.

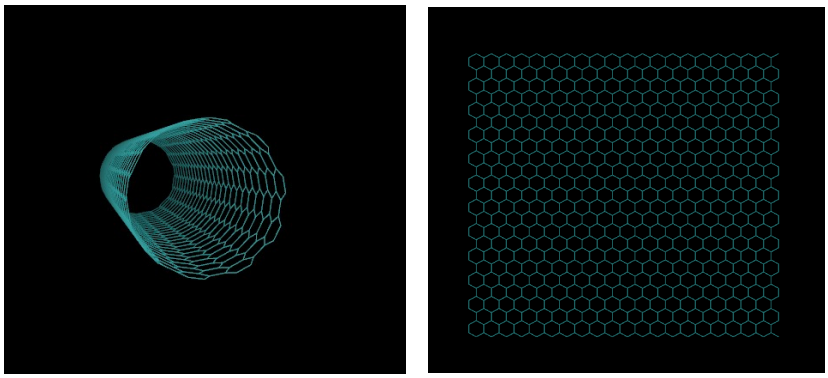

a) **b)**

Figure 6.3: a) (10,10) carbon nanotube. b) (5,5) graphene sheet.

Table 6.5: Graphene force field interaction parameters [72-74].

Lennard-Jones 12-6 parameters			**Charge distribution**	
Atom	**ε [K]**	**σ [Å]**	**Atom**	**q [e]**
$C_{graphene}$	28	3.4	$C_{graphene}$	0.0

6.4 Combination rules

The EPM2 semiflexible CO2 model, SPCFw water model and graphene model were used for interactions between components of similar type. Lorentz-Berthelot mixing rule was applied on the system components of dissimilar type. The main drawback by using the Lorentz-Berthelot mixing rule is that it is non-physical [75-76]. But then, why is it used in this work? The thing is that it is widely used among researchers [75]. Also, good models for water-CO2 mixture, water-graphene and CO2-graphene do not really exist. Other mixing rules do exist, but Lorentz-Berthelot is the most common one [75]. Often, the Lorentz-Berthelot mixing rule can be used as an approximation. However, it is important to be critical with the results, and to evaluate if the mixing rule gave a representable result.

The Lorentz-Berthelot mixing rule is stated as below:

$$\sigma_{ij} = \frac{1}{2}\left(\sigma_i + \sigma_j\right) \tag{6.1}$$

$$\varepsilon_{ij} = \sqrt{\varepsilon_i \varepsilon_j} \tag{6.2}$$

where the energy well depth parameter ε_{ij} between atom i and atom j is calculated by geometric mean. The molecular size distance parameter σ_{ij} between atom i and atom j is calculated by arithmetic mean.

6.5 Reduction of graphene wall bias effect

In the main simulations conducted in this project (in both part 1 and 2), four graphene walls were used to make the system non-equilibrium with a pressure and a chemical gradient across the nanotube. This will be discussed more comprehensively later on, but for now, it was found necessary to reduce the bias effect those four graphene walls could have on the simulation results. To reduce the impact the graphene walls had on the water and CO2 molecules in the system, both the graphene–CO2 and graphene–water interactions were 1/10 tuned down.

Figure 6.4 shows the difference between a simulation with original graphene–CO2 interactions and a simulation with 1/10 scaled down interactions. Both systems contain two graphene walls normal to the z-direction, 300 CO2 molecules and a xyz-volume of *(51.577x51.048x52.0) Å*^{2}. The CO2 molecules were packed randomly with Packmol [58] Both simulations were simulated for 10 ns with NVT ensemble. Figure 6.4 a) is a

snapshot of the last time frame of the 10 ns simulation where the interactions are original. It can be observed that the CO2 molecules have a high preference to be near the graphene walls. In figure 6.4 b), the graphene–CO2 interactions are 1/10 tuned down. From a visual point of view, the 1/10 tune down has a tremendous positive effect. The amount of CO2 molecules adsorbed to the graphene walls is reduced significantly. To quantify the difference, the density of the CO2 molecules for both systems was plotted along the z-axis. The result can be seen in figure 6.5. The density is calculated with a resolution of 1 Å bins along the z-axis. The two, black, dotted lines represent the graphene walls. Also, from the density profiles, it can be observed that with the original graphene wall interactions, a large amount of the CO2 molecules adsorbed to the graphene walls. It can be explained by the non-polarity of both the graphene surface and the CO2 molecules and the strong CO2-nanotube vdw interactions. By tuning down the Lennard-Jones interactions the CO2 molecules have with the graphene walls, this adsorption effect was significantly reduced, resulting in a decreased preference for CO2 to be near the graphene walls, and making the CO2 distribution much more homogenous. For all the future simulations conducted in this master project, all the Lennard-Jones interactions the graphene walls have with the other components of the system, both water and CO2, will be 1/10 tuned down. On the positive side, the strong graphene-CO2 original interactions show the strong CO2 adsorption potential for the use of carbon nanotubes in the water/CO2 separation process. 1/10 scale down was chosen as a lower limit since the water and CO2 molecules cannot be permitted to escape through the graphene walls.

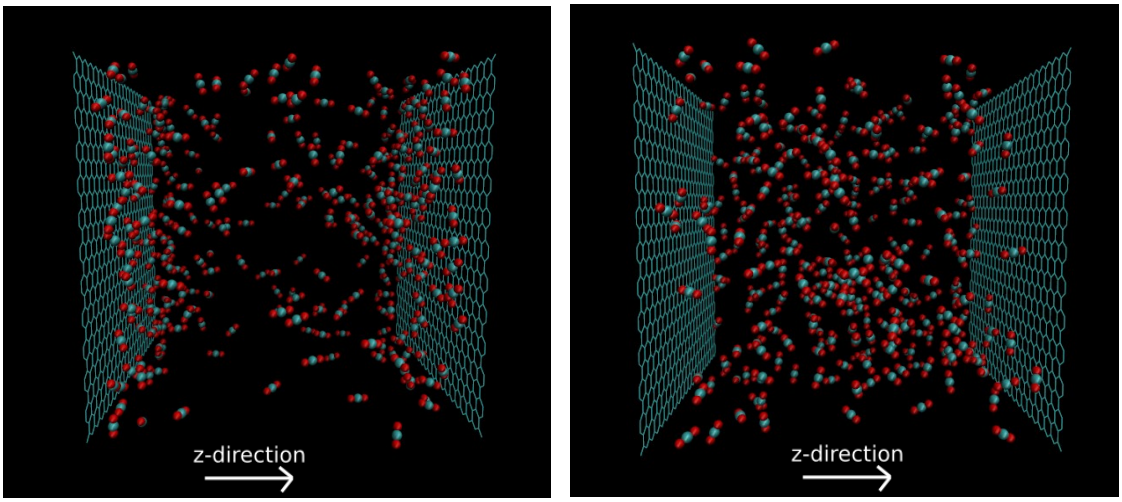

a) **b)**

Figure 6.4: Visualization of 10 ns simulation of CO2 molecules between two graphene walls with a) original interactions and b) 1/10 tune down interactions. The CO2 molecule is visualized as bonded red (oxygen) and blue (carbon) atoms. The two blue sheets are graphene walls.

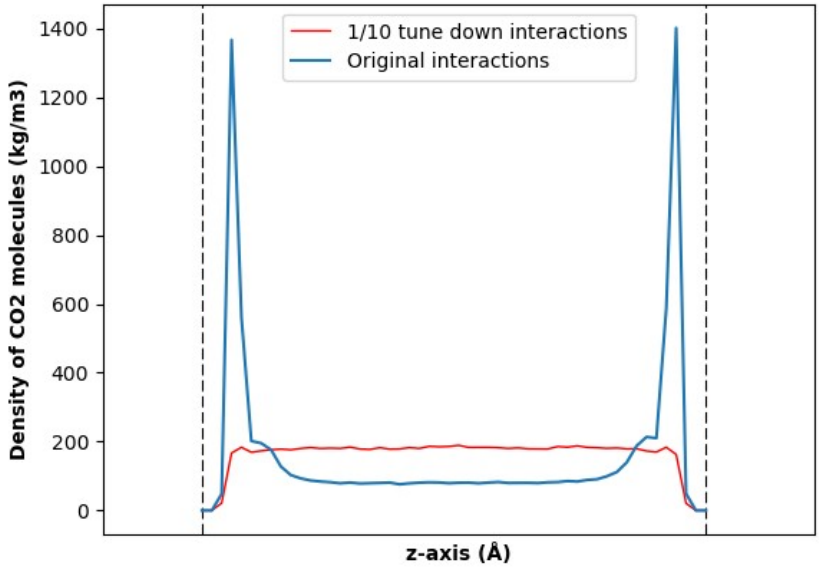

Figure 6.5: Density profile of the CO2 molecules in figure 5.1 a) and b). The two dotted lines represent the two graphene walls.

6.6 Computational details

LAMMPS simulation software [36] was used as a tool to evaluate the separation process. Packmol [58] was used to pack the nanotube/graphene walls into their rigid positions and to pack the initial start configuration of the water/CO2 molecules. Moltemplate [77] was used to generate *.data*, *.in.init* and *.in.settings* files to be run with LAMMPS based the *.xyz* file from Packmol and a *.lt* file containing molecular force field parameters.

For all the main simulations in part 1 and 2, the Verlét algorithm was used to time integrate the system. The Verlét Algorih was implemented in LAMMPS using the function *fix NVE*. Two Berendsen thermostats [48] were applied to the system, one for the water-CO2 mixture container and one for the receiving tank, to control the temperature to be 298 K in both boxes. This was done to have no temperature gradient across the nanotube. Both thermostats are region based in z-direction and are 2 Å distance from the graphene walls in each box (on the inside). The goal with the thermostats was also to achieve a canonical ensemble NVT distribution at equilibrium conditions. The thermostat coupling parameter was chosen to be 100 timesteps.

The timestep for each simulation was *1 femtoseconds = 10^{-15} seconds*. The dump frequency was set to be 1000, meaning that the trajectories of the molecules in the system were dumped to a *.dcd* file each 1000 timestep.

A cut-off distance of 12.0 Å was used for the short-range (Lennard-Jones 12-6) interactions. Particle-Particle Ewald Mesh Summation (PPEMS) was used to calculate the long-range (electrostatic) interactions, with a cut-off equal 0.0001.

The nanotube was 60 Å long in z-direction in all simulations, both in part 1 and 2. All the simulations had a xy-area of *(51.577x51.048) $Å^2$*, which made it possible to have a perfect connection between the graphene walls over the periodic boundary conditions in xy-direction. In xy-direction, both the waterCO2box and CO2box stretch out for infinity over the periodic boundary conditions. In the z-direction, there was a 20 Å length of vacuum between the waterCO2box and the CO2box over the periodic boundary conditions to mitigate the graphene-graphene interactions between the graphene walls.

All the simulations, both in part 1 and 2, were simulated for 30 ns.

7 Results and discussion

This section presents the simulation results obtained in this work. The results from the four simulations in part 1 are discussed in chapter 7.1 and those of the four simulations in part 2 are discussed in chapter 7.2. Combined, parts 1 and 2 provide valuable insight into the water/CO2 separation process by means of carbon nanotubes in terms of selectivity (evaluated in part 1) and capacity (evaluated in part 2). Selectivity and capacity are two absolute essential characteristics in the evaluation of a possible adsorption material. The fact that our simulations were performed using a molecular dynamics simulation tool like LAMMPS, make it possible to investigate how the separation process occurs on a molecular level.

All the mean and standard deviation values presented in both tables and plots in chapter 7 have been calculated using the block average method [78]. For each 10000 timestep, the sampled values of the 100 last timesteps are averaged. By doing so, the overall mean value is averaged over uncorrelated values, and thus, the mean value and the standard deviation provide a better representation of fluctuations in the sampled data.

7.1 Water/CO2 separation with carbon nanotubes

The goal with the four simulations performed in part 1 was to evaluate the impact of nanotube size and initial pressure gradient across the nanotube on CO2 selectivity and the risk of water entrainment. Both of the independent parameters, the nanotube size and the initial pressure gradient across the nanotube, represent two extreme scenarios. Two extreme scenarios were chosen so that differences and similarities could more easily be observed. This choice also made it possible to gain a better understanding which of the two factors might be crucial for the separation process.

Table 7.1 summarizes the independent variables used in the four simulations conducted in part 1. Two different z-sizes of the waterCO2box were used to evaluate the separation process at two different initial pressures of the non-equilibrium water-CO2 mixture.

Table 7.1: The four simulations conducted in part 1.

Simulation nr.	Nanotube size	z-size of waterCO2box
Simulation 1	(10,10)	122 Å
Simulation 2	(20,20)	122 Å
Simulation 3	(10,10)	112 Å
Simulation 4	(20,20)	112 A

While the simulations conducted in part 1 of this research project were very similar in terms of system set-up, varying the two independent parameters resulted in dramatically different outcomes. Therefore, we will first present and compare the main observations from the four simulations. The visualization of the time evolution of the system is arguably the most fundamental way to get a general estimate on the separation process efficiency. Secondly, the visual observations will be supplemented with a discussion of the forces driving in the separation process. The theory behind the driving forces is basically the same for all the four simulations, but due to the variation in nanotube size and initial pressure gradient, the outcome will vary. Thirdly, the selectivity and water risk for all the four simulations will be compared and discussed to evaluate the separation process as a function of nanotube size and initial pressure gradient across the nanotube. Finally, the main observations from the separation process will be discussed from a larger perspective by comparing them with previous studies.

7.1.1 Visual observations of the separation process

For all the four simulations in part 1, it was mostly carbon dioxide molecules that left the water-CO2 mixture container (aka the waterCO2box), passed through the nanotube, and entered the receiving tank (CO2box). This trend can clearly be seen in figures 7.1-7.4 produced by means of the VMD package. The nanotube and graphene walls are colored blue. The water molecules are in pink. The coloring of CO2 molecules is based on their initial positions. The yellow-colored CO2 molecules started in the waterCO2box. The red CO2 molecules were initially in the nanotube, while the white colored molecules were initially placed in the CO2box.

Consider simulation 1, which with the following parameters: a (10,10) nanotube and a 122 Å z-size waterCO2box. Immediately after the simulation started, two major processes could be observed. The first was the phase separations taking place in the waterCO2box. The water and CO2 molecules were initially evenly distributed, as seen in figure 7.1 a), and then they quickly re-organized, resulting in phase separation. Figure 7.1 b) shows how a portion of CO2 molecules collected near the graphene walls while the others formed a CO2 nanobubble. In figure 7.1 c), the nanobubble has grown larger, and so has the CO2 enrichment layer near the left graphene wall of the waterCO2box. The enrichment layer is even larger in figure 7.1 d), while the CO2 nanobubble is gone. The water molecules behaved quite differently. Figures 7.1 a)-d) show that water molecules form a hydrogen-bond water block. The second process that can be observed in figures 7.1 a)-d) is that there is a net flow of CO2 molecules from the water-CO2 mixture container, through the nanotube and into the receiving tank. Figure 7.1 b) also shows that as the simulation starts, CO2 molecules from both containers enters the nanotube together with a cluster of water molecules. In figure 7.1 c), the water cluster has travelled almost all the way through the nanotube, and there is a net flow of yellow CO2 molecules to the right. In figure 7.1 d), it can be observed that a great amount of yellow CO2 molecules has trajected into the CO2box and the water cluster has reached the receiving tank.

Simulation 2 in part 2 consists of the two independent variables: a (20,20) nanotube and a 112 Å z-size waterCO2box. Figure 7.2 shows the time outline of the system evolution. Visually, simulation 2 appears to be very similar to simulation 1 except for two differences. The first one is the behavior of water molecules. In simulation 2, a cylinder of water molecules had progressed about 1/4 of the nanotube at most, before fully retreating after ~4.1 ns. The second difference is in the number of CO2 molecules in the CO2box. Comparison of figures 7.1 d) and 7.2 d) shows that after 30 ns of simulation, there is a greater amount of CO2 molecules in the receiving tank in case of simulation 1 than simulation 2. On the other hand, there appeared to be more of CO2 molecules in the (20,20) nanotube in simulation 2 compared to the (10,10) nanotube of simulation 1.

Similarly, simulations 3 and 4 looked very much like simulations 1 and 2. The only difference that can clearly be observed by comparing figures 7.1-7.4, is the risk of water entrainment. Figures 7.1 b) and 7.3 b) show a larger water cluster entering the nanotube for simulation 3 compared to simulation 1. Also, the water cylinder has progressed further into the nanotube in simulation 4 than for simulation 2, as seen in figures 7.2 b) and 7.4 b). The higher water risk for simulations 3 and 4 may be related to the lower initial volume of waterCO2box, and hence, a higher pressure in the water-CO2 mixture.

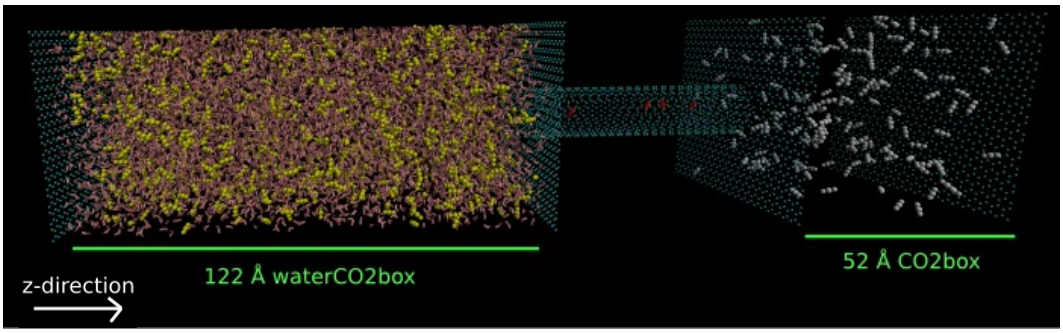

a) Simulation time 0 ns. The initial configuration.

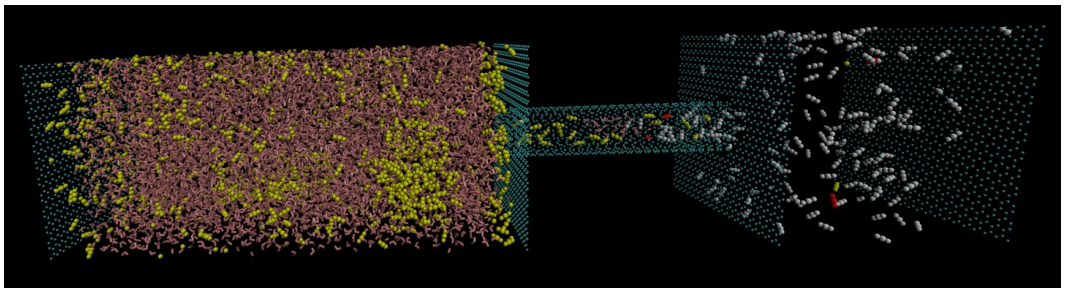

b) Simulation time 0.3 ns. Water cluster containing 26 water molecules in the middle of nanotube.

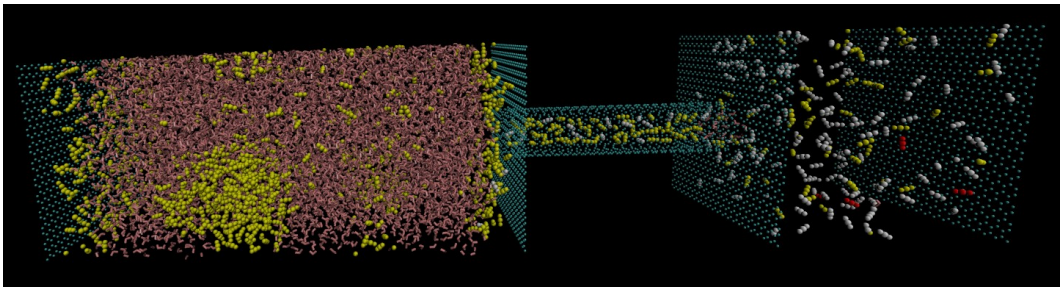

c) Simulation time 4.1 ns. Formation of CO2 nanobubble. The water cluster have reached CO2box.

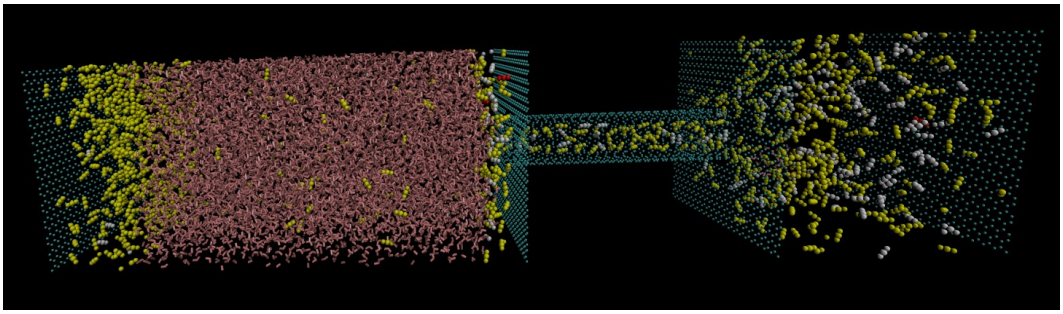

d) Simulation time 30.0 ns. Close to steady-state conditions, almost no net flow in nanotube. Nanobubble is gone. Water cluster still in CO2box.

Figure 7.1: Visual illustration with coloring of simulation 1 in part 1. Water molecules are colored pink. The coloring of CO2 molecules is based on initial region location. Yellow CO2 molecules initially in waterCO2box, red initially in nanotube and white initially in CO2box.

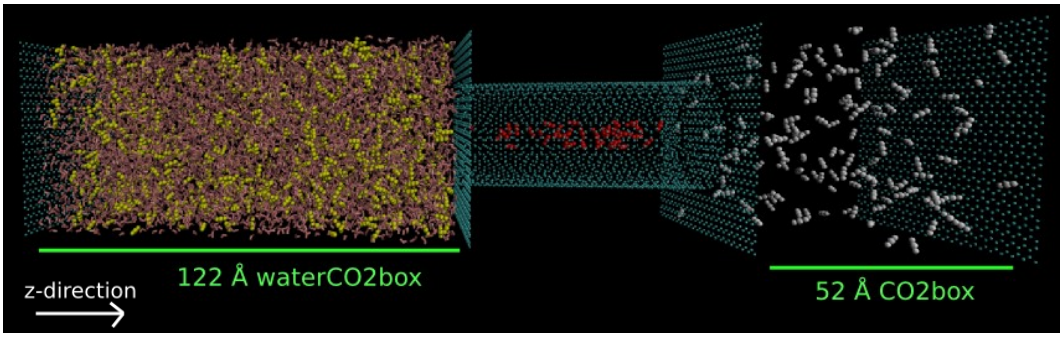

a) Simulation time 0 ns. The initial configuration.

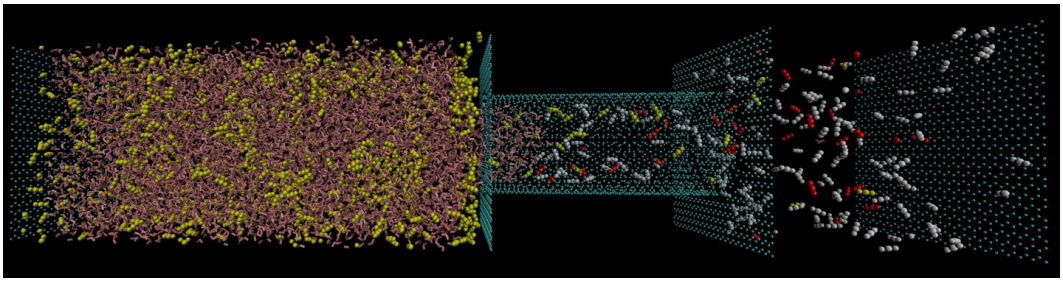

b) Simulation time 0.08 ns. Water tries to get into/or is pushed slightly into nanotube.

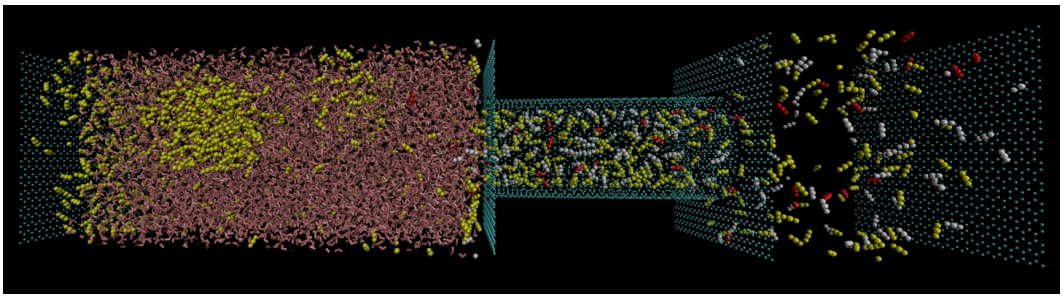

c) Simulation time 4.1 ns. Water has retreat from nanotube. Formation of CO2 nano bubble.

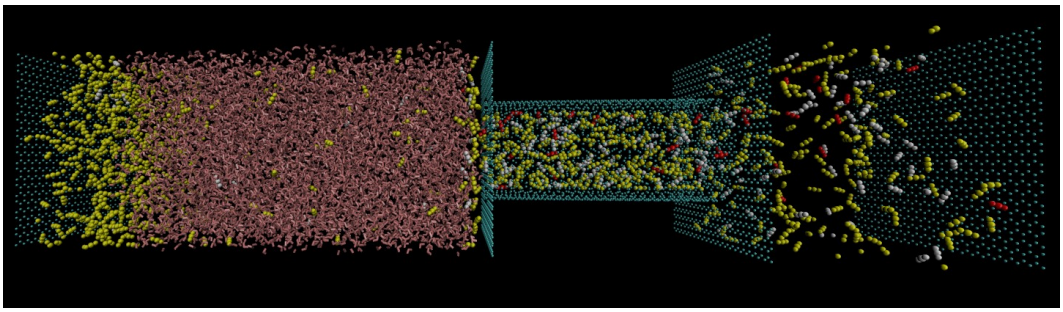

d) Simulation time 30 ns. Steady-state conditions and no net flow in nanotube due to lack of excess CO2 molecules available in the water-CO2 mixture.

Figure 7.2: Visual illustrating with coloring of simulation 2 in part 1.

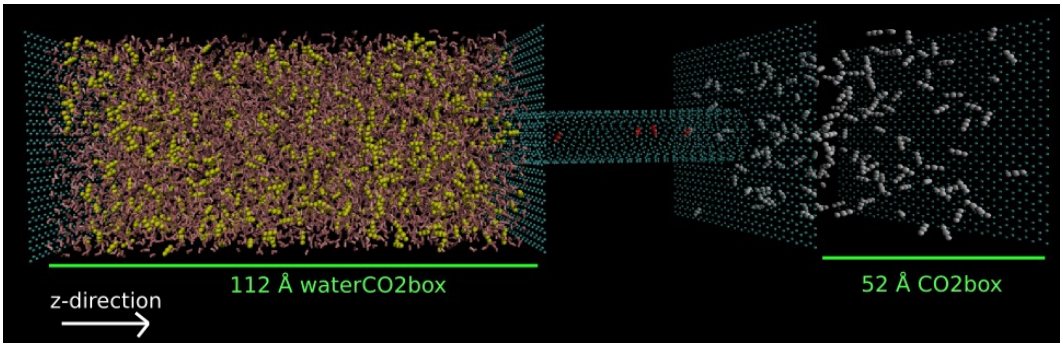

a) Simulation time 0 ns. The initial configuration.

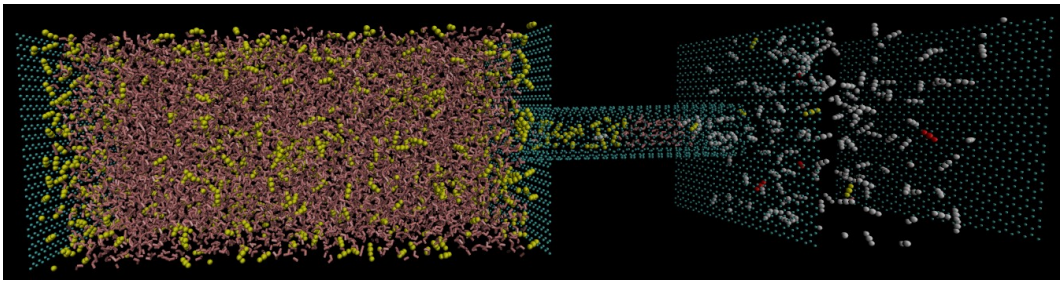

b) Simulation time 0.6 ns. Water cluster containing 76 water molecules in the middle of nanotube.

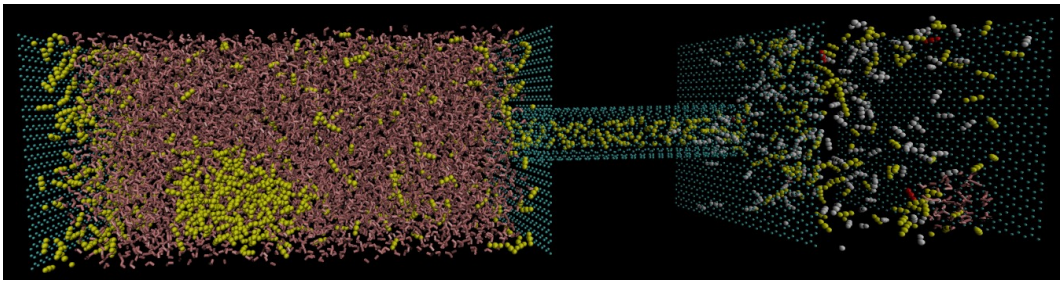

c) Simulation time 2.8 ns. Formation of CO2 nanobubble. The water cluster have reached CO2box.

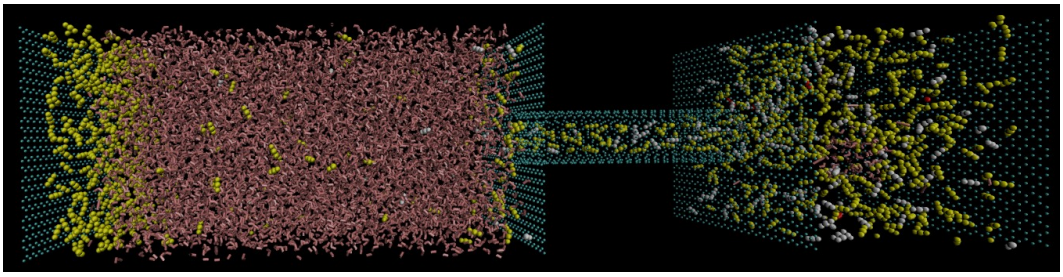

d) Simulation time 30 ns. Close to steady-state conditions, almost no net flow in nanotube. Nanobubble is gone. Water cluster still in CO2box.

Figure 7.3: Visual illustrating with coloring of simulation 3 in part 1.

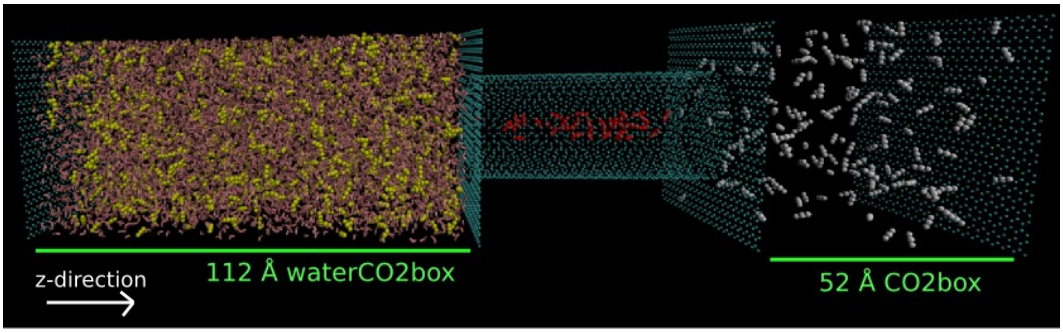

a) Simulation time 0 ns. The initial configuration.

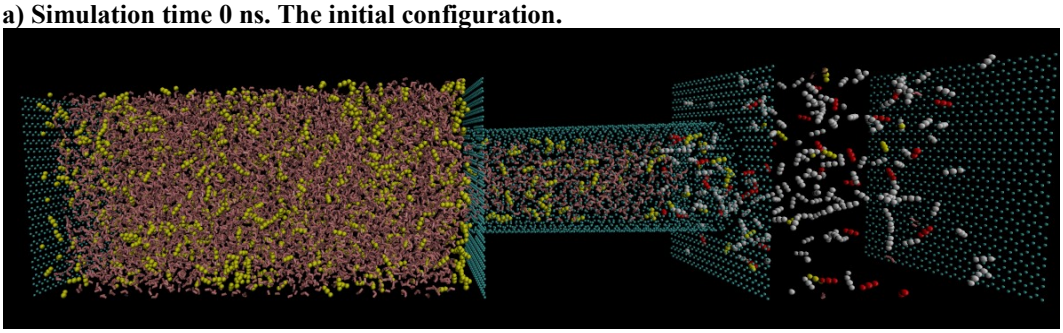

b) Simulation time 0.08 ns. A water cylinder has entered the ~3/4 of the nanotube.

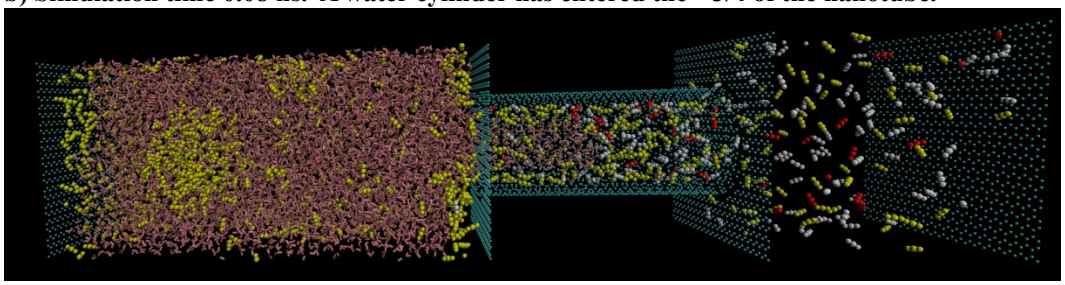

c) Simulation time 0.13 ns. The water cylinder never breaks through and retreats.

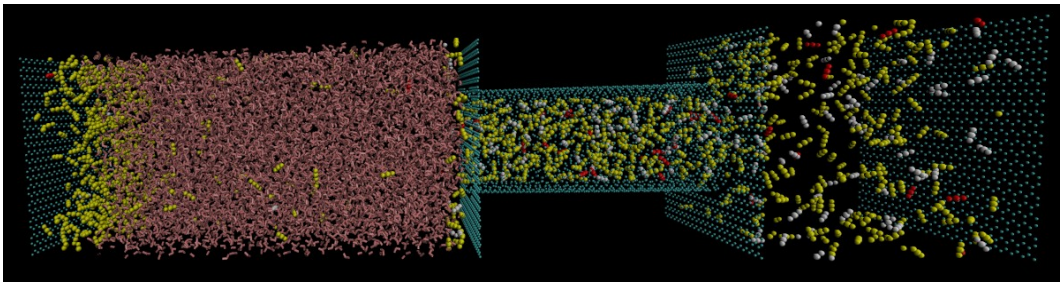

d) Simulation time 30 ns. Steady-state conditions and no net flow into nanotube due to lack of excess CO2 molecules available in the water-CO2 mixture.

Figure 7.4: Visual illustrating with coloring of simulation 4 in part 1.

7.1.2 Driving forces in the separation process

By evaluating the driving forces, it is possible to obtain a better understanding on why the separation process happens. There are two driving forces:

- mechanical work → results in “unspecific” flux
- chemical work → results in selective flux

First, let's consider the mechanical pressure driving force. The mechanical work is related to the pressure gradient across the nanotube. In both the water-CO2 container and the receiving tank, there is a pressure due to the thermal motion of molecules. As seen from figures 7.1-7.4, there exists a net flow of water/CO2 molecules from the waterCO2box into the CO2box. Therefore, it is reasonable to assume that the initial total pressure in the water-CO2 mixture container is higher than in the receiving tank.

The mechanical work will mainly contribute to molecular **flow**, i.e. the pressure gradient across the nanotube will achieve a net mass transfer involving both water and CO2 from the waterCO2box, through the nanotube and into the CO2box. But, it will not contribute to selectivity and water/CO2 separation. The mechanical work will just push both water and CO2 molecules through the nanotube. The net flow of CO2 molecules from the water-CO2 mixture container, through the nanotube and into the receiving tank can be observed visually in figures 7.1-7.4, as well as evaluating by tracking the number of CO2 molecules in receiving tank as a function of time (plotted in figure 7.5). The orange curve and the red curve in figure 7.5 a) represents the number of CO2 molecules in the CO2box vs time for simulation 1 and 3, respectively. Figure 7.5 b) plots the same for simulation 2 and 4.

The pressure gradient across the nanotube will decreases with time due to a net flow of CO2 molecules out of the waterCO2box and into the CO2box. However, the magnitude of the pressure gradient was found to be too challenging due to the absence of any meaningful pressure estimator due to the complexity and the number of processes simultaneously occurring in the system. As seen from figures 7.1-7.4, phase separation took place in all the four simulation systems within the time interval spanning 0 ns to 30 ns. Some examples of phases present included: CO2 adsorbed to graphene wall phase, CO2 forming a nanobubble, water/CO2 interface phase, and CO2 dissolved in the aqueous phase. The receiving tank is not as complicated as the waterCO2box, but it still presented a challenge since it contains at least two phases, i.e. the bulk CO2 phase and CO2 adsorbed onto the graphene wall. In addition, the pressure measurements were affected by the presence of water molecules in the receiving tank in case of simulations 1 and 3.

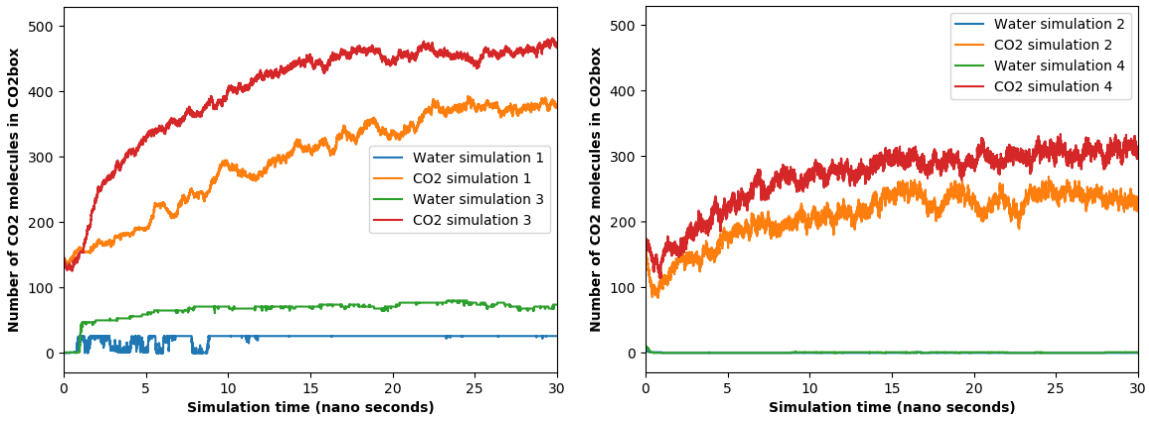

a) Simulation 1 and 3. **b) Simulation 2 and 4.**

Figure 7.5: Number of CO2 and water molecules in receiving tank vs time for simulations 1-4 in part 1.
Simulation 1 – (10,10) nanotube and initially a low pressure water-CO2 mixture.
Simulation 2 – (20,20) nanotube and initially a low pressure water-CO2 mixture.
Simulation 3 – (10,10) nanotube and initially a high pressure water-CO2 mixture.
Simulation 4 – (20,20) nanotube and initially a high pressure water-CO2 mixture.

The chemical work contributes highly to the water/CO2 separation process by means of the nanotubes due to both **flux** and **selectivity**. The chemical driving force can be interpreted in terms of two processes. The first one is related to phenomena taking place in the water-CO2 mixture container, with the second one to the chemical gradient across the nanotube. First, let's consider the water-CO2 mixture container. As seen from figures 7.1-7.4, several phase separation processes occur in the waterCO2box. The water molecules form a hydrogen-bonded water block due to strong water-water interactions. The hydrogen bonds are visualized in figure 7.6 a) in case for simulation 1 at 0.4 ns, and in figure 7.6 b) for simulation 2 at 0.8 ns. This strong preference for formation of the hydrogen bond networks can explain why the water molecules prefer to avoid trajecting into the nanotube where they will be hindered from forming many hydrogen bonds. The water molecules will rather stay in the waterCO2box surrounded by like molecules. The nanotube-CO2 interactions are much more advantageous than the water-nanotube ones, and combined with the strong water-water bonding, the CO2 molecules in the water-CO2 mixture will have a much higher affinity than water to adsorb into the nanotube despite being slightly larger in size.

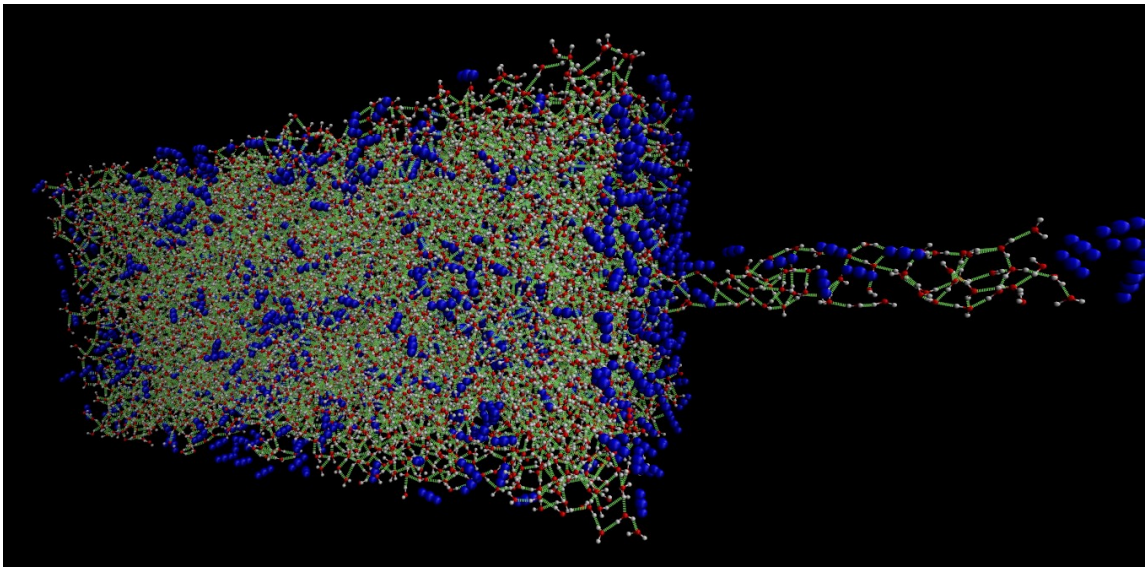

a) Simulation 1 in part 1. Simulation time 0.4 ns.

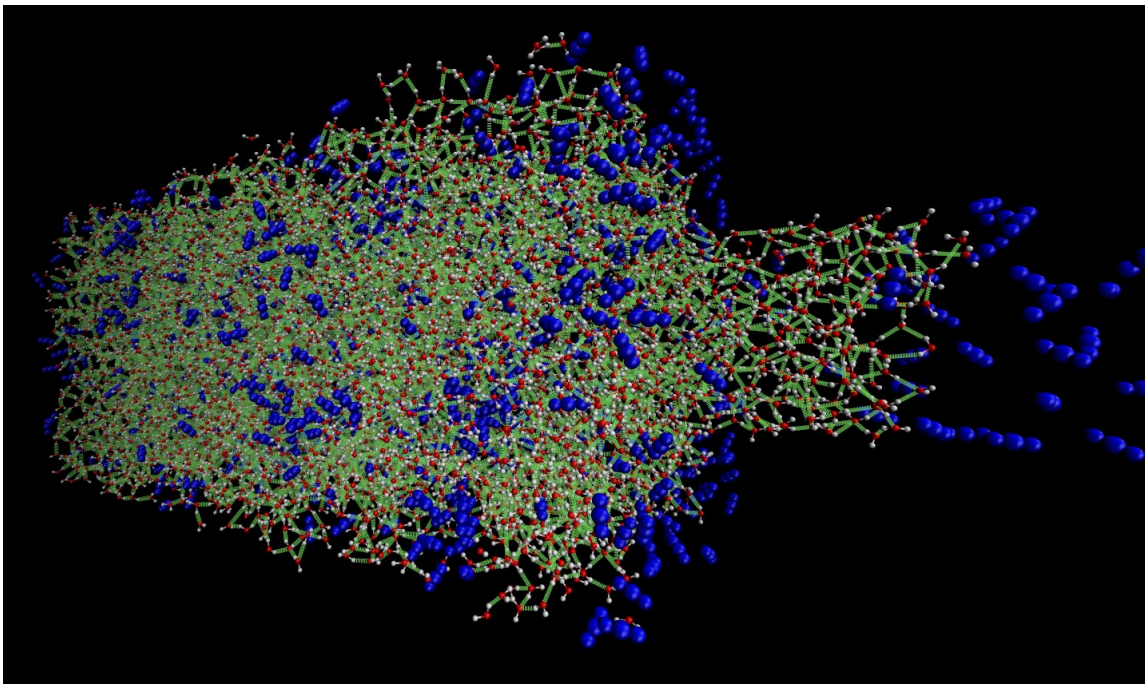

b) Simulation 2 in part 2. Simulation time 0.6 ns.

Figure 7.6: Visualization of hydrogen bonds between water molecules. Blue molecules are CO2. Red/white molecules are water. The green lines represent hydrogen bonds between water molecules.

The chemical driving force is also highly related to the amount of excess CO2 molecules in the bulk aqueous phase. Its time evolution is visualized and quantified in figure 7.7 for

simulation 2. At 0.4 ns, there is a concentration of ~9.5 mole% CO2 in water bulk, while at 30 ns, the CO2 concentration in water bulk drops down to ~0.8 mole%. The region between the two green bars in figure 7.7 a) is assumed to constitute the water bulk phase because the z-size of the water-CO2 mixture container was large enough for this region not to be overly affected by graphene walls. Another observation that could substantiate this claim that the amount of excess CO2 molecules in water bulk gives a high chemical driving force can be seen in figure 7.8. Figure 7.8 shows the water and CO2 density profile for the whole simulation system at a) 0.4 ns and b) 30 ns for simulation 1. The density profiles for simulation 2-4 are included in Appendix A in figure A.1. In figure 7.7a), it can be observed there is a high amount of excess CO2 molecules in water bulk, distributed as nanobubbles. In b), the amount of excess CO2 molecules in water bulk has decreased significantly. Comparing this observation with the CO2 flux profiles in figure 7.5, the same tendency for all the four simulations in part 1 is that at 0.4 ns, there is a high CO2 flux into the CO2box and a high concentration of excess CO2 in water bulk, while at 30 ns, then both the CO2 flux and the excess CO2 concentration are low. Initially, there is a concentration of 10 mole% CO2 in distributed evenly in water. 10 mole% is way above the equilibrium concentrations of CO2 in water. Preferably, the water wants to have a saturation concentration of CO2, and for simulation 2, that saturation concentration seems to be ~0.8 mole%.

The tendency of the aqueous phase to achieve the saturation concentration of CO2 is due to the minimization of Gibbs free energy. This happens because the water molecules prefer to be surrounded by other water molecules. Experimental studies have shown that a water molecule form ~3.4 hydrogen bonds on average in bulk liquid, and not exactly 4 due to continuously formation and breaking of the hydrogen bonds. This gives rise to two effects, both a force that makes CO2 move out of the water and a contribution to a strong affinity of the CO2 relative to water to adsorb into the confined nanotube channel. The way the phase separation of the water and CO2 molecules in the waterCO2box contribute to the chemical driving force can also be explained in terms of potential energy. Initially, at the start of the simulations, the water and CO2 molecules are randomly, evenly distributed in the waterCO2box. At this state, the water-CO2 mixture has a high potential energy because it is not favorable for neither water or CO2 molecules to maintain that distribution. Therefore, due to dissimilarities in polarity and interactions, the Gibbs free energy is minimized as the water and CO2 molecules phase separates with an initial 10 mole% CO2 concentration in water. The water molecules are polar with a strong dipole moment due to electronegativity and the non-linear shape, giving rise to hydrogen bond formation between other water molecules. CO2 molecule on the other hand is non-polar due to linearity, with a strong quadrupole moment. The phase separations can also be explained in terms of surface area minimization where the water/CO2 interface is minimized when excess CO2 molecules form a nanobubble or enrich near the graphene walls.

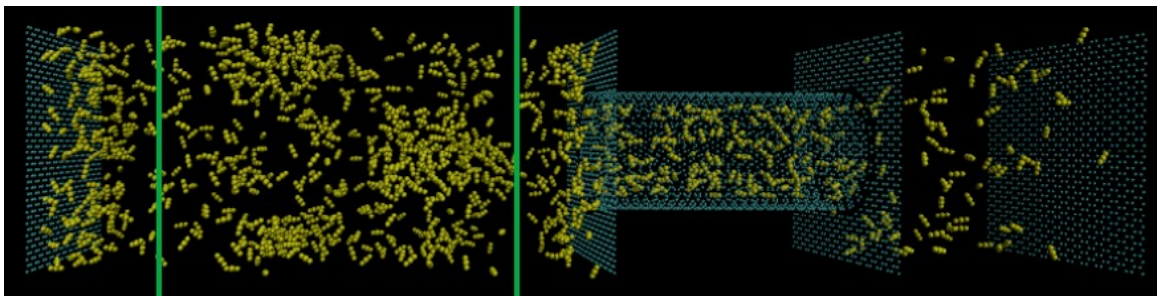

a) 0.4 ns. ~9.5 mole% CO2 in water bulk. Region between the two green bars is considered as water bulk.

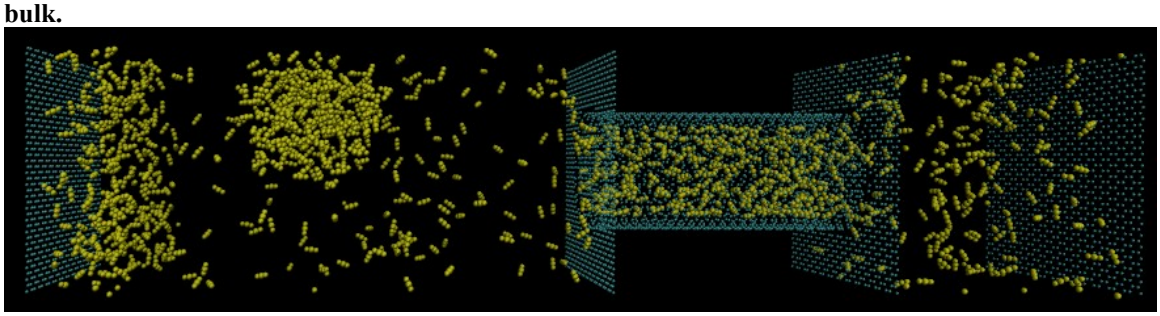

b) 5.7 ns. ~7.0 mole% CO2 in water bulk. A CO2 nanobubble in water bulk is formed.

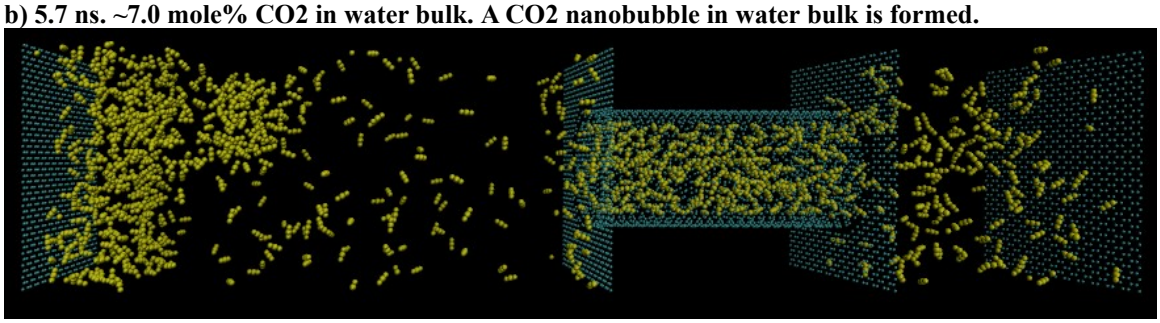

c) 9.7 ns. ~3.5 mole% CO2 in water bulk. Most CO2 molecules in nanobubble trajects to near the left graphene wall as it breaks.

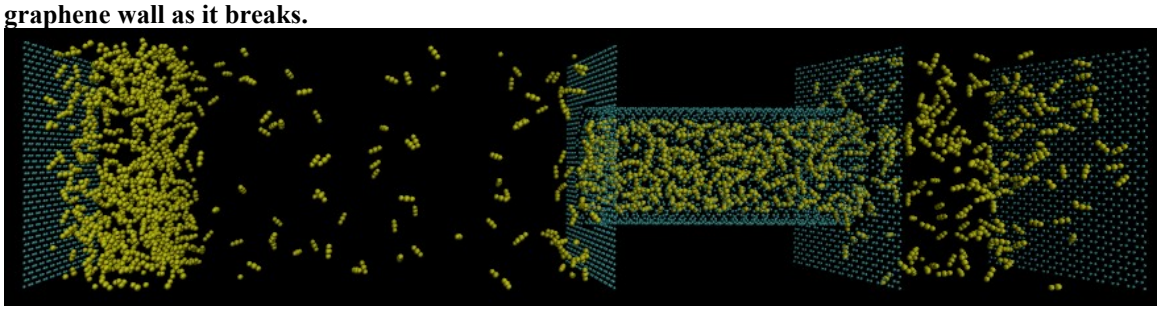

d) 30.0 ns. ~0.8 mole% CO2 dissolved in water bulk, about equilibrium concentration.

Figure 7.7: Visual illustration of how the chemical driving force of CO2 in waterCO2box decreased with simulation time. Simulation 2 in part 1. The CO2 molecules are colored yellow.

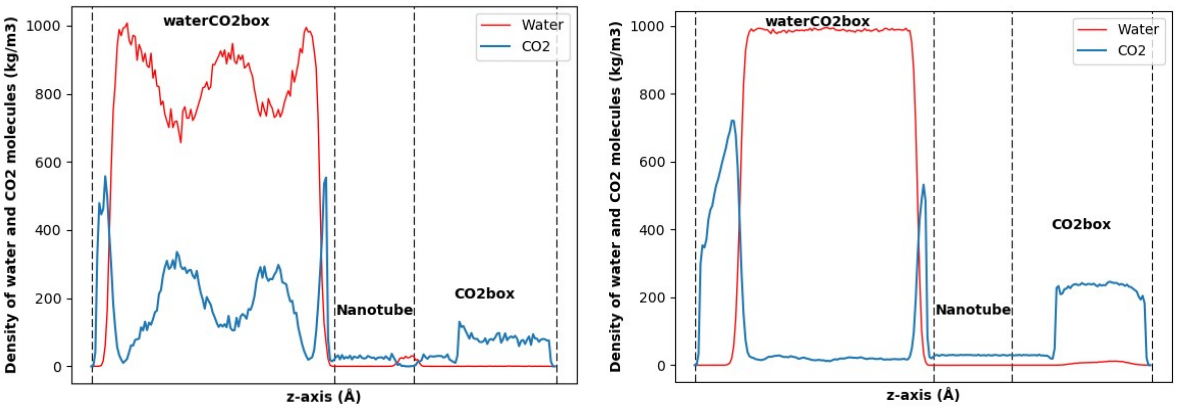

Figure 7.8: Density profile for the whole simulation system at simulation time a) 0.4 ns and b) 30 ns. The four dotted lines represent the position on the z-axis of the four graphene walls. Simulation 1 in part 1.

The second process that can explain the chemical driving force is the chemical gradient across the nanotube due to the non-equilibrium system set-up. The CO2 molecules in the water-CO2 mixture container are in a different environment than the CO2 molecules in the receiving tank. Considering the waterCO2box and the nanotube, a general expression for the net chemical work for CO2 is:

$$\left(\mu_{CO2}^{nanotube} - \mu_{CO2}^{waterCO2box}\right) dN_{CO2}^{nanotube} \tag{7.1}$$

and the same can be expressed for water:

$$\left(\mu_{water}^{nanotube} - \mu_{water}^{waterCO2box}\right) dN_{water}^{nanotube} \tag{7.2}$$

Based on the observations from the four simulations in part 1, it would be reasonable to assume that, initially, the chemical potential of CO2 in the water-CO2 mixture container is higher than the chemical potential of CO2 in nanotube, due to the strong affinity for CO2 to adsorb into the nanotube:

$$\mu_{CO2}^{CO2box} < \mu_{CO2}^{nanotube} < \mu_{CO2}^{waterCO2box} \tag{7.3}$$

For water, the opposite can be assumed, due to the strong affinity for water to stay in the water-CO2 mixture container:

$$\mu_{water}^{nanotube} \gg \mu_{water}^{waterCO2box} \tag{7.4}$$

Equations (7.3) and (7.4) are a consequence of combined first and second law of thermodynamics, which, at constant temperature and pressure, will always drive the system to minimize the chemical work-related contribution. They are based on the principle that a process (e.g. diffusion, mass transport, chemical reaction) favors in the direction from high chemical potential towards low chemical potential at constant temperature and pressure. Equations (7.3) and (7.4) describes that the chemical driving force for CO2 in the water-CO2 mixture is in the opposite direction of the chemical driving force for water in the water-CO2 mixture. The CO2 molecules have a much higher affinity to adsorb into the nanotube from the water-CO2 mixture relative to water, as seen from figure 7.1-7.4 and 7.5.

A high concentration of excess CO2 molecules in water bulk appeared to enhance the chemical driving force that results in the CO2 molecules having a much higher affinity for entering the nanotube than water, while also producing a high net flux of CO2 molecules into the receiving tank. The reason why the amounts of excess CO2 molecules are so important for the separation process can be explained by tracking the CO2 molecules passing into the nanotube. According to figure 7.9, the excess CO2 molecules from the water bulk are first enriched in the vicinity of the graphene wall, then they start traversing in the xy-plane before passing into the nanotube. This idea can be supplemented by observing the trajectory paths of individual CO2 molecules, shown in figure 7.10 for simulations 1 and 2 for the time interval from 0.4 ns to 8.0 ns. Consider two CO2 molecules in figure 7.9 a) and b), selected because they crossed over from the water-CO2 mixture container and into the receiving tank. As seen from figures 7.9 a)-b), they both were positioned in the water bulk at 0.4 ns, then they joined the enrichment of CO2 near the graphene wall at the nanotube entrance, moved in the xy-plane before passing into the receiving tank. To be precise, both molecules trajected back to the waterCO2box where they again moved along the graphene wall before once again passing through the nanotube and back into the CO2box. From both figures 7.9 and 7.10, and also the density profile in figure 7.8, it can be observed that there are almost no CO2 molecules in the region between water bulk and the CO2 enrichment layer near the right graphene wall of the waterCO2box. It appears that the CO2 molecules prefer to avoid this region in favor of concentrating near the graphene walls before adsorbing into the nanotube.

The reason for a cluster of water molecules to traject into the nanotube and to the other side was likely due to a combination of a high pressure in the water-CO2 mixture and the being “pushed” by the CO2 molecules rushing to adsorb into the nanotube.

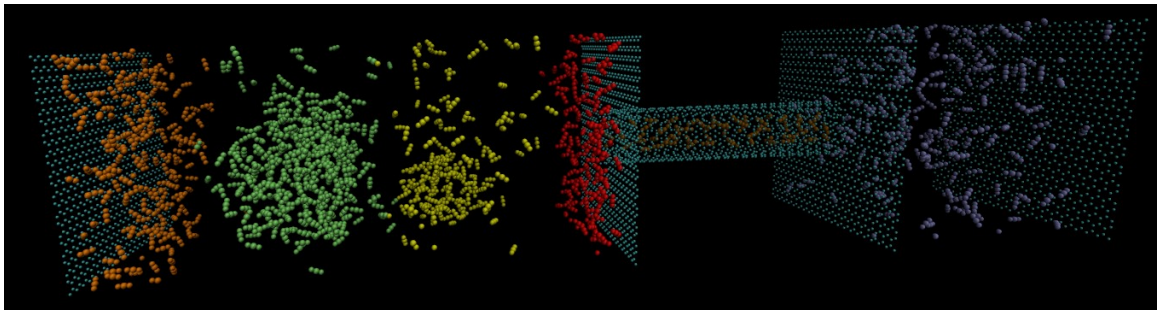

a) Simulation time 5.0 ns

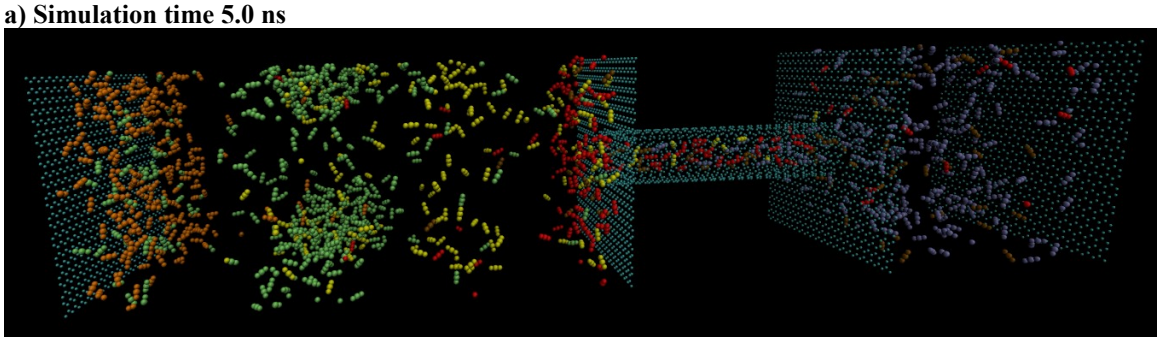

b) Simulation time 6.2 ns

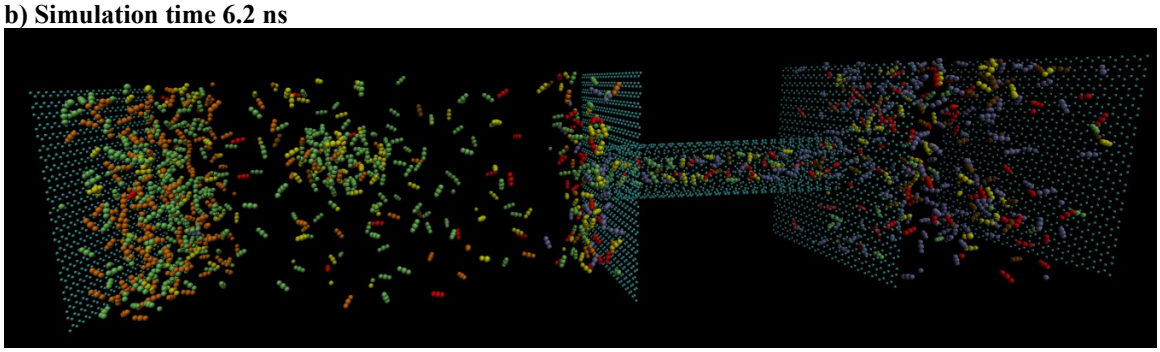

b) Simulation time 15.5 ns

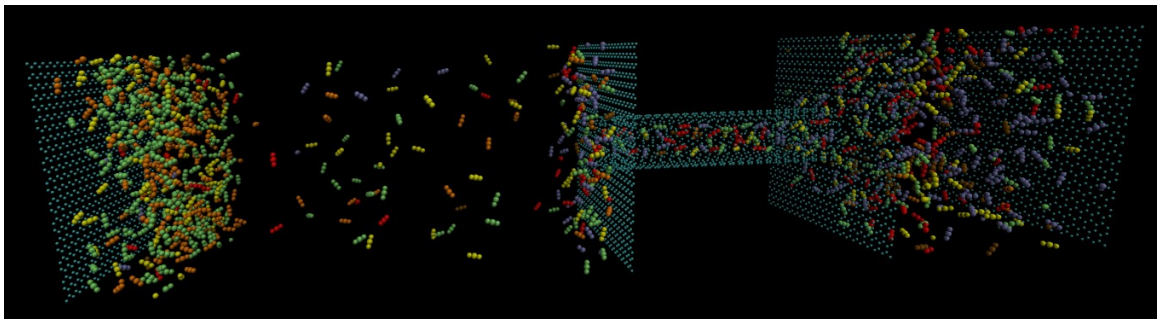

c) Simulation time 30 ns

Figure 7.9: Visual illustration of what CO2 molecules that traject into the nanotube. Simulation 1 in part 1. All the molecules (except the nanotube and the four graphene sheets) are CO2 molecules colored based on initial position, used to study molecular movements.

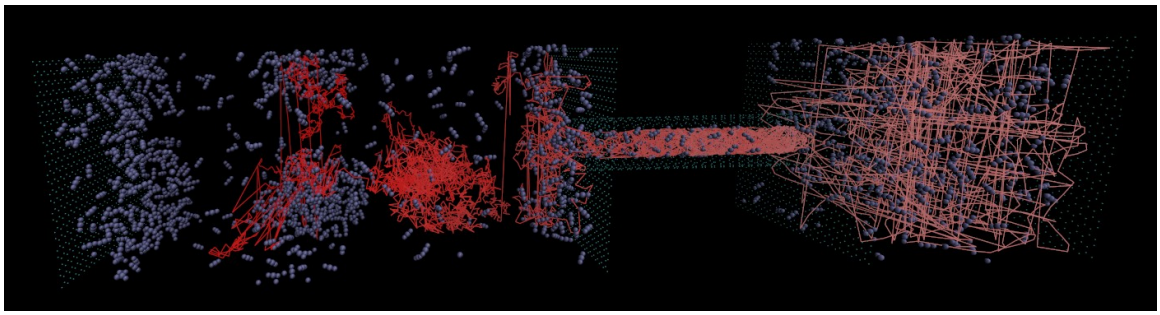

a) Trajectory path for a CO2 molecule. Simulation 1.

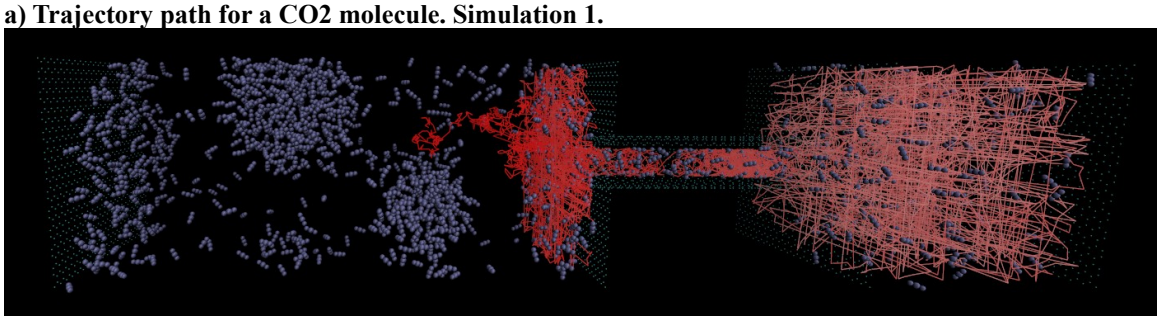

b) Trajectory path for a CO2 molecule. Simulation 1.

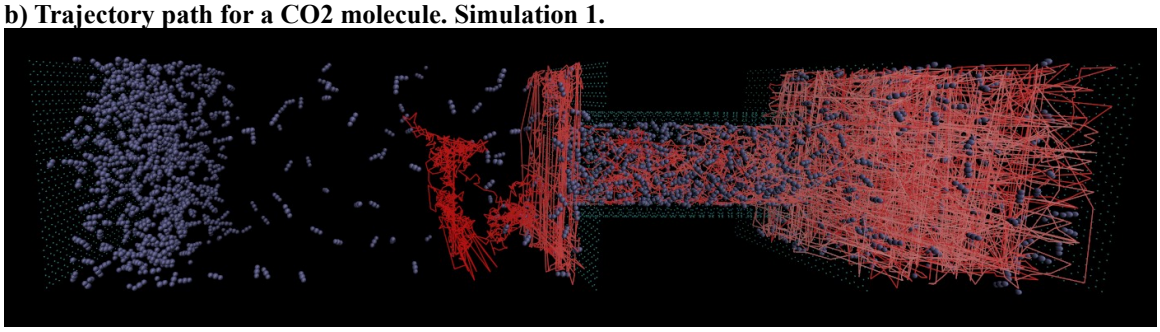

c) Trajectory path for a CO2 molecule. Simulation 2.

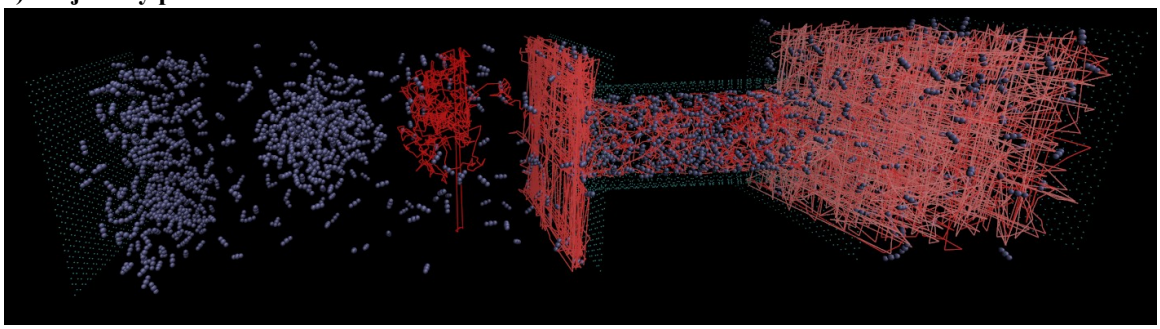

d) Trajectory path for a CO2 molecule. Simulation 2.

Figure 7.10: Visual illustration of trajectory paths (colored red) for four CO2 molecules, one trajectory path in each a)-b). Start position in water-CO2 mixture container and end position in receiving tank. Simulation time period is from 0 to 30 ns. The ice-blue colored molecules are CO2 molecules. The trajectories are calculated with a ready-to-use script in VMD [79].

7.1.3 Selectivity and risk of water entrainment

In this section, we compare the main observations for each of the four simulations to evaluate the selectivity and water risk as a function nanotube size and initial pressure gradient across it.

All the four simulations performed in part 1 exhibited good CO2 selectivity and a low risk of water entrainment. According to findings presented in figures 7.1-7.4, a higher initial pressure gradient across the nanotube corresponded to the higher flux of CO2 molecules into the receiving tank. This tendency can also be confirmed basing on the number of CO2 molecules in receiving tank vs time plotted in figure 7.5, where both red curves (higher initial pressure in the water-CO2 mixture container) are consistently higher than the corresponding orange curves (low initial pressure in the water-CO2 mixture).

The risk of water entrainment increased with pressure as well. Consider figure 7.5 a), presenting the water and CO2 flux profiles for the two (10,10) nanotube simulations. In simulation 1, a cluster of 26 water molecules entered the receiving tank, with the size of the cluster increasing to 76 in simulation 3. Both water clusters quickly traversed into the nanotube and all the way into the receiving tank, as illustrated in figure 7.1 and 7.3. When it comes to the two simulations involving a (20,20) nanotube, the water cylinder crossed over about one fourth of the nanotube length in simulation 2 and at least three fourths in simulation 4, before retreating to the water/CO2 mixture, as seen in figure 7.2 and 7.4. But still, for all the four simulations, water was highly discriminated from entering the nanotube compared to CO2, resulting in a net transport of CO2 molecules into the receiving tank. Simulation 3-4 had an initially higher pressure gradient across the nanotube relative to simulation 1-2.

However, the flux profiles in figure 7.5 do not tell the whole story about the water entrainment risk because for the two (20,20) nanotube simulations, the water cluster never reached the receiving tank, as figure 7.2 and 7.4 illustrates. According to figure 7.5, the CO2 flux into the receiving container in the two (20,20) nanotube simulations appeared to be affected more by water molecules entering the nanotube compared to the two (10,10) nanotube simulations. Simulations 3-4 exhibited a higher decrease in the number of CO2 molecules in the receiving tank initially as the simulation starts. It could be simply because the (20,20) nanotube is roughly twice larger in diameter than the (10,10) nanotube, meaning that there is a greater number of CO2 molecules initially in the receiving tank that traverse into the (20,20) nanotube. It could also be related to the risk of water entrainment. The large water cylinder entering the nanotube (before retreating) for the two (20,20) nanotube simulations are shown as a function of time in figure A.2 in Appendix A. By comparing the flux profiles of water in nanotube in figure A.2 a) and b) with the CO2 flux profiles in figure 7.5 b), it can be observed that the water cylinder in the (20,20) nanotube simulations have retreated fully in a time **after** the

number of CO2 molecules in the receiving tank began to increase rapidly. This implies that the CO2 molecules were able to pass through the nanotube even though there is a cylinder of water blocking the nanotube. After visual observation in VMD, it was found that the CO2 molecules traject both through the water cylinder and at the inner surface of the nanotube in order to pass the water cylinder. For the two (10,10) nanotube simulations, the water cluster that flows through the nanotube seems to affect the CO2 flux into receiving tank very little because the water cluster flows with the CO2 molecules through the nanotube.

The reason for the water cluster being cut off in the two (10,10) nanotube simulations, but not for the two (20,20) nanotube simulations could be due to the nanotube size. The (20,20) nanotube has a diameter of 2.708 nm while the (10,10) nanotube has a diameter of 1.354 nm. As a consequence, the water molecules that entered the larger (20,20) nanotube could maintain their hydrogen bonds with the water molecules in the water-CO2 mixture container both for a longer time and in a greater amount compared the water molecules entering the (10,10) nanotube, as seen from figure 7.6 and A.2.

Based on the simulation results, it is difficult to conclude with any certainty which nanotube size provided the best CO2 selectivity. From figure 7.5, it can be observed that the smaller (10,10) nanotube gives a higher flux of CO2 molecules into the CO2box for both initial pressure gradients relative to the larger (20,20) nanotube. An idea to a cause could be that the smaller (10,10) nanotube have a higher ability to adsorb CO2 molecules from the water-CO2 mixture due to a more confined space, leading to stronger CO2-nanotube interactions for those CO2 molecules that are inside the nanotube. Another cause could be related to the bias effect of the graphene walls. The (20,20) nanotube is larger in diameter, thus the graphene walls at the nanotube entrance have a smaller surface area, and this could cause a greater amount of CO2 molecules enrich near the nanotube entrance for the smaller (10,10) nanotube. Yet another possible cause is related to the CO2 mass limitation in the water-CO2 mixture container. The CO2 molecules that trajected from the waterCO2box and into the CO2box, they were not replaced. In addition, there was an increasing density of CO2 molecules in the CO2box. Thus, the chemical driving force decreased with time, both in terms of limitation of excess CO2 molecules in water bulk and also due to decreased chemical gradient across the nanotube. The (20,20) nanotube is likely more affected by the CO2 mass limitation than the (10,10) nanotube because it has a larger diameter and can therefore contain more CO2 molecules, resulting in a relative fewer amount of CO2 molecules than can traject all the way into the receiving tank.

Both the pressure and chemical gradient across the nanotube decreased with time. Thus, the flux curves of CO2 in receiving tank eventually flattened out. Simulation 3-4 seems to have reached a steady-state condition with a more or less flat flux curve after 30 ns simulation. But, for simulation 1-2, the flux curve seems to still be on the rise. Therefore,

to be able evaluate the steady-state conditions, all the systems must be simulated for even longer intervals. However, the steady-state conditions are not the important thing for the evaluation of the goals with part 1. Part 1 was focused on the selectivity and water risk, and as seen from the four simulations, the water molecules enter the nanotube in great amounts only in the beginning of the simulation. Once the CO2 molecules have completely filled the nanotube, no more water molecules enter the nanotube excepting the fluctuations at the nanotube entrances.

7.1.4 Comparison with previous results

The new method to capture CO2 that is presented in this master thesis is based on the hypothesis that a CO2 concentration greatly exceeding their water solubility limits (by a factor of 5-10 times) will result in a massive transport of CO2 molecules through the nanotube. The results from the four simulations conducted in part 1 appear to support this idea due to the high excess CO2 concentration in bulk water will provide a high chemical driving force in the water-CO2 mixture leading to CO2 adsorbing into the nanotube. As mentioned in section 1.3, a paper Lee & Aluru published in 2013 studied the nanotube-assisted separation of liquid water and flue gas components (CO2, N2, H2) by means of non-equilibrium molecular dynamics simulations [35]. The main difference between simulations conducted in this work and the work of Lee & Aluru is that they used the equilibrium concentrations of CO2 in water. Their system set-up was designed so that the water was saturated with CO2 based on the vapor pressure of a flue gas above the liquid water. Then, as CO2 molecules left the aqueous phase, they trajected further through the nanotube. Beside some minor fluctuations at the inlet, the study of Lee & Aluru did not observe any instance of water molecules entering the nanotube. In this master project however, as seen from figure 7.1-7.4, the water risk was significant higher, with a water cluster traversing all the way into the receiving tank (simulation 1,3) and a water cylinder entering about half of the nanotube before retreating into to the water-CO2 mixture (simulation 2,4). The higher water risk seen in the simulations conducted in this work compared to those in Lee & Aluru's results could be related to the high initial amount of excess CO2 distributed in water due to the water molecules being "pushed" into the nanotube by the CO2 molecules impelled by the strong chemical driving force. It could also be related to the mechanical driving force that will push both water and CO2 molecules into the nanotube if the pressure is high enough. Yet another possible explanation could be that Lee & Aluru used a (8,8) nanotube. As seen from our simulations, the nanotube size could make a significant impact because it was easier for the water molecules to enter the larger nanotube.

Gordillo et al. [80] has used MD simulations to show that the long-range hydrogen bond structure of water will be highly altered by the confined space in the nanotube. As

discussed earlier, the discrimination of water due to geometric limitations inhibiting optimum hydrogen bonding is one of the main contributions to the chemical driving force that ensured good CO2 selectivity through nanotube separation from water.

The flow rate of pure water through the nanotubes can be quite high [81-83], likely thanks to the the smoothness of the nanotube inner walls, narrow pore channel and weak water-nanotube interactions. This fact can actually strengthen the conclusions obtained in this project, because it shows the strong affinity for CO2 adsorption into the nanotube compared to water.

In all the four simulations performed in part 1, some water molecules immediately entered the nanotube. In case of both (10,10) nanotube simulations (simulation 1,3), the cluster of water molecules trajected all the way into the CO2box. Simulation involving the (20,20) nanotubes (simulation 2,4) had a water cluster which stayed in the nanotube before retreating into water bulk followed by CO2 completely filling the nanotube and barring any more water molecules from entering (besides some small fluctuations in/out at the nanotube entrances). This result is similar to the findings of Lee & Aluru [84] whose paper evaluated the equilibrium transport of various gas-water mixtures in carbon nanotubes. They also observed the water molecules first entering the nanotube, and then being expelled by the CO2 molecules which completely filled the nanotube. This indicates a good separation selectivity, where the CO2 molecules have a strong affinity compared to water to adsorb into the nanotube due to strong water-water interactions and strong nanotube-CO2 interactions.

The transport of pure light gases in carbon nanotubes (CNTs) have been studied extensively in the recent years. The bulk of them agree that transport diffusivities of the light gases, including CO2, in carbon nanotubes can be of orders of magnitude higher than in other nanosize channels including zeolites and polymeric pores [85-87], thus offering a huge advantage for the CO2 separation with nanotubes. The superior transport properties of CO2 in carbon nanotubes, relative to other nano-porous channels can be explained by the smoothness of the inner carbon walls and the high affinity for CO2 for adsorption into the non-polar nanotube.

7.2 Capacity of carbon nanotubes

The main goal of simulations performed as part 2 of this research project was to evaluate the capacity (flux and chemical potential) of the nanotubes. This was done by establishing the quasi-equilibrium conditions between the right-end nanotube and the receiving tank as a function of nanotube size and the initial driving forces in the water-CO2 mixture container. When the quasi-equilibrium state had been achieved, fundamental thermodynamic equations were used to estimate the chemical potential of CO2 in nanotube. The flux across the nanotube was evaluated by following the time evolution of the number of CO2 molecules in the receiving box.

To achieve the quasi-equilibrium state, simulation systems from part 1 have been modified to overcome the CO2 mass limitation in the water-CO2 mixture container and also due to challenges in controlling the driving forces of the supersaturated water-CO2 mixture. Two changes were made. First, we have changed the initial configuration of the water and CO2 molecules in the water-CO2 container. In part 2, they were packed into two layers, one layer of pure water and layer of pure CO2. The pure CO2 layer was placed near the nanotube entrance to reproduce CO2 enrichment effect in a water-CO2 mixture. Then, each system was equilibrated for 20 ns with the nanotube blocked to let the two layers stabilize. Thereafter, the four simulations were all ran for 30 ns with the nanotube open with the moveable wall moving.

Table 7.2 lists the varying parameters used in the four simulations conducted in part 2. The two nanotube sizes were chosen to represent two extreme points: a small-diameter (10,10) and a large-diameter (20,20) nanotube. The same was true in case of the independent variable corresponding to the driving forces for CO2 in the water-CO2 mixture container. The CO2 driving forces in the water-CO2 mixture container were kept constant on average by keeping the CO2 density of the CO2layer control region the same by means of the mass flow rate conservation approach. For simulations 1-2, the CO2 layer retained **liquid** density, while having **gas** density in simulations 3-4.

Table 7.2: The two independent variables for the four simulations in part 2.

Simulation nr.	Nanotube size	Density of CO2 in CO2layer control region
Simulation 1	(10,10)	Liquid
Simulation 2	(10,10)	Liquid
Simulation 3	(20,20)	Gas
Simulation 4	(20,20)	Gas

The next sub-sections contain the results and discussion pertaining to the four simulations conducted in part 2. We will first present the simulation findings obtained via visual observations. Secondly, the quasi-equilibrium state of each simulation will be considered together with the driving forces. Thirdly, the nanotube capacity will be discussed in terms of CO2 flux through nanotube and quantified further in terms of chemical potential. We will then discuss the uncertainties and errors of the simulations. Finally, the simulation results will be compared with previous work.

Once again, we will refer to the region between the two graphene walls on the left hand side of the nanotube as the water-CO2 mixture container (waterCO2box) with the receiving tank (CO2box) defined as the region between the two graphene walls on the right hand side.

7.2.1 Visual observations of the nanotube capacity simulations

Figures 7.11-7.14 present the initial and the final state of the four simulations. Both simulation 1 and 2 resulted in a tremendously high CO2 flux from the waterCO2box, through the nanotube and into the CO2box compared to simulation 3-4. The flux profiles of CO2 in the receiving tank, shown in figure 7.15, can substantiate this visual observation even further. The dramatically higher resulting number of CO2 molecules in the receiving tank evident in simulation 1-2 compared to simulation 3-4 can be attributed to the density of CO2 in the CO2layer. In figure 5.5 a) and b), the CO2 layer is defined as a region extending 20 Å in the z-direction which we used as a control volume together with a nanotube control region to move the wall based on a mass flow rate conservation equation. In simulation 1-2, that CO2layer has a liquid density of CO2. For simulation 3-4, the CO2layer has a gas density. Therefore, initially, there is a higher driving force gradient across the nanotube for simulation 1-2 compared to simulation 3-4.

The driving forces can be divided into two parts: a mechanical pressure driving force and a chemical driving force. With time, both the pressure gradient and the chemical gradient across the nanotube decreased due to the net flow of CO2 molecules into the receiving tank. The contribution from the water-CO2 mixture to the total driving forces can be assumed to be constant because we chose to maintain the density of the CO2layer. This was found to be necessary to be able to reach the quasi-equilibrium conditions as a function of nanotube size and driving forces in the water-CO2 mixture.

As seen in figures 7.15 a)-d), not a single water molecule entered the receiving tank in any of the four simulations constituting part 2.

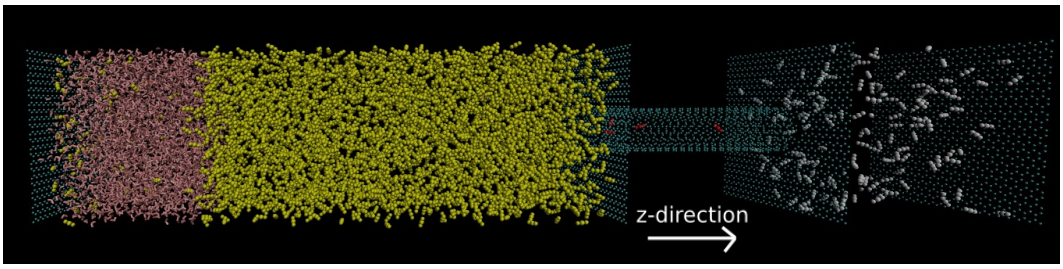

a) The initial configuration. Moveable wall at initial z-position.

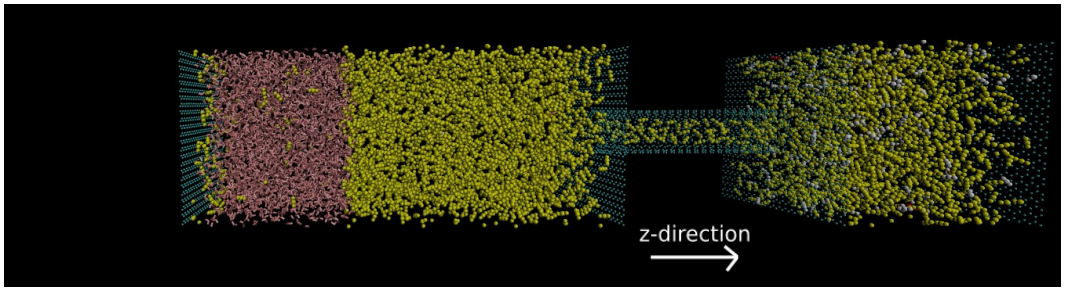

b) Snapshot of system at 30 ns. Steady-state conditions and quasi-equilibrium point are assumed to be reached. No net flow in nanotube and the moveable wall does not move much.

Figure 7.11: Visualization of initial state in a) and final state in b). Simulation 1 in part 2.

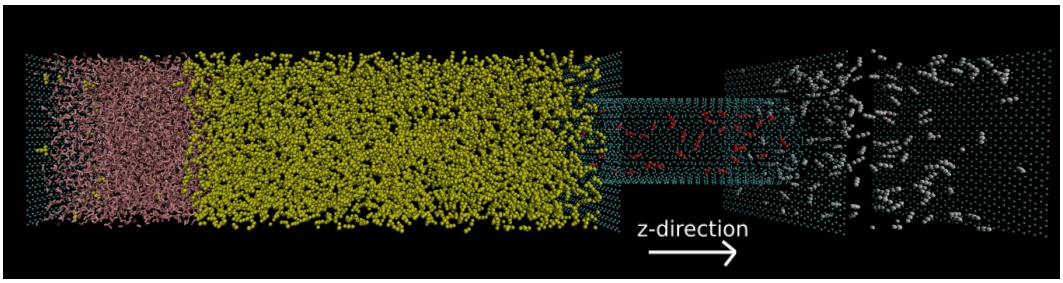

a) The initial configuration. Moveable wall at initial z-position.

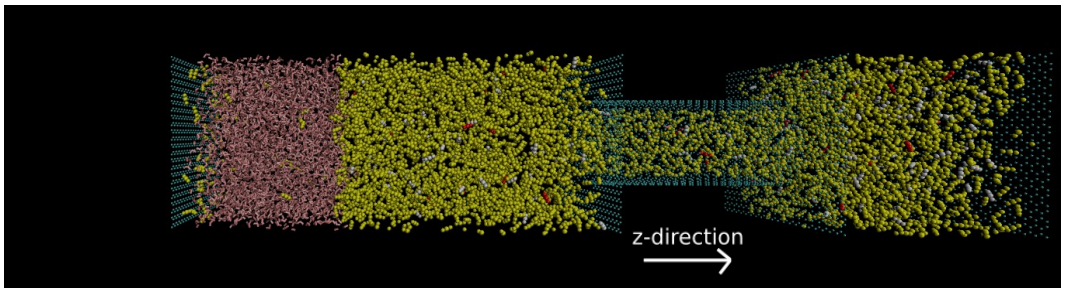

b) Snapshot of system at 10 ns. Steady-state conditions and quasi-equilibrium point are assumed to be reached. No net flow in nanotube and the moveable wall does not move much.

Figure 7.12: Visualization of initial state in a) and final state in b). Simulation 2 in part 2.

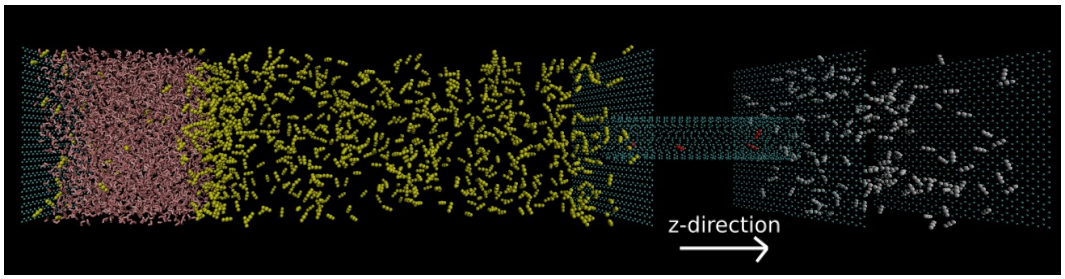

a) The initial configuration. Moveable wall at initial z-position.

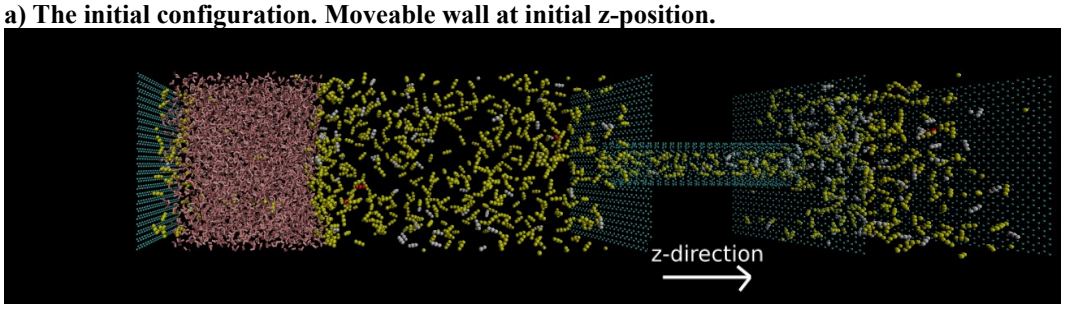

b) Snapshot of system at 30 ns. Steady-state conditions and quasi-equilibrium point is assumed to be reached. No net flow in nanotube and the moveable wall does not move much.

Figure 7.13: Visualization of initial state in a) and final state in b). Simulation 3 in part 2.

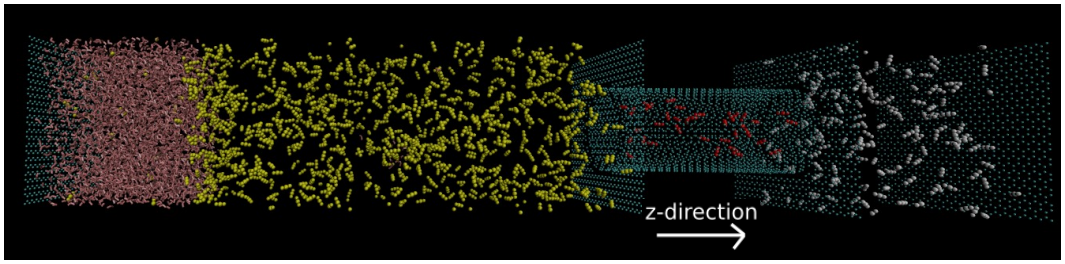

a) The initial configuration. Moveable wall at initial z-position.

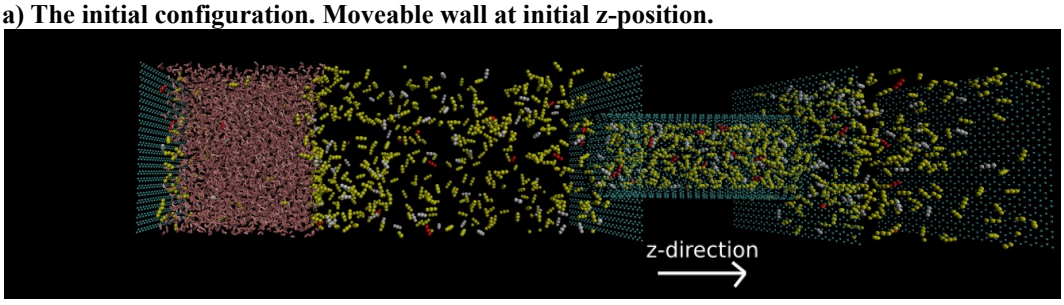

b) Snapshot of system at 30 ns. Steady-state conditions and quasi-equilibrium point is assumed to be reached. No net flow in nanotube and the moveable wall does not move much.

Figure 7.14: Visualization of initial state in a) and final state in b). Simulation 4 in part 2.

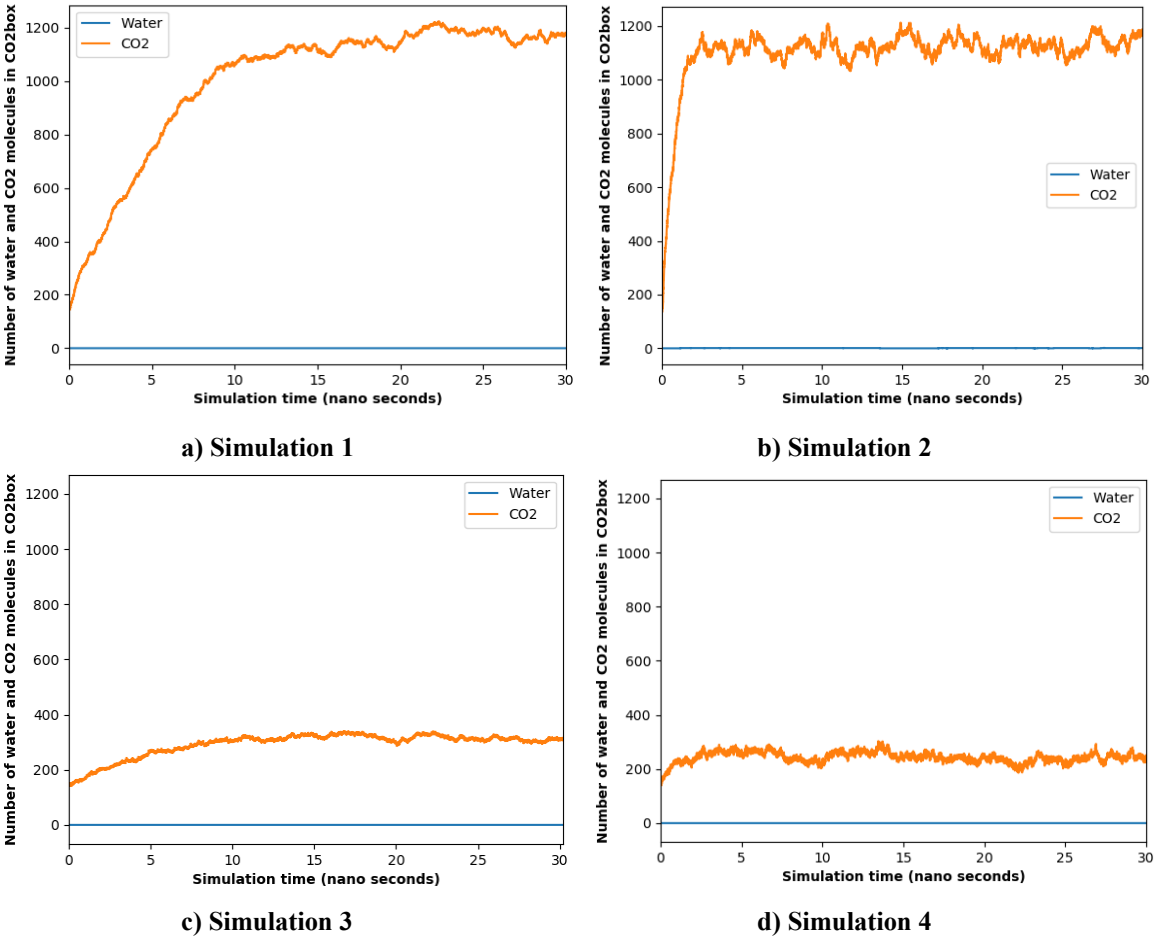

Figure 7.15: Number of water and CO2 molecules in receiving tank (CO2box) as a function of time for all the four simulations in part 2.

7.2.2 Nanotube capacity in terms of CO2 flux through nanotube

Figure 7.16 shows the number of CO2 molecules in receiving tank as a function of time for the four simulations in part 2, exactly the same as figure 7.15 a)-d). The N_{CO2} in receiving tank vs time curves vary with time due to a decrease in pressure and chemical gradient across the nanotube. All the curves increase rapidly in the beginning (approximately linearly) before they flatten out. The curvatures are different. For the two (10,10) nanotube simulations (simulation 1 and 3), the curves are more asymptotical than for the two (20,20) nanotube simulations (simulation 2 and 4), illustrating different flow properties of CO2 in the two nanotube sizes.

The number flux through nanotube can be defined as:

$$Number\ flux = \frac{1}{A_{nanotube}} \frac{dN_{CO2}}{dt} \tag{7.5}$$

where $A_{nanotube}$ is the cross-sectional area of nanotube, dN_{CO2} is the change in CO2 molecules in receiving tank and dt is the change in time.

The CO2 flux through the nanotube was estimated with a least-square linear regression fit in MATLAB. Two fluxes were estimated for each curve by using equation (7.5): a flux in the time interval where the flux is at its peak and a flux for the time interval where the flux is approximately zero. Figure 7.17-7.20 shows the estimated fluxes for the two time intervals for the four simulations in part 2. The peak fluxes are presented in table 7.2. The errors in the peak flux are calculated based on the slope of the least-square linear regression fit. The cross-sectional area of the nanotubes $A_{nanotube}$ are calculated using the gross area rather than the effective (available space) in the nanotube. The effective area is a bit smaller than the gross area due to molecular Lennard-Jones interactions. The gross diameters of the (10,10) and the (20,20) nanotube are 1.354 nm and 2.708 nm, respectively.

The fluxes calculated in this work are of course mostly suitable for relative comparison purposes. More realistic value will require calculation based on sampling of density profiles of molecules inside nanotube so as to exclude the inaccessible regions of inner tube walls to get the effective nanotube area.

From figure 7.17-7.20 and table 7.3, one can conclude (20,20) nanotubes will generate a greater peak flux through the nanotube and into the receiving tank at the same driving forces in the water-CO2 mixture container (waterCO2box) than the (10,10) nanotubes. Most likely, this is due to their ~4 times larger cross-sectional area than the (10,10) nanotube, which makes it easier for the CO2 molecules to flow through in less time.

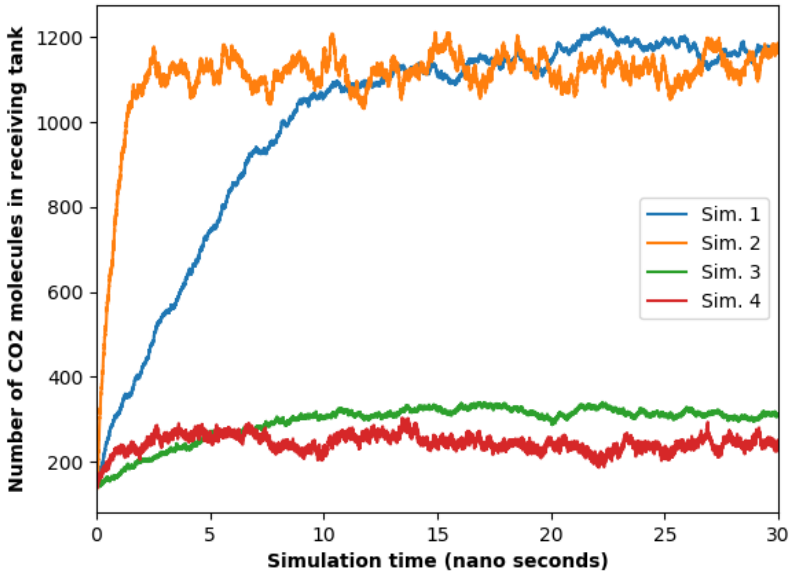

Figure 7.16: Number of CO2 molecules in receiving tank vs time for all the four simulations in part 2.

Table 7.3: Estimated CO2 flux through nanotube (direction towards receiving tank) for the four simulations in part 2, also shown in figure 7.17-7.20. The fluxes were estimated for the time interval where the flux is at its peak (colored red in figure 7.17-7.20). The two independent variables are also included: nanotube size and driving force of CO2 in water-CO2 mixture container.

Simulation nr.	Nanotube size	Driving forces in waterCO2box	CO2 flux through nanotube (molecules/ns/nm^2)
Simulation 1	(10,10)	High	4.20 +- 0.01
Simulation 2	(20,20)	High	26.4 +- 0.1
Simulation 3	(10,10)	Low	0.738 +- 0.001
Simulation 4	(20,20)	Low	1.42 +- 0.01

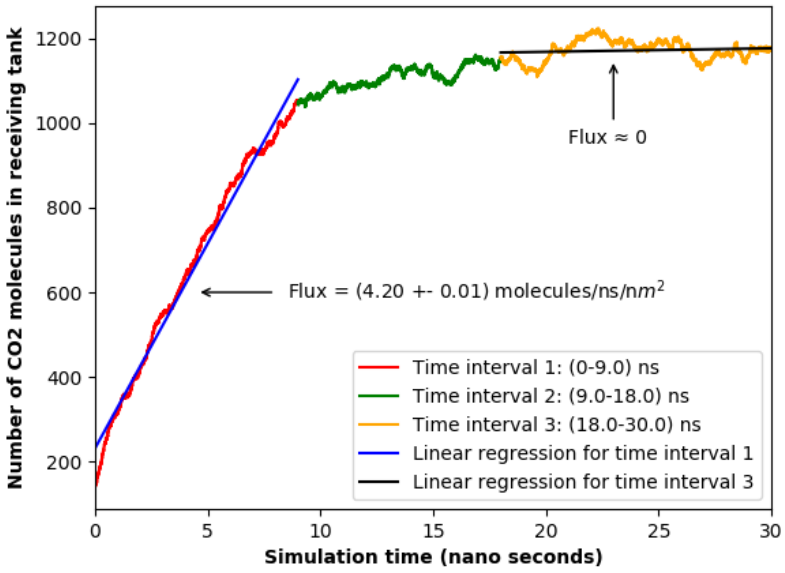

Figure 7.17: CO2 flux profile for simulation 1 in part 2, that is with the independent variables: a (10,10) nanotube and high driving forces in the water-CO2 mixture container. The flux through nanotube (direction towards receiving tank) was estimated for two time intervals: peak flux and where the flux is approximately 0.

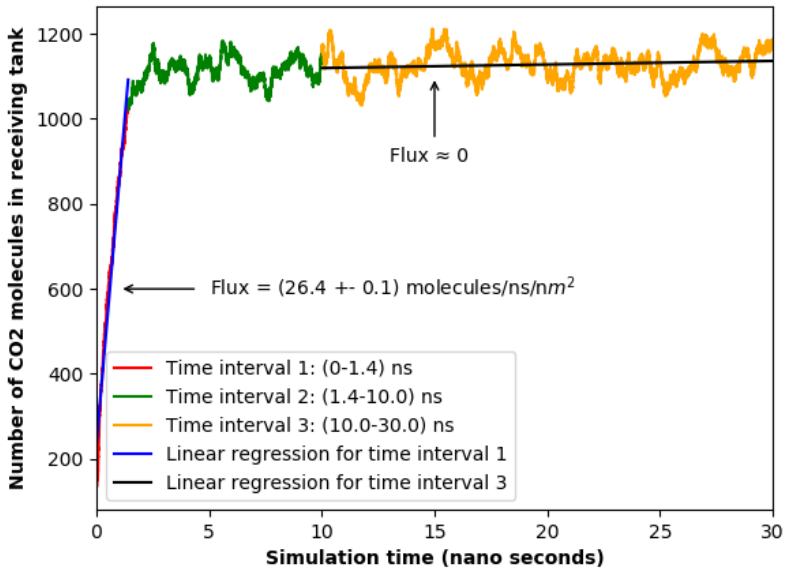

Figure 7.18: CO2 flux profile for simulation 2 in part 2, that is with the independent variables: a (20,20) nanotube and high driving forces in the water-CO2 mixture container. The flux through nanotube (direction towards receiving tank) was estimated for two time intervals: peak flux and where the flux is approximately 0.

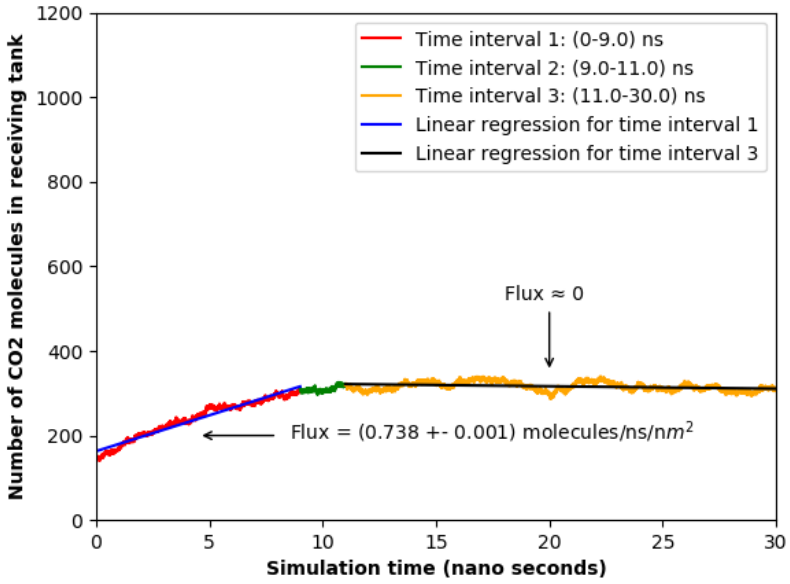

Figure 7.19: CO2 flux profile for simulation 3 in part 2, that is with the independent variables: a (10,10) nanotube and low driving forces in the water-CO2 mixture container. The flux through nanotube (direction towards receiving tank) was estimated for two time intervals: peak flux and where the flux is approximately 0.

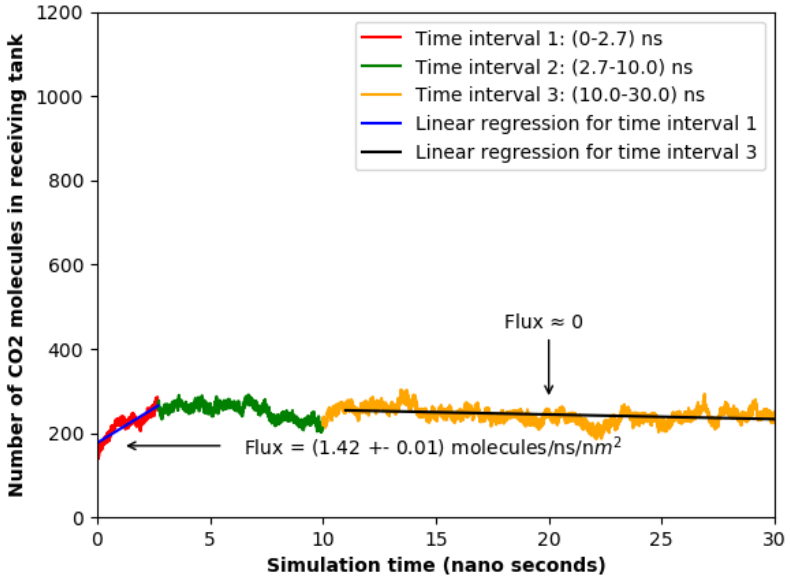

Figure 7.20: CO2 flux profile for simulation 4 in part 2, that is with the independent variables: a (20,20) nanotube and low driving forces in the water-CO2 mixture container. The flux through nanotube (direction towards receiving tank) was estimated for two time intervals: peak flux and where the flux is approximately 0.

Figure 7.16, 7.17-7.20 illustrate the substantial impact of increasing the driving forces in the water-CO2 container. Both the flux (peak flux) and amount of CO2 molecules achieved in receiving tank are much higher for simulation 1-2 compared to simulation 3-4. Simulation 1-2 have high driving forces in water-CO2 mixture container due to liquid CO2 density in the CO2layer control region while simulation 3-4 have low driving forces due to gas CO2 in the CO2layer control region. This is a very good result because it illustrates the positive effect in terms of the separation process if there is a high-density region of CO2 near the nanotube entrance in the water-CO2 mixture container.

However, determining which nanotube size that will be capable of fully saturate the receiving tank with most CO2 molecules has proven to be a challenging task. This is due to the small margin in the result. It appears in figure 7.16 that both of the (10,10) nanotube simulations actually result in a higher number of CO2 molecules in the receiving tank at quasi-equilibrium conditions than the two corresponding (20,20) nanotube simulations. But, as seen from both figure 7.16, the margin is small. In addition, the curves for the simulation 1-2 overlap due to the large fluctuations in simulation 2. The small margin may be affected by constraints with the simulation system, which will be discussed in chapter 7.2.5.

It would be instructive to consider physical phenomena behind the large fluctuations of the flux curve of simulation 2 and simulation 4 in figure 7.16. Both simulation systems contain a large (20,20) nanotube. Therefore, we suggest that the dramatic fluctuations are a consequence of the higher number of CO2 molecules present in the (20,20) nanotube than in the (10,10) once at quasi-equilibrium conditions. Hence, the fluctuation effect of CO2 molecules in/out of the receiving tank is “enhanced” for the (20,20) nanotube. The same effect has been present in the four simulations in part 1, where the content in the (20,20) nanotubes fluctuated more than that of the (10,10) nanotubes, as seen in figure 7.5.

7.2.3 Quasi-equilibrium conditions

Judging by the flux profiles in figures 7.16, 7.17-7.20, all the four simulations in part 2 had reached a good approximation of a steady-state after 30 ns simulation. The steady-state conditions are reached because the receiving tank is fully saturated with CO2 molecules at the given nanotube size and driving forces in the water-CO2 mixture tank. At steady-state conditions, there is no net flow of CO2 molecules in the nanotube (*flux* ≈ *0*). Also the pressure profiles of CO2 in receiving tank vs time will flatten out, as shown in figure B.1 in Appendix B.

To make sure that the systems have reached quasi-equilibrium conditions, all four of them were simulated for 10 ns longer with the moveable wall kept fixed to eliminate any mechanical work done on the system. We deemed this necessary, even though the wall position appeared to fluctuate around a mean value at steady-state conditions (at least in simulations 1-3, but the density of CO2 in CO2layer for simulation 4 was more challenging to control) as seen in figure B.2 in Appendix B. The resulting flux profiles from the last 10 ns of simulation with a fixed wall can be seen in figure 7.21. The flux curves are all more or less flat on average, implying quasi-equilibrium conditions. Table 7.4 lists the number of CO2 molecules in the receiving tank at quasi-equilibrium. The values were calculated with the block average method from data sampled during the last 5 ns of the 10 ns simulation with the moveable wall fixed.

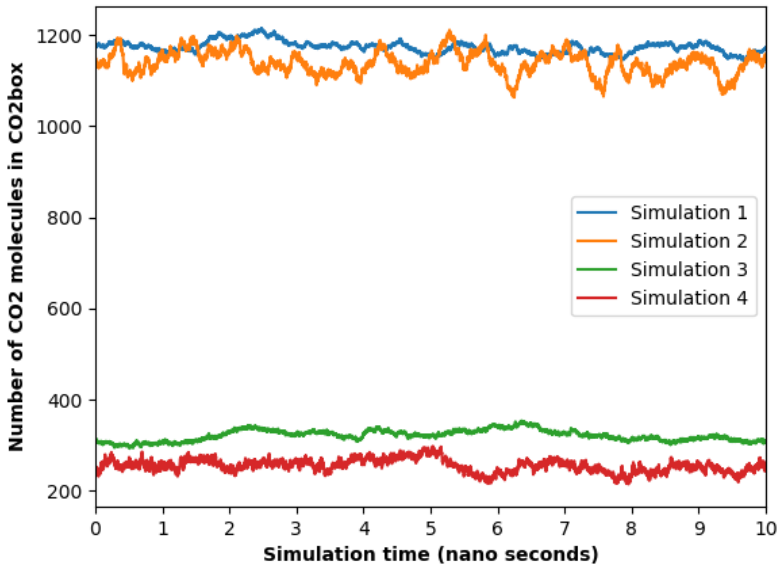

Figure 7.21: Flux profiles for CO2 in receiving tank for the 10 ns simulation with moveable wall fixed.

Table 7.4: Number of CO2 molecules in the receiving tank at quasi-equilibrium conditions with relative uncertainties.

Simulation nr.	N_{CO2} in receiving tank
Simulation 1	1177 molecules +- 1%
Simulation 2	1151 molecules +- 2%
Simulation 3	325 molecules +- 3%
Simulation 4	254 molecules +- 5%

7.2.4 Nanotube capacity in terms of chemical potential of CO2 in nanotube

The main goal of the simulation system that achieves the particular equilibrium state given the nanotube size and the driving forces was to obtain an estimate for the chemical potential of CO2 adsorbed in nanotube. At quasi-equilibrium conditions, there is no net flow of CO2 molecules in the nanotube. This implies steady-state conditions between the CO2 molecules in the water-CO2 mixture tank, the nanotube and the receiving tank.

Once the quasi-equilibrium state has been reached, it makes it possible to estimate the chemical potential of CO2 at the **right end of the nanotube** (the 30 Å right half of the nanotube). Due to the complexity in the water-CO2 mixture, it is the CO2 in the right-end nanotube and the CO2 in the receiving container that are considered to be in quasi-equilibrium. The 60 Å long nanotube is assumed to be long enough so that the CO2 in the right-end nanotube will not be affected by the water/CO2 molecules in the water-CO2 mixture container. The water-CO2 mixture tank in part 2 is very complex, just as in part 1. There are several phases including CO2 adsorbed on the graphene wall, the CO2 bulk phase, water/CO2 interfacial phase, and the aqueous phase with CO2 dissolved in water. The receiving container is much simpler. It does contain two phases, the CO2 bulk and CO2 adsorbed to graphene wall, and this might affect the chemical potential estimate. This error contribution will be discussed later.

When the quasi-equilibrium conditions between CO2 in right-end nanotube and CO2 in the receiving container (CO2box) have been established, the total Gibbs free energy can be assumed to be minimized:

$$dG^{tot} = dG^{1} + dG^{2} = 0 \tag{7.6}$$

where *2* represents the “right-end nanotube” and *3* represents the “CO2box”. By applying equation (4.10)-(4.11) to both regions, the change in Gibbs free energy for CO2 in the right-end nanotube can be expressed as:

$$dG^1 = V^1 dP^1 - S^1 dT^2 + \Sigma \mu_i^1 dN_i^1 \tag{7.7}$$

The same for the change in Gibbs free energy in the receiving container:

$$dG^2 = V^2 dP^2 - S^2 dT^1 + \Sigma \mu_i^2 dN_i^2 \tag{7.8}$$

The physical meaning of dP^2 is an infinitesimal change in pressure of the CO2 in the receiving container as time increases from t_0 to t_1. Similar description could be made for dT^2, dP^1 and dT^1. At quasi-equilibrium conditions, $dP^2 \approx 0$ and $dP^1 \approx 0$ because no mechanical work is done on/by the system and there is no net flow in the nanotube. In addition, at quasi-equilibrium conditions, $dT^2 = 0$ and $dT^1 = 0$ due to the Berendsen thermostats applied to both the receiving tank and the water-CO2 mixture container. The thermostats can be thought of as a mechanist that couple each containers to an external heat bath so that heat can be exchanged in order to keep the temperature at 298 K. The simulation system is assumed be isolated from the rest of the universe, meaning that the number of molecules in the system is constant. And, at quasi-equilibrium conditions, the exchange of CO2 molecules between the right-end nanotube and the receiving box is assumed to be the same, hence, $dN^1 = -dN^2$. Therefore, at quasi-equilibrium conditions, by combining equation (7.6)-(7.8) with the conservation laws for an isolated system, and the thermal and mechanical quasi-equilibrium conditions, the total change in Gibbs free energy can be written as:

$$dG^1 + dG^2 = (\mu_{CO2}^1 - \mu_{CO2}^2) dN_{CO2}^2 \tag{7.9}$$

In equation (7.9), the water term for chemical work is not included because no water molecules entered the receiving tank for none of the four simulations in part 2.

Equation (7.9) implies that for the total Gibbs free energy to be minimized (reach 0), there exist three criteria for quasi-equilibrium conditions:

$$T^1 \approx T^2 \qquad \textit{Thermal quasi-equilibrium} \tag{7.10}$$

$$P^1 \approx P^2 \qquad \textit{Mechanical quasi-equilibrium} \tag{7.11}$$

$$\mu_{CO2}^1 \approx \mu_{CO2}^2 \qquad \textit{Chemical quasi-equilibrium} \tag{7.12}$$

The whole process presented and described so far in chapter 7.2 proposes a new technique used to estimate the chemical potential of CO2 at the right end of the nanotube by means of equation (7.12). The chemical potential of CO2 in receiving tank will be estimated, and as equation (7.10)-(7.12) express, the chemical potential of CO2 in right-end nanotube is assumed to be the same as the chemical potential of CO2 in receiving tank at quasi-equilibria. Calculating the chemical potential of CO2 in nanotube directly would make no sense due to such the confined space in the nanotube, which makes the

behavior of CO2 in nanotube highly affected by all the bouncing into the inner nanotube walls.

The chemical potential of CO2 in receiving tank (CO2box) μ_{CO2}^{2} in equation (7.12) is the **total** chemical potential of CO2 in receiving tank. The total chemical potential is the sum of the residual and the ideal:

$$\mu_{CO2}^{total,2} = \mu_{CO2}^{residual,2} + \mu_{CO2}^{id.gas,2} \tag{7.13}$$

where $\mu_{CO2}^{total,2}$, $\mu_{CO2}^{residual,2}$, $\mu_{CO2}^{id.gas,2}$ are the total, residual and ideal gas chemical potential of CO2 in the receiving tank, respectively. $\mu_{CO2}^{total,2}$ is the same as μ_{CO2}^{2} in equation (7.12).

So, in order to calculate the total chemical potential of CO2 in the right-end nanotube, the residual and ideal gas chemical potential of CO2 in receiving tank must be calculated.

The **residual** chemical potential of CO2 in receiving tank was estimated using the technique of thermodynamic integration. For each of the four systems in part 2, a box that is identical to the CO2box (but without the graphene walls) was simulated in the NVT ensemble, i.e. a pure box of CO2 molecules with periodic boundary conditions in all three directions mimicking bulk CO2 phase. The volume of the box is the same as the CO2box volume in the four systems, *(51.577x51.048x52.0) Å*^{3}. The number of CO2 molecules used in the thermodynamic integration was the same as that in the CO2box on average at the quasi-equilibrium conditions, from table 7.4. In total, ten NVT simulations for the pure CO2box were conducted, each different thermostat temperature, starting from 298K and all the way up to 2980 K, with equal spacing for 1/T. The pair potential energy per CO2 molecule was evaluated in each simulation. The pair potential energy per CO2 molecule (kJ/mole) was then plotted as a function of 1/T (1/T). The curve for all the four simulations in part 2 are shown in figure 7.22. The theoretical point (0,0) represents the ideal gas. For an ideal gas, both the inverse temperature and potential energy are zero.

A cubic polynomial fit was made to interpolate between the data points from the 10 simulations + the theoretical point in figure 7.22. The interpolation was done by using the MATLAB function *Piecewise Cubic Hermite Interpolating Polynomial* (PCHIP). Then, the MATLAB function *Trapezoidal Numerical Integration* (Trapz) was used to integrate the polynomial function from 1/298 (1/K) to infinity inverse temperature (1/K). This resulted in a value *Q* of the integral. Then, the residual chemical potential of CO2 in the CO2box $\mu_{CO2}^{residual,2}$ was calculated by using equation 4.23, modified as:

$$\mu_{CO2}^{residual,2} = 298\,x\,Q \tag{7.14}$$

In figure 7.22, it can be observed that the potential energy at 1/298 (1/K) is significantly lower for simulation 1-2 compared to simulation 3-4. This is related to the density. For simulation 1, 1177 CO2 molecules were used in the simulation of pure CO2 box without graphene walls, which implies a density of 680 kg/m3. For simulation 2, the number of CO2 molecules used was 1151 with a density of 665 kg/m3. Both densities are close to reaching the liquid density of CO2, as seen from figure 5.8, where the dew point density at 298 K is 712 kg/m3. For simulation 3 the N_{CO2} was 325 with 188 kg/m3 in density, and for simulation the N_{CO2} was 254 with 147 in density. For simulation 3 and 4, at those two densities, the CO2 is in gas phase. It makes sense that the potential energy at 298 K for "almost liquid density" is significant lower than for CO2 gas density because a gas contains more energy. As an example, heat energy can be added to liquid water to make it boil (change from liquid to gas phase). Therefore, the relative potential energies in the thermodynamic integration make physical sense.

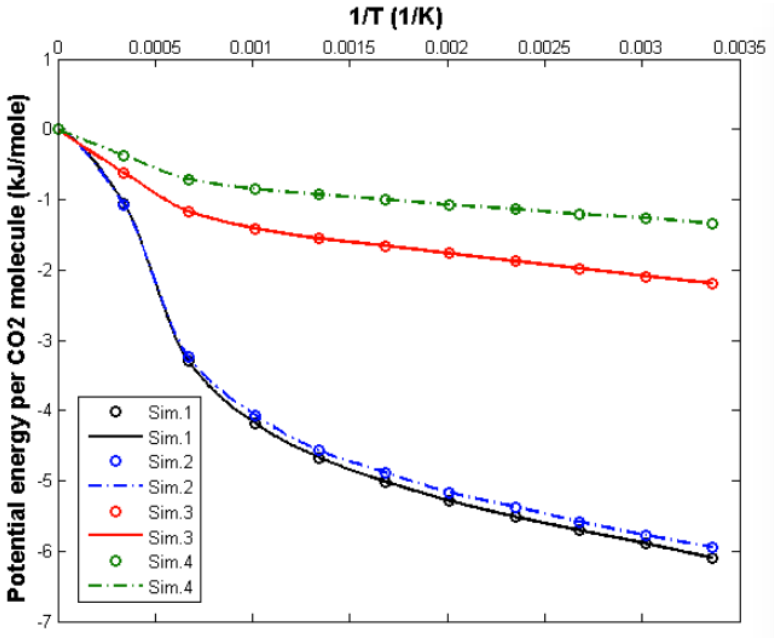

Figure 7.22: Potential pair energy per CO2 molecule (kJ/mole) vs 1/T (1/K), for simulation 1-4 in part 2. Circles represent simulation data points. Lines represent polynomial interpolation fit. The plot is used to estimate the residual chemical potential of CO2 in receiving tank.

The **ideal** gas chemical potential for CO2 in receiving tank was calculated analytically by coding a script in Fortran 95 that uses temperature and density as input variables. The script is included in Appendix C. In addition, the moments of inertia for the CO2 molecule are part of the ideal gas chemical potential calculation.

To make the ideal gas chemical potential as representable as possible for the CO2 model used in this project (Harris & Yung EPM2 semiflexible CO2 model), the moments of inertia for this CO2 model were calculated. The moments of intertia of a molecule is defined as the resistance the molecule has to rotate when exerted by a torque force, and they describe the rotational degrees of freedom for the CO2 molecule. There are three principal moments of inertia that define the moments of inertia of a molecule. That is: *Ixx*, *Iyy* and *Izz*, one contribution each of the three Cartesian coordinate axes. The moments of inertia can be calculated by applying basic geometry linear algebra to the molecule. For example, the length of the C_{CO2}-O_{CO2} bonds in the CO2 molecule is known, the same is the average O_{CO2}-C_{CO2}-O_{CO2} angle. By simulation of a box of 146 CO2 molecules, with box volume of (51.577x51.048x52.0) $Å^3$, at 298K, for 10 ns, it was found that the average angle for the EPM2 semiflexible CO2 model molecule used in this project is (178.9 +- 0.7) degrees. Luckily, VMD have a build-in function that makes it possible to measure the moments of inertia for the CO2 molecule from a simulation. The build-in function *measure moments $sel eigenvals* was used to calculate the average moments of inertia of the EPM2 semiflexible CO2 model molecule from the simulation described above. The result is shown in table 7.5.

Table 7.5: Moments of inertia in xyz directions for EPM2 semiflexible CO2 model (with angle 178.9 degrees on average). Found by simulation.

EPM2 semiflexible model		
I_{xx} (g/mole $Å^2$)	I_{yy} (g/mole $Å^2$)	I_{zz} (g/mole $Å^2$)
42.238 +- 0.006	42.236 +- 0.007	0.002 +- 0.008

For a rigid, linear CO2 molecule (with 180 degrees angle), there exists just two rotational degrees of freedom. It implies that $I_{xx}=I_{yy}$ and $I_{zz}=0$. EPM2 CO2 model is semiflexible, meaning that the angles can oscillate from the equilibrium angle 180 degrees, giving a third rotational degree of freedom. Thus, the I_{zz} is not 0 and also the value of I_{xx} and I_{yy} will be affected, as seen in table 7.5. But, there were some challenges with measuring a representable potential energy contribution from the angle bending as part of the thermodynamic integration (this will be discussed more comprehensively later on). Therefore, it was chosen to use the moments of inertia for a linear CO2 molecule (in table 7.6) instead of the moments of inertia for the angle-bending EPM2 semiflexible CO2 model (in table 7.5).

The moments of inertia for a linear, rigid CO2 molecule with the same bond length as the EPM2 semiflexible CO2 model was calculated and are listed in table 7.6. Equation (7.15) was used in the calculation:

$$Ixx = Iyy = 2\, m_O\, r_{C-O}^2 \quad , \quad I_{zz} = 0 \tag{7.15}$$

where m_O is the mass of the oxygen atom and $r_{C\text{-}O}$ is the bond length between the carbon atom and the oxygen atom in the CO2 molecule. For the EPM2 semiflexible CO2 model, the bond length is 1.149 Å.

Table 7.6: Calculated moments of inertia in xyz directions for linear CO2 molecule.

Linear CO2 molecule	
$I_{xx}=I_{yy}$ (g/mole Å^2)	I_{zz} (g/mole Å^2)
42.253	0

The estimated **total** chemical potential values of CO2 in receiving tank are listed in table 7.7. At quasi-equilibrium conditions, the total chemical potential of CO2 in the right-end nanotube is assumed to be the same as the total chemical potential of CO2 in the receiving tank, according to equation (7.12). The residual and ideal gas chemical potentials of CO2 in receiving tank are also listed in table 7.7.

The estimated residual chemical potentials follow the same tendency as the measured potential pair energies in figure 7.22. The residual chemical potentials for simulations 1-2 are an order of magnitude lower than that for simulations 3-4.

The total chemical potential of CO2 in nanotube can be used to characterize the adsorption capacity of the nanotube under given system conditions. The adsorption capacity is a vital characteristic for an adsorption material and is of primary importance. In the discussion of estimated chemical potential of CO2 in nanotube in terms of nanotube capacity, the total chemical potential will be used because it contains both the potential energy contribution and the kinetic energy contribution. In table 7.7, it can be observed that the total chemical potential values are approximately the same in all four simulations. This result can be explained by considering the liquid/vapor equilibrium. Theoretically, at liquid/gas equilibrium, the total chemical potential for each phase should be identical, according to the quasi-equilibrium criteria in equation (4.20)-(4.22). The same must hold for temperature and pressure. Thus, the similarity of total chemical potentials makes sense because the densities for achieved CO2 in the receiving tank for simulations 1-2 and simulations 3-4 are each close to the liquid/vapor equilibrium curve at 298 K, according to figure 5.8. The residual chemical potential on the other hand will be lower for the liquid phase due to the lower potential energies, same as observed for the measured pair potential energies in figure 7.22. In order for the total chemical potentials to be about the same for all densities, then the ideal gas chemical potentials have to

balance the residual chemical potentials. Hence, it makes sense that the ideal gas chemical potential for liquid phase (simulation 1-2) is higher than that for gas phase (simulation 3-4).

The total chemical potentials listed in table 7.7 constitute the "final result" of this project, meaning that estimating the chemical potential of CO2 was the one of the main goals with this master thesis. In part 1, the selectivity and water risk were evaluated, and as discussed, it is the chemical work (chemical driving force) that makes the CO2 molecules selectively adsorb into the nanotube from the non-equilibrium water-CO2 mixture. The chemical work is related to the difference in total chemical potentials:

$$\left(\mu_{CO2}^{nanotube} - \mu_{CO2}^{waterCO2box}\right) dN_{CO2} \tag{7.16}$$

The total chemical potential of CO2 in nanotube $\mu_{CO2}^{nanotube}$ can also be related to the minimum work required to add one more CO2 molecule into the nanotube. This can best be illustrated with an example. Consider simulation 1, where the total chemical potential of CO2 in right-end nanotube at quasi-equilibrium conditions was estimated to be -40.281 +- 0.008 kJ/mole. Most likely, in a separation process, the chemical potential of CO2 in a non-equilibrium water-CO2 mixture will vary dependent on what phase the CO2 molecules are in. For instance, the CO2 can be distributed as nanobubbles or be more spread. Consider a CO2 nanobubble in a non-equilibrium water-CO2 mixture. If the chemical potential the CO2 nanobubble in the water-CO2 mixture container is higher than the chemical potential of CO2 in nanotube (-40.281 kJ/mole in right-end nanotube), then CO2 molecules favors for trajecting into the nanotube:

$$\mu_{CO2}^{waterCO2box} > \mu_{CO2}^{nanotube} \tag{7.17}$$

This is because a positive dN_{CO2} change in nanotube will result in a decrease in free energy and is as such favorable.

With time, the total chemical potential of the CO2 in the water/CO2 mixture will likely decrease (and so does the chemical work). The mass transport of CO2 molecules into the nanotube will stop when the total chemical potential of CO2 in nanobubble decreases so much that it eventually limits the magnitude of the chemical potential of CO2 in nanotube. Therefore, the total chemical potential of CO2 in nanotube describes the minimum chemical work required to add one more CO2 molecule into the nanotube. This example illustrates the high importance of knowing the total chemical potential of CO2 in nanotube because the chemical potential is a very important factor that determines both the water/CO2 selectivity and the amount of CO2 molecules that can be adsorbed into the nanotube (nanotube capacity).

Similar to the total chemical potentials in table 7.7, the density of CO2 in right-end nanotube (the 30 Å right half of the nanotube), listed in table 7.8, does not differ much for the four simulations, even though there is a difference in nanotube size and density of CO2 in receiving tank (from gas to "almost" liquid density). This result implies that there is a certain limit of the magnitude of both density and total chemical of CO2 in nanotube. This result is a good thing in terms of the use of nanotubes in separation process of water and CO2 because it illustrates that the behavior of CO2 in nanotube (in terms of density and total chemical potential) is not so affected by external factors like nanotube size and driving forces in the connecting containers.

Table 7.7: Total, residual and ideal gas chemical potential of CO2 in the right-end nanotube estimated for all the four simulations in part 2 at quasi-equilibrium conditions. With corresponding densities of CO2 in the receiving tank. 298K temperature.

Simulation nr.	CO2 density in receiving tank (kg/m^3)	Resid. chemical potential (kJ/mole)	Id.gas chemical potential (kJ/mole)	Tot. chemical potential (kJ/mole)
Simulation 1	680 +- 1%	-4.375 +- 0.008	-35.905	-40.281 +- 0.008
Simulation 2	665 +- 2%	-4.279 +- 0.008	-35.961	-40.240 +- 0.008
Simulation 3	188 +- 2%	-1.528 +- 0.009	-39.091	-40.620 +- 0.009
Simulation 4	147 +- 3%	-0.925 +- 0.002	-39.700	-40.625 +- 0.002

Table 7.8: Number of CO2 molecules and gross CO2 density in the right-end nanotube at quasi-equilibrium conditions.

Simulation nr.	CO2 density in receiving tank (kg/m^3)	Number of CO2 molecules in nanotube	CO2 density in nanotube (kg/m^3)
Simulation 1	680 +- 1%	32 +- 2%	67.7 +- 2%
Simulation 2	665 +- 2%	165 +- 3%	87.2 +- 3%
Simulation 3	188 +- 2%	29 +- 2%	61.3 +- 2%
Simulation 4	147 +- 3%	112 +- 4%	59.2 +- 4%

The densities of CO2 in the right end nanotube, listed in table 7.8, were calculated by first counting the number of CO2 molecules present in the right-end nanotube at quasi-equilibrium conditions, and then convert it to kg/m^3. The density is calculated with the gross nanotube volume, which is the volume of whole nanotube (in contrast to the effective, net available pore volume for the CO2 molecules due to molecular Lennard-Jones interactions).

7.2.5 Uncertainties and constraints for simulation systems in part 2

For the estimated residual chemical potential of CO2 in nanotube, listed in table 7.7, there are two types of errors. The **first type of error** is related to the thermodynamic integration. The residual chemical potentials in table 7.7 are listed with their corresponding absolute uncertainties. The uncertainties are calculated based on the mean relative uncertainty for the measured potential pair energies from the NVT simulation of box with pure CO2 molecules. This is thought to be reasonable because they are in the same order of magnitude for a temperature of 298K. In table B.1 and B.2 in Appendix B, the measured temperature and potential pair energies are listed with uncertainties, for simulation 1 and 4 (as two extreme scenarios). 10 simulations were conducted for both simulation 1 and 4, but just 4 are listed for simplicity. The information the two tables provide is that the mean measured temperature is the same as the thermostat temperature within the uncertainty, which is a very good thing. Therefore, the residual chemical potentials are listed with the same percentage error as the relative error in the potential pair energy, with the same number of significant digits as the absolute uncertainty in the potential pair energy measurements. It was found necessary to include representable errors for the residual chemical potentials to be able to evaluate how many significant digits present them with. The error bars in the simulation data points in the plot of potential pair energy per CO2 molecule vs 1/T in figure 7.22 are not included because they are very minor. For all the simulation data points, the error bars in both x -and y-direction are within the circles. Therefore, if they were to be included, they would have just made things more unorganized and chaotic and disturb the purpose of the plot.

In addition, there is a minor error in the PCHIP method and the Trapz method in MATLAB used to calculate the residual chemical potential from the data points in figure 7.22. They are not included quantitatively, but just discussed qualitatively. PCHIP is a interpolation method, thus is strikes exactly through the data points, but the curvature between the points could result in errors. An advantage with the PCHIP interpolation method, compared to e.g. the *spline interpolation function* in MATLAB, is that the PCHIP is designed so that there is as little unnecessary curvature between the data points. Actually, the Trapz method could have been used to estimate the residual chemical potential directly from the data points. As an example, for simulation 1, using the PCHIP method together with the Trapz method, the result was $\mu_{CO2}^{residual,2} = -4.375$ kJ/mole. Using the Trapz method directly on the data points gave $\mu_{CO2}^{residual,2} = -4.374$ kJ/mole.

Hence, not much difference even though they use different approached. The Trapz method stretches a linear line between each data points, while the method using Trapz combined with PCHIP uses many more points between the data points.

During the simulations of the box of pure CO2 molecules without graphene walls (as part of the thermodynamic integration), a challenge occurred. Above ~400 K, the potential energy was measured to be positive. Related to the curves in figure 7.22, that is not possible because the theoretical point is (0,0). After investigation, it was found that the angle bending potential energy contributed with a too large potential energy to the total measured potential energy. To get a more representable potential energy per CO2 molecule, the angle bending potential energy was neglected and just the pair potential energy was measured. As discussed in Chapter 3 about the bonded and non-bonded interactions between atoms/molecules, the total potential energy interaction for the EPM2 CO2 model can be expressed as:

$$U_{total} = U_{non-bonded} + U_{bonded} \tag{7.18}$$

$$U_{non-bonded} = U_{vdw} + U_{electrostatic} \tag{7.19}$$

$$U_{bonded} = U_{bond\,stretching} + U_{angle\,bending} \tag{7.20}$$

The EPM2 CO2 molecule is semiflexible, meaning that the bonds are rigid, thus no bond stretching and the potential energy contributions from the bonds are zero. This was measured correctly in LAMMPS, but the measured potential energy contribution from the angle bending was too large. Consequently, only the pair potential energy was used in the thermodynamic integration and chemical potential estimation, as seen in figure 7.22. The pair potential energy is exactly the same as the non-bonded potential energy $U_{non-bonded} = U_{vdw} + U_{electrostatic}$. The choice to just use pair potential energy can be thought to be reasonable because it may be that the EPM2 semiflexible model is not fitted to reproduce perfect angle potential energy. The interaction parameters for the EPM2 model are known to produce good equilibrium data for CO2 up to the critical point, but no simulation model is perfect at everything. The reason why sampled angle bending potential energy is too large is not clear and investigations of reasons would be far beyond this project. The mean angle of CO2 molecules was measured to be (178.5 +- 0.8) as previously mentioned, so things seem to be ok with the angles. The challenge with angle bending potential energy is the reason why the moments of inertia for the theoretical linear CO2 molecule was used in the calculation of ideal chemical potential and not the values calculated from simulation.

Yet another uncertainty related to the thermodynamic integration is the bias effect the graphene walls have on the estimated residual chemical potential. The receiving tank (CO2box) in the four simulation systems in part 2 all have two graphene walls, as seen

from figure 7.11-7.14. In the thermodynamic integration process to estimate the residual chemical potential, the two graphene walls were not included. The thermodynamic integration was conducted for just a pure box of CO2 molecules, and therefore there is infinity bulk CO2 over all xyz periodic boundaries. Hence, the estimated residual chemical potential does not include the graphene-CO2 interactions which are present in all the four main simulations in part 2. The bias effect the graphene walls have on the estimation can be quantified in terms of the Gibbs free energy contribution of the graphene walls:

$$dG^{fluid-wall} = x_{CO2}\,\mu_{CO2-wall} + x_{water}\,\mu_{water-wall} \tag{7.21}$$

where x_{CO2} and $\mu_{CO2\text{-}wall}$ are the mole fraction and chemical potential of CO2 in the CO2 phase adsorbed to the wall, and x_{water} and $\mu_{water\text{-}wall}$ are the mole fraction and chemical potential of water in the water phase adsorbed to the wall.

With the graphene walls present, there are at least two phases of CO2 based on interactions. The first is the CO2 bulk phase and the second is the CO2 adsorbed to graphene wall phase (even though the graphene-CO2 interactions are 1/10 scaled down). By using equation (7.21), the bias effect could have been quantified by conducting two simulations. The first one is the simulation conducted in this project. That is with a pure box of CO2 molecules without graphene walls where the CO2-CO2 pair potential energy is measured. The second one is a simulation with two graphene walls, representing the receiving tank in the four main simulation systems in part 2, where both the CO2-graphene and CO2-CO2 potential pair energies are measured. However, in this master project, graphene wall bias effect is not evaluated quantitatively, but just being discussed qualitatively. This is done simply because of prioritization and the time limit.

The ideal gas chemical potential is calculated analytical, thus there are really no errors other than round-off and truncation errors.

The **second type of error** is related to the constraints of the simulation systems. In this project, there have been some challenges in controlling the driving forces of the simulation systems. The challenges occurred in the very beginning of this research project. It started all the way back with the simulations conducted in part 1, where the heterogeneous, non-equilibrium water-CO2 mixture made it very difficult to control the driving forces. A result from part 1 was the CO2 mass limitation in the water-CO2 mixture that resulted in steady-state conditions before the desired quasi-equilibrium conditions were reached. The desired quasi-equilibrium condition is a situation where there is enough CO2 molecules available in the water-CO2 mixture and still the receiving tank is fully saturated with CO2 molecules, which in this work have been investigated as a function of nanotube size and initial driving forces. Therefore, the simulation system in part 1 was modified. The result of the modification, after a very time consuming working

period, was the simulation system shown in figure 5.5 and 7.11-7.14. The system in part 2 is designed to have enough CO2 molecules in the water-CO2 mixture and still preserve the water/CO2 interface. In addition, the layer of CO2 molecules made it possible to control the driving forces. To use the word “control” is maybe a little exaggeration because most likely the driving forces are not controlled due to the complexity of the water-CO2 mixture container. Anyway, the driving forces was assumed to be controlled by controlling the density of CO2 in the CO2layer, a 20 Å z-long layer of CO2 molecules 10 Å away from the nanotube entrance in the water-CO2 mixture container. The density was chosen to control the driving forces because there can be assumed to be two yielding driving forces present. That is: the mechanical pressure driving force and the chemical driving force. This is an reasonable assumption because both pressure and chemical potential are a function of temperature and density: $P=P(\rho,T)$ and $\mu=\mu(\rho,T)$, where ρ is the density. The temperature in the water-CO2 mixture container is assumed to be constant (fluctuations around mean value 298 K) due to the Berendsen thermostat applied to that region. The density of CO2 in CO2layer was kept constant (not exactly constant but fluctuating around a mean value) by moving the moveable wall based on the mass flow rate conservation equation, given by equation (5.1). The result was actually very good. The density of CO2 in CO2layer was kept approximately constant on average for simulation 1-3, as seen in figure B.3 a)-c) in Appendix B. But, simulation 4 was very challenging, which can be seen from figure B.3 d), where the density decreases with simulation time. It could perhaps be due to a combination of a large (20,20) nanotube and a low density (which is more affected by the exchange of particles than high density regions). The challenge with simulation 4 can also be represented by figure B.2 d), showing how the z-position of the moveable wall changes with time. It can be observed that the wall fluctuates widely even though steady-state conditions seem to be reached according to the flux profile of CO2 molecules in the receiving tank in figure 7.15 d).

Another thing to notice about challenges with controlling the driving forces is that the 20 ns equilibration with blocked nanotube resulted in slightly different densities of CO2 in the CO2layer for the four simulations in part 2. From figure B.3, it can be seen that for simulation 1, the density is slightly higher than the density for simulation 2, both initial and average density. The same can be observed from simulation 3 and 4, where simulation 3 has a higher density than simulation 4, initially (and also mean value but the mean density of simulation 4 was too challenging to keep constant). An idea for a cause is related to the nanotube size. Both simulation 1 and 3 consist of a (10,10) nanotube. The (10,10) nanotube has a smaller radius than the (20,20) nanotube, and as seen from figure 7.11-7.14, the graphene walls at the nanotube entrance actually consist of more carbon atoms for the smaller (10,10) nanotube. As a result, it could be that the Lennar-Jones interaction field surrounded by the carbon atoms at the nanotube entrance is higher for the (10,10) nanotube simulations, leading to a higher density of CO2 in the CO2layer. A possible solution to the density differences could have been to e.g. increase the z-size of the water-CO2 mixture container for simulation 1 and 3 to have the same density for

simulation 1-2 and 3-4. But, it was prioritized to nothing about it because, firstly, it would have been very time consuming to fine-adjust the density, and secondly, a change in the z-size could affect the driving forces in a way that perhaps is not known. Instead, it was chosen to just keep the density of CO2 in CO2layer constant at the density obtained from the 20 ns equilibration with blocked nanotube. The code was written to keep the density constant, and so it did, at least for simulation 1-3. Again, this is another example of a constraint of the simulation system that makes it difficult to conclude which nanotube size that results in the best (greatest) number of CO2 molecules in receiving tank due to the small margin in results and overlapping, as seen with the flux curves in figure 7.16.

The second type of error can also be related to the graphene wall bias effect. The four graphene walls are present just to create a pressure and chemical gradient across the nanotube. But, in a real life experiment or an industrial use, they will likely not be present. However, the bias effect was significantly reduced by 1/10 tune down the graphene – water and grapene-CO2 interactions, as seen from figure 6.4-6.5.

7.2.5 Comparison with previous results

For simulation 1, a density of 680 kg/m^3 was used in the simulations of the pure CO2box without graphene walls as part of the thermodynamic integration. At 298K, the pair potential energy was measured to be -6.065 +- 0.008 kJ/mole. This result is in good correspondence with experimental results presented by Kuznetsova et al. [88]. They presented the potential energy of CO2 as liquid phase at 300 K to be about -7 kJ/mole.

The three principal moments of inertia values listed in table 7.5 are in excellent agreement with Huang & Pascal's calculated values [89]. Huang got moments of inertia values of $I_{xx}=I_{yy}\approx 43.04$ *(g/mole Å^2)*, $I_{zz}\approx 0$ *(g/mole Å^2)* for the EPM2 semiflexible model.

After conducting a literature search, it was not found any comparable CO2 fluxes through nanotube. However, a comparable water flux has been found in the literature. Wang [82] conducted a non-equilibrium MD study on pure water flow through a (12,12) carbon nanotube at a 50 bar pressure gradient and 300 K temperature, and obtained an estimate for water flux to be 1.784 ± 0.003 molecules/ns/nm^2. Fluxes calculated in this work (table 7.3) are on the same order of magnitude.

There is a lack of literature on the chemical potential of CO2 in nanotube, probably because it never has been calculated before. Therefore, the method to estimate the chemical potential of CO2 in nanotube presented in this master thesis can be considered as a pioneer work, and hence, it is difficult to compare with previous results.

Chapter 8 – Conclusions

In this work, a new CO2 capture technique has been proposed and numerically evaluated by means of nano scale methods. It presents a new approach for separating CO2 from flue gas involving the use of carbon nanotubes, or similar size channels of non-polar hydrocarbons for separating CO2 from CO2/water mix of finely distributed CO2 bubbles. The main goal of this project has been to evaluate the feasibility of separating CO2 from water using the nanotubes with classical Molecular Dynamics simulations as our scientific method of choice. The criteria for success of the concept are that the flow-through capacity in terms of flux should be high enough for realistic equipment sizes, and that the selectivity is sufficient.

A non-equilibrium MD set-up was constructed. It consisted of a water-CO2 mixture container consisting of various ratios of water and CO2 so as to imitate a distribution of CO2 bubbles and CO2 physically dissolved in water. This container was coupled to the second tank via a carbon nanotube, containing CO2 initially in gas phase. The whole system of the two containers and the connecting nanotube was thermostatted at 298 K, ensuring the absence of thermal gradient across the nanotube. The net remaining driving forces combined with first and second law of thermodynamics were therefore limited to mechanical and chemical work. Theoretically, this set-up would involve transport of CO2, and potentially some water, until the driving forces vanish, and a quasi-equilibrium between the receiving tank and the nanotube is established.

The simulations conducted in this project have been divided into two parts. The main goal with part 1 involved evaluating the nanotube selectivity and risk of water entrainment. The main goal with part 2 was to evaluate the nanotube capacity. Moreover, by conducting as many as four simulations in both parts (each with two extreme scenarios as independent variables), it was possible to discuss the trends and relative results, and also to have a wider understanding of the separation process.

8.1 Water/CO2 separation with carbon nanotubes

In part 1 of this project, a simulation system was designed to make it possible to evaluate the CO2 selectivity and risk of water entrainment as a function of nanotube size and initial pressure gradient across the nanotube. Systems investigated in part 1 all exhibited good selectivity and low water risk in the separation process. After analysis of the systems, it was found that the amount of excess CO2 molecules in the water bulk phase was a large contribution to the chemical driving force. An initial concentration of 10 mole% CO2 distributed in water (~10 times higher concentration of CO2 in water than its solubility limit), and after 30 ns of simulation time, the amount of excess CO2 in water

bulk dropped down to ~0.8 mole%. The flux profiles of CO2 in the receiving tank eventually flattened out, likely reflecting the decrease in excess CO2 molecules in water bulk (and also decrease in mechanical and chemical gradient across the nanotube). This result is very encouraging because it shows the strong chemical work available in the water-CO2 mixture with super-high amounts of excess CO2 distributed. The CO2 molecules showed strong preference for adsorption into the nanotubes compared to the water molecules due to strong water-water interactions (hydrogen bonds) and strong CO2-nanotube interactions.

A higher initial pressure gradient resulted in a higher flux of CO2 from the water-CO2 mixture and through the nanotube, but also a higher water entrainment risk. In both simulations involving (10,10) nanotube, a small water cluster entered receiving tank. For the two (20,20) nanotube simulations, the water cluster was never cut off by the carbon dioxide, it just filled the nanotube before retreating into the water-CO2 mixture, which in fact illustrates the strong preference for water to be surrounded by other hydrogen bonding water molecules.

8.2 Capacity of the carbon nanotubes

In part 2, the simulation system in part 1 was modified in order to utilize a new method (presented in this work) that made it possible to estimate the chemical potential of CO2 in nanotube. The system set-up in part 2 was successfully designed to find the desired quasi-equilibrium conditions between right-end nanotube and receiving tank as a function of nanotube size and driving forces in the water-CO2 mixture container. At this stage, there exist thermal, mechanical and chemical quasi-equilibria between the right end nanotube and the receiving tank, with no net flow of CO2 molecules in nanotube, making it possible to estimate chemical potential of CO2 in the nanotube.

The chemical potential of CO2 at the right hand side of nanotube (connected to receiving tank) was successfully estimated for the first time ever. It was equal to: -40.281 +- 0.008 kJ/mole (simulation 1), -40.240 +- 0.008 kJ/mole (simulation 2), -40.620 +- 0.002 kJ/mole (simulation 3) and -40.625 +- 0.009 (simulation 4). Simulation 1-2 were characterized by the high driving forces in the water-CO2 mixture container, while simulations 3-4 corresponded to low driving forces. The total chemical potentials are all approximately the same, even though simulation 1-2 achieved liquid CO2 density in receiving tank and simulation 3-4 achieved CO2 gas density in receiving tank. This is a very interesting result because it illustrates that CO2 molecules in nanotube are not particularly affected by external factors such as nanotube size and density in connecting tank.

The estimated chemical potentials are of high importance in the evaluation of the potential of nanotubes for separation of water and CO2 because it is a quantity that

describes the minimum work required to add one more CO2 molecule into the nanotube. For the separation process to happen, the chemical potential of CO2 in water-CO2 mixture must be higher than the chemical potential of CO2 in nanotube.

The peak CO2 flux through the nanotubes was estimated to be 4.20 +- 0.01 molecules/ns/nm^2 (simulation 1), 26.4 +- 0.1 molecules/ns/nm^2 simulation 2, 0.738 +- 0.001 molecules/ns/nm^2 (simulation 3) and 1.42 +- 0.01 molecules/ns/nm^2 (simulation 4). The calculated peak fluxes show that the two (20,20) nanotube simulations (simulation 2,4) have a much higher flux through the nanotube than the two (10,10) nanotubes (simulation 1,3). This could also be observed from the flux profiles of CO2 in receiving tank, where it can be observed that the two (20,20) nanotubes saturated the receiving tank much faster than the two (10,10) nanotubes. However, the two nanotube sizes, for same magnitude of driving forces in water-CO2 mixture container, yielded approximately the same amount of CO2 in receiving tank.

Yet another conclusion reached basing on the simulations in part 2 was that a higher driving force in the water-CO2 mixture container resulted in a much higher flux through the nanotube as well as dramatically higher number of CO2 molecules in the receiving tank. This is a very encouraging result because it shows the high potential (with high flux) of nanotube for the separation process if there is a high-density region of CO2 in the water-CO2 mixture near the nanotube entrance.

9 Suggestion for further work

The work done in this project should be considered a pioneer project where we have proposed and evaluated a novel technique to capture CO2, as well as a new approach to estimate the chemical potential of CO2 in nanotube. But, as in all projects, there are things that could have been done differently and more comprehensively.

9.1 Simulations in part 1

The goal of part 1 was to model a non-equilibrium set-up that made it possible to evaluate the selectivity and water entrainment risk as a function of nanotube size and initial pressure gradients across the nanotube. Below are some proposed suggestions for further work in connection with simulations conducted in part 1.

9.1.1 Graphene wall bias effect

The goal with this project was to get an overall view of the separation process. Therefore, there exist a number of improvements and factors that deserve a more comprehensive study which was not done because of time limitations. An example is the 1/10 scaling of the graphene walls Lennard-Jones interactions. The value of 1/10 was chosen simply because it gave a dramatic decrease in the adsorption effect of CO2. A further tune down, e.g. 1/15 or 1/20, or 1/11 for that case, was not tried because tuning the graphene wall interactions too much down could result in the CO2 molecules either being stuck in the wall or passing through it. A suggestion could be to investigate the graphene wall scaling more thoroughly to find a more physical graphene-CO2 and graphene-water interaction. Another possibility could be to try a wall of another type.

Even though the interactions with graphene walls were scaled by the factor of 1/10, there existed a wall at the nanotube entrances which led to CO2 enrichment near the graphene walls for the excess CO2 molecules in water. This bias could possibly affect the separation process. But still, since water has shown a strong tendency to compress itself into a hydrogen bonding water block, it will tend to push the excess CO2 molecules out of the water mixture. A suggestion to further work could be to develop a simulation system that does not require graphene walls at all.

9.1.2 Intermolecular interaction potentials of unlike molecules

In this project, the Lorentz-Berthelot mixing rules have been used to calculate the graphene-water and graphene-CO2 interactions due to the lack of a force field specifically parameterized to describe the interactions. A model that described the graphene-water interaction was found, and it has shown good abilities for reproducing the contact angle of water on the hydrophobic graphene surface [90]. A similar model for CO2 does not exist to the best of our knowledge, hence the mixing rule was used for both water and CO2 interactions with nanotube. A further step in the investigation of this new method to capture CO2 could be to develop a model for both water and CO2 that can reproduce their experimental interactions with nanotube. This could give an even further realistic picture of the separation process. The mixing rules were also used for water-CO2 interactions. Nevertheless, based on the simulation results, the behavior of water-CO2 mixture appeared to be reasonable judging by phase separation and equilibrium concentration of CO2 in water. But, it would perhaps have been even better to develop a water-CO2 interaction model tested to a greater extent to reproduce the experimental data.

9.1.3 Initial start configuration of water/CO2 molecules

The initial start configuration for the water and CO2 molecules in the water-CO2 mixture container was highly unphysical for all the four simulations evaluated in part 1. The molecules were packed randomly in Packmol so that they were evenly distribution to mitigate an initial start configuration bias. A suggestion for further work would be to find a configuration that could describe a real, non-equilibrium water/CO2 mixture. Preferably, the venture nozzle hydrodynamic effect should also be included. Initializing all the simulations from several random initial start configurations, to see if the final state (the result) is the same would improve the statistics.

9.1.3 Pressure sampling

An accurate evaluation of pressure has not been done in this research project. As previously discussed, there were some challenges in controlling the pressure of the non-homogeneous, non-equilibrium water-CO2 mixture. It would be very instructive to find a way to control the pressure of the water-CO2 mixture. Also, it is necessary to do more research on what is a realistic volume of the 10 mole% CO2 in water-CO2 mixture. It could also be beneficial to perform a study on the optimal pressure and temperature for the nanotube separation process.

9.1.5 Reaction kinetics

The reaction of water and CO2 that produces carbonic acid (H_2CO_3) has been neglected in this work but might be important and therefore should be included.

9.2 Simulations in part 2

The goal of simulation conducted in part 2 was to evaluate the nanotube capacity in terms of flux and chemical potential. The flux was quantified by measuring the number of CO2 molecules in the receiving tank as a function of time. The chemical potential of CO2 in the nanotube was estimated by assuming that thermal, mechanical work and chemical gradients must vanish when a quasi-equilibrium between right-end nanotube and receiving tank has been established. This section presents suggestions for further work with regards to simulations conducted in part 2.

9.2.1 Controlling the driving forces

An enormously important part of this research project has been to design a system that made it possible to keep the driving forces in the water-CO2 mixture constant on average, so that the desired quasi-equilibrium conditions could be reached. A basic mass flow rate conservation was used to calculate the velocity of the moveable wall to keep the density of CO2 in the CO2layer control region roughly constant. As previously discussed, this method gave very promising result for simulations 1-3. Simulation 4, however, has proven much more challenging to control, likely due to CO2 gas density and the large diameter of (20,20) nanotube. Therefore, a suggestion for further work would be to improve this method to achieve better control of the driving forces.

9.2.2 Free energy calculations

Thermodynamic integration method was used to calculate the residual chemical potential of a pure box of CO2 molecules for different densities at 298 K. It would have been instructive to compare the results by using another method to calculate the residual chemical potential of a pure box of CO2, e.g. Widom particle insertion method or the Adaptive Biasing Force (ABF).

9.2.3 Longer nanotubes

Both for part 1 and 2, it would have been quite informative to use longer nanotube to probe the possible impact on selectivity, water risk, and capacity.

9.2.4 Relate the simulation results more to current CO2 capture technologies

The final suggestion for further work would be to evaluate the energy efficiency and give cost estimates for the new method of CO2 capture presented in this master thesis. It is important to discuss how efficient the nanotube separation process is compared to the current CO2 capture technologies, like the use of zeolites and amines. This aspect was not prioritized because the main goal was to evaluate the potential of nanotube separation of water and CO2 by conducting molecular dynamics simulations and to investigate how

different independent variables (extreme points) will affect the separation process. In addition, this new concept for CO2 capture is in its very early pioneer stage.

References

[1] Dagens Næringsliv. *Verden tørster etter mer olje.* 23 March 2018. nr. 70. p. 16-17.

[2] REN21. *Renewables 2017 Global Status Report.* 2017. URL: http://www.ren21.net/wp-content/uploads/2017/06/17-8399_GSR_2017_Full_Report_0621_Opt.pdf

[3] Raul Barreto. *Fossil Fuels, Alternative Energy and Economic Growth.* 2014. URL: https://economics.adelaide.edu.au/research/papers/doc/wp2014-03.pdf

[4] British Petroleum. *BP Statistical Review of World Energy 2017.* 2017. URL: https://www.bp.com/content/dam/bp/en/corporate/pdf/energy-economics/statistical-review-2017/bp-statistical-review-of-world-energy-2017-full-report.pdf

[5] Winnie Courtene-Jones et al. *Microplastic pollution identified in deep-sea water and ingested by benthic invertebrates in the Rockall Trough, North Atlantic Ocean.* 2017. URL: https://www.sciencedirect.com/science/article/pii/S0269749117312885

[6] Jane Dignon, *NOx and SOx emissions from fossil fuels: A global distribution*. 1991. URL: https://www.sciencedirect.com/science/article/pii/096016869290047O

[7] Sultan Hameed and Jane Dignon. "*Global Emissions of Nitrogen and Sulfur Oxides in Fossil Fuel Combustion 1970–1986*". 2012. URL: https://www.tandfonline.com/doi/pdf/10.1080/10473289.1992.10466978

[8] Camille Parmesan and Gary Yohe. *A globally coherent fingerprint of climate change impacts across natural systems*. 2003. URL: https://www.nature.com/articles/nature01286.pdf

[9] Mark Jacobson. *On the causal link between carbon dioxide and air pollution mortality*. 2007. URL: https://agupubs.onlinelibrary.wiley.com/doi/epdf/10.1029/2007GL031101

[10] Stephanie Waldoff et al. *The Marginal Damage Costs of Different Greenhouse Gases: An Application of FUND*. 2014. URL: http://www.economics-ejournal.org/economics/discussionpapers/2011-43/file

[11] Myles Allen and Thomas Stocker. *Impact of delay in reducing carbon dioxide emissions*. 2013. URL: https://www.nature.com/articles/nclimate2077.pdf

[12] European Commision. *Paris Agreement 2015*. URL: https://ec.europa.eu/clima/policies/international/negotiations/paris_en#tab-0-0

[13] Zhong-Xiang Zhang et al. *The withdrawal of the U.S. from the Paris Agreement and its impact on global climate change governance*. 2017. URL: https://www.sciencedirect.com/science/article/pii/S1674927817300849

[14] Norsk Petroleum. *Carbon Capture and Storage*. URL: https://www.norskpetroleum.no/en/environment-and-technology/carbon-capture%20and-storage/

[15] Equinor (Statoil). *Carbon Capture and Storage*. URL: https://www.equinor.com/en/how-and-why/climate-change/carbon-storage.html

[16] NERC. *Removal of CO2 from natural gas processing plant*. 2017. URL: http://www.bgs.ac.uk/discoveringGeology/climateChange/CCS/RemovalCO2NaturalGas.html

[17] Hossein Dashti. *Recent advances in gas hydrate-based CO2 capture*. 2014. URL: https://www.sciencedirect.com/science/article/pii/S1875510015000438

[18] Yangyang Lie and Jennifer Wilcox. *CO2 Adsorption on Carbon Models of Organic Constituents of Gas Shale and Coal*. 2010. URL: https://pubs.acs.org/doi/pdf/10.1021/es102700c

[19] Dennis Leung et al. *An overview of current status of carbon dioxide capture and storage technologies*. 2014. URL: https://www.sciencedirect.com/science/article/pii/S1364032114005450

[20] Christina Quintella et al. *CO2 Capture Technologies: an Overview with Technology Assessment Based on Patents and Articles*. 2011. URL: https://www.sciencedirect.com/science/article/pii/S1876610211002840

[21] APEC Energy Working Group. *Building Capacity for CO2 capture and Storage in the APEC Region - A training manual for policy makers and practitioners* . 2009.

[22] Lei Li et al. *A review of research progress on CO2 capture, storage, and utilization in Chinese Academy of Sciences*. 2011. URL: https://www.sciencedirect.com/science/article/pii/S0016236111004807

[23] Intergovermental Panel on Climate Change (IPCC). *IPCC Special Report on Carbon Dioxide Capture and Storage*. 2005. URL: https://www.ipcc.ch/pdf/special-reports/srccs/srccs_wholereport.pdf

[24] EPRI. *Retrofitting CO2 Capture*. 2009. URL: http://eprijournal.com/wp-content/uploads/2016/02/2009-Journal-No.-2.pdf

[25] Anand Rao et. al. *Details of A Technical, Economic and Environmental Assessment of Amine-based CO2 Capture Technology for Power Plant Greenhouse Gas Control*. 2002. URL: https://pubs.acs.org/doi/10.1021/es0158861

[26] Global CCS Institute. *Module 2 CO2 capture: Post-combustion flue gas separation*. URL: http://hub.globalccsinstitute.com/publications/building-capacity-co2-capture-and-storage-apec-region-training-manual-policy-makers-and-practitioners/module-2-co2-capture-post-combustion-flue-gas-separation#fn_4

[27] Gassnova. *What is CO2 capture?*. 2017. URL: https://www.gassnova.no/en/facts-ccs/what-is-co2-capture

[28] José Figueroa et al. *Advances in CO2 capture technology – The U.S. Department of Energy's Carbon Sequestration Program*. 2008. URL: https://www.sciencedirect.com/science/article/pii/S1750583607000941

[29] Daniel Jansen. *Pre-combustion CO2 capture*. 2015. URL: https://www.sciencedirect.com/science/article/pii/S1750583615001917

[30] Ahmad Ismail et al. *Gas Separation Membranes*. 2015. Page 95. URL: https://link.springer.com/content/pdf/10.1007%2F978-3-319-01095-3.pdf

[31] S Chen. *Using 13X, LiX, and LiPdAgX zeolites for CO2 capture from post-combustion flue gas*. 2017. URL: https://www.sciencedirect.com/science/article/pii/S0306261917300399

[32] P Jadhav et al. *Monoethanol Amine Modified Zeolite 13X for CO2 Adsorption at Different Temperatures*. 2007. URL: https://pubs.acs.org/doi/pdf/10.1021/ef070038y

[33] Lang Liu and Suresh Bhatia. *Molecular Simulation of CO2 Adsorption in the Presence of Water in Single-Walled Carbon Nanotubes*. 2013. URL: https://pubs.acs.org/doi/pdf/10.1021/jp403477y

[34] Spycher and Pruess. *CO2-H2O mixtures in the geological sequestration of CO2. I. Assessment and calculation of mutual solubilities from 12 to 100°C and up to 600 bar*. 2003. URL: https://www.sciencedirect.com/science/article/pii/S0016703703002734

[35] Jonhoo Lee and N Aluru. *Water-solubility-driven separation of gases using graphene membrane*. 2012. URL: https://webhost.engr.illinois.edu/~aluru/Journals/JMS13.pdf

[36] LAMMPS simulation software progam. *LAMMPS Users Manual*. 2003. 11 May 2018 version. URL: http://lammps.sandia.gov/doc/Manual.pdf

[37] Claus Borgnakke and Richard Sonntag. *Fundamentals of Thermodynamics – SI Version*. Page 6-7. Eight edition. University of Michigan. WILEY. 2014.

[38] Daan Frenkel and Berend Smit. *Understanding Molecular Simulation – From Algorithm to Applications*. Page 167-200, 291-320. Second edition. University of Amsterdam. ACADEMIC PRESS – An Imprint of Elsevier. 1996.

[39] University of California, Santa Barbara: M Shell. *Other free energy techniques*. 2012. URL: https://engineering.ucsb.edu/~shell/che210d/Other_free_energy_techniques.pdf

[40] Harvey Gould and Jan Tobochnik. *The Chemical Potential and Phase Equilibria*. 2009. Clark University. URL: http://stp.clarku.edu/notes/chap7.pdf

[41] University of Oslo (UiO). *Gibbs' phase rule*. URL: http://kj-gibbs.uio.no/phase_rule.html

[42] Mark E. Tuckerman. *Statistical Mechanics: Theory and Molecular Simulation*. 2010. Oxford Graduate Texts. Page 136-138. URL: http://www.nanophysics.pl/3books/Books/Statistical_Mechanics.pdf

[43] Michael Allen. *Introduction to Molecular Dynamics Simulation*. 2004. URL: https://udel.edu/~arthij/MD.pdf

[44] Bjørnar Jensen. *Investigation into impact of solid surfaces in aqueous* systems. PhD at the University of Bergen. 2016. Page 18-19, 23, 28-30. URL:

[45] Tatyana Kuznetsova. *Molecular modeling for thermodynamic properties of bulk and interfacial systems*. University of Bergen, Norway. 2001.

[46] J. W. Eastwood and R. W. Hockney. *P3M3DP—The three-dimensional periodic particle-particle/ particle-mesh program*. 1980. URL: https://www.sciencedirect.com/science/article/pii/0010465580900521

[47] Block Luty and Wilfred Gunsteren. *Calculating Electrostatic Interactions Using the Particle-Particle Particle-Mesh Method with Nonperiodic Long-Range Interactions*. 1995. URL: https://pubs.acs.org/doi/pdfplus/10.1021/jp9518623?src=recsys

[48] H Berendsen. *Molecular dynamics with coupling to an external bath*. 1984. URL: https://aip.scitation.org/doi/pdf/10.1063/1.448118

[49] Philippe Hünenberger. *Thermostat Algorithms for Molecular Dynamics Simulations*. 2005. URL: https://pdfs.semanticscholar.org/0e83/4dcac5bfdf91a0b0b7fa5488e9324a1d51d5.pdf

[50] Birgit Strodel (Computational Biochemistry Group). *Simulation of Biomolecules*. URL: http://www.strodel.info/lecture3.pdf

[51] Suichi Nosé. *A unified formulation of the constant temperature molecular dynamics methods*. 1984. URL: https://aip.scitation.org/doi/pdf/10.1063/1.447334

[52] William Hoover. *Canonical dynamics: Equilibrium phase-space distributions*. 1984. URL: https://journals.aps.org/pra/pdf/10.1103/PhysRevA.31.1695

[53] Nicholas Spycher et al. *CO2-H2O mixtures in the geological sequestration of CO2. I. Assessment and calculation of mutual solubilities from 12 to 100°C and up to 600 bar*. 2003.URL: https://www.sciencedirect.com/science/article/pii/S0016703703002734

[54] Lars Øi. *Aspen HYSYS Simulation of CO2 Removal by Amine Absorption from a Gas Based Power Plant*. 2007. URL: https://www.ep.liu.se/ecp/027/008/ecp072708.pdf

[55] ProSim. CO2 capture using amine solution. 2017. URL: http://www.prosim.net/bibliotheque/File/Exemples-Applications-PSP/En/PSPS_E19_EN-CO2_capture-with-amine-process.pdf

[56] Haining Zhao. *Web computational tool used to calculate CO2 properties*. Updated: April, 2015. URL: http://www.energy.psu.edu/tools/CO2-EOS/

[57] Roland Span and Wolfgang Wagner. *A New Equation of State for Carbon Dioxide Covering the Fluid Region from the Triple-Point Temperature to 1100 K at Pressures up to 800 MPa*. 1996. URL: https://aip.scitation.org/doi/pdf/10.1063/1.555991

[58] L Martínes et al. *Packmol: A Package for Building Initial Configurations for Molecular Dynamics Simulations*. 2008. URL: http://m3g.iqm.unicamp.br/packmol/packmol2.pdf

[59] Jonathan Harris and Kwong Yung. *Carbon Dioxide's Liquid-Vapor Coexistence Curve and Critical Properties As Predicted by a Simple Molecular Model*. 1995. URL: https://pubs.acs.org/doi/pdf/10.1021/j100031a034

[60] Yang Liu et al. *Simulations of Vapor–Liquid Phase Equilibrium and Interfacial Tension in the CO2–H2O–NaCl System*. 2013. URL: https://onlinelibrary.wiley.com/doi/pdf/10.1002/aic.14042

[61] Yangyang Liu and Jennifer Wilcox. *Molecular Simulation Studies of CO 2 Adsorption by Carbon Model Compounds for Carbon Capture and Sequestration Applications*. 2012. URL: https://pubs.acs.org/doi/pdf/10.1021/es3012029

[62] William Humphrey. *VMD: Visual Molecular Dynamics*. 1996. URL: https://www.sciencedirect.com/science/article/pii/0263785596000185

[63] Yujie Wu et al. *Flexible simple point-charge water model with improved liquid-state properties*. 2006. URL: https://aip.scitation.org/doi/pdf/10.1063/1.2136877

[64] Kahled Toukan and Aneesur Rahman. *Molecular Dynamics Simulation of atomic motions in water*. 1984. URL: https://journals.aps.org/prb/pdf/10.1103/PhysRevB.31.2643

[65] Francesco Paesani et al. *An accurate and simple quantum model for liquid water*. 2006. URL: https://aip.scitation.org/doi/pdf/10.1063/1.2386157

[66] Melissa Paradise and Tarun Goswami. *Carbon nanotubes – Production and industrial applications*. 2006. URL: https://www.sciencedirect.com/science/article/pii/S0261306906000914

[67] International Balzan Price Foundation. *Sumio Iijima*. 2007. URL: http://www.balzan.org/en/prizewinners/sumio-iijima/the-discovery-of-carbon-nanotubes-iijima

[68] A Abramyan et al. *Influence of liquid environment and bounding wall structure on fluid flow through carbon nanotubes*. 2015. URL: https://www.sciencedirect.com/science/article/pii/S0375960115002352

[69] Teka Talukdar and Apurba Mitra. *A molecular dynamics simulation study for the mechanical properties of different types of carbon nanotubes*. 2012. URL: https://link.springer.com/content/pdf/10.1007%2Fs13204-012-0110-z.pdf

[70] Irina Zaporotzkova et al. *Carbon nanotubes: Sensor properties. A review*. 2016. URL: https://www.sciencedirect.com/science/article/pii/S2452177917300178

[71] Rasel Das. *Carbon nanotube membranes for water purification: A bright future in water desalination*. 2013. URL: https://www.sciencedirect.com/science/article/pii/S0011916413006127

[72] Yangyang Liu and Jennifer Wilcox. *Molecular Simulation Studies of CO2 Adsorption by Carbon Model Compounds for Carbon Capture and Sequestration Applications*. 2012. URL: https://pubs.acs.org/doi/pdf/10.1021/es3012029

[73] Tina Duren. *Composition dependent transport diffusion coecients of CH4=CF4 mixtures in carbon nanotubes by non-equilibrium molecular dynamics simulations*. 2001. URL: https://www.sciencedirect.com/science/article/pii/S0009250902000441

[74] John Brodholt and Bernard Wood. *Molecular dynamics simulations of the properties of CO2-H2O mixtures at high pressures and temperature*. 1993. URL: http://www.minsocam.org/ammin/AM78/AM78_558.pdf

[75] Dezso Boda and Douglas Henderson. *The effects of deviations from Lorentz–Berthelot rules on the properties of a simple mixture*. 2008. URL: https://www.tandfonline.com/doi/pdf/10.1080/00268970802471137?needAccess=true

[76] Jian Chen. *Comparison of different mixing rules for prediction of density and residual internal energy of binary and ternary Lennard–Jones mixtures*. 2000. URL: http://www.cie.unam.mx/~mlh/documentos/Miguel/mixingrules2.pdf

[77] Andrew Jewett. *Moltemplate Manual*. 2017. URL: http://www.moltemplate.org/doc/moltemplate_manual.pdf

[78] University of Helsinki. *Statistical errors – block average method*. URL: http://www.courses.physics.helsinki.fi/fys/moldyn/lectures/L6.pdf

[79] Andrew Dalke and Axel Kahlmeyer. *Molecular trajectory path script for VMD*. University of Illinois Urbana-Champaign/University of Pennsylvania. URL: http://www.ks.uiuc.edu/Research/vmd/script_library/scripts/trajectory_path/

[80] M Gordillo. *Hydrogen bond structure of liquid water confined in nanotubes*. 2000. URL:https://www.sciencedirect.com/science/article/abs/pii/S0009261400010320

[81] Luying Wang et al. *Nonequilibrium molecular dynamics simulation of water transport through carbon nanotube membranes at low pressure*. 2012. URL: https://aip.scitation.org/doi/pdf/10.1063/1.4734484

[82] Luying Wang. *Molecular Dynamics Simulations of Liquid Transport through nanofiltration membranes*. 2012. URL: https://macsphere.mcmaster.ca/bitstream/11375/12488/1/fulltext.pdf

[83] Sony Joseph and N Aluru. *Why Are Carbon Nanotubes Fast Transporters of Water?*. 2007. URL: https://pubs.acs.org/doi/pdf/10.1021/nl072385q

[84] Joonho Lee and N Aluru. *Separation of gases from gas–water mixtures using carbon nanotubes*. 2009. URL: https://web.engr.illinois.edu/~aluru/Journals/APL10-1.pdf

[85] M Whitby and N Quirke. *Fluid flow in carbon nanotubes and nanopipes*. 2007. URL: https://www.nature.com/articles/nnano.2006.175

[86] Lang Liu and Suresh Bhatia. *Molecular Simulation of CO2 Adsorption in the Presence of Water in Single-Walled Carbon Nanotubes*. 2013. URL: https://pubs.acs.org/doi/pdf/10.1021/jp403477y

[87] Anastasios Skoulidas. *Rapid Transport of Gases in Carbon Nanotubes*. 2002. https://journals.aps.org/prl/pdf/10.1103/PhysRevLett.89.185901

[88] Tatyana Kuznetsova and Bjørn Kvamme. *Viability of Atomistic Potetnials for Thermodynamic Properties of Carbon Dioxide at Low Temperature*. 2001. URL: https://onlinelibrary.wiley.com/doi/epdf/10.1002/jcc.1130

[89] Shao-Nung Huang and Pascal. *Absolute Entropy and Energy of Carbon Dioxide Using the Two-Phase Thermodynamic Model*. 2011. URL: http://www.wag.caltech.edu/publications/sup/pdf/929.pdf

[90] Yanbin Wu and N Aluru. *Graphitic Carbon−Water Nonbonded Interaction Parameters*. 2013. URL: https://pubs.acs.org/doi/pdf/10.1021/jp402051t

Appendix A

Appendix A includes supplementary plots used in the discussion and evaluation of CO2 selectivity and water risk for the separation process with nanotube (part 1 of this work).

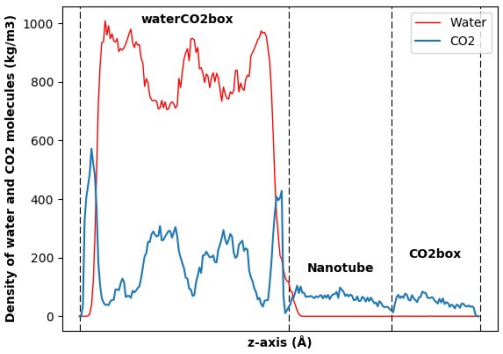

a) 0.4 ns (simulation 2)

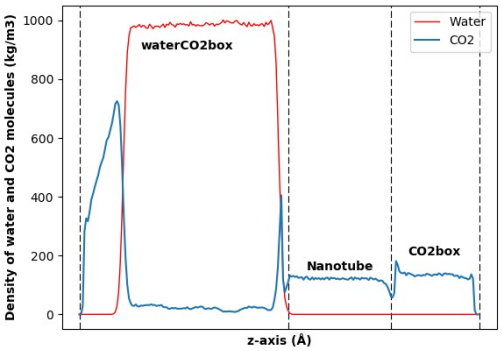

b) 30 ns (simulation 2)

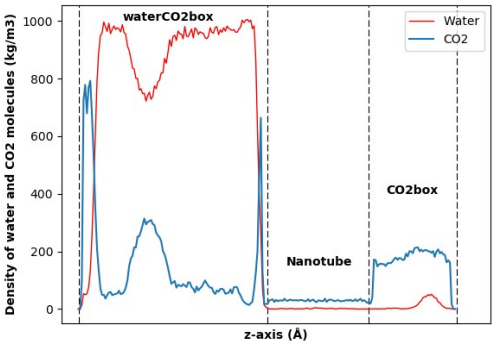

a) 0.4 ns (simulation 3)

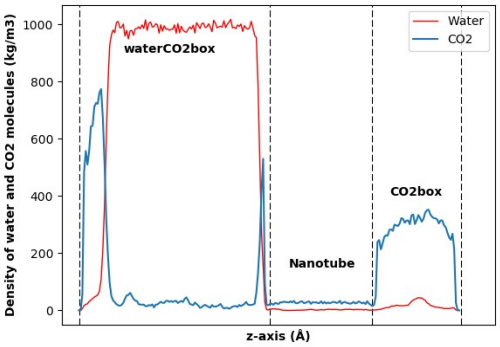

b) 30 ns (simulation 3)

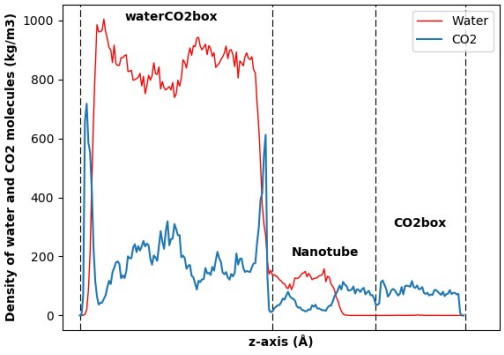

a) 0.4 ns (simulation 4)

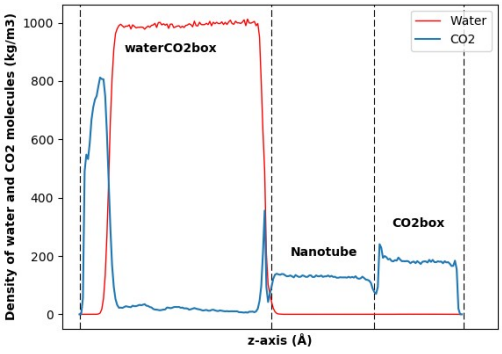

b) 30 ns (simulation 4)

Figure A.1: Density profile of water and CO2 for the whole system for the simulation 2-4 in part 1.

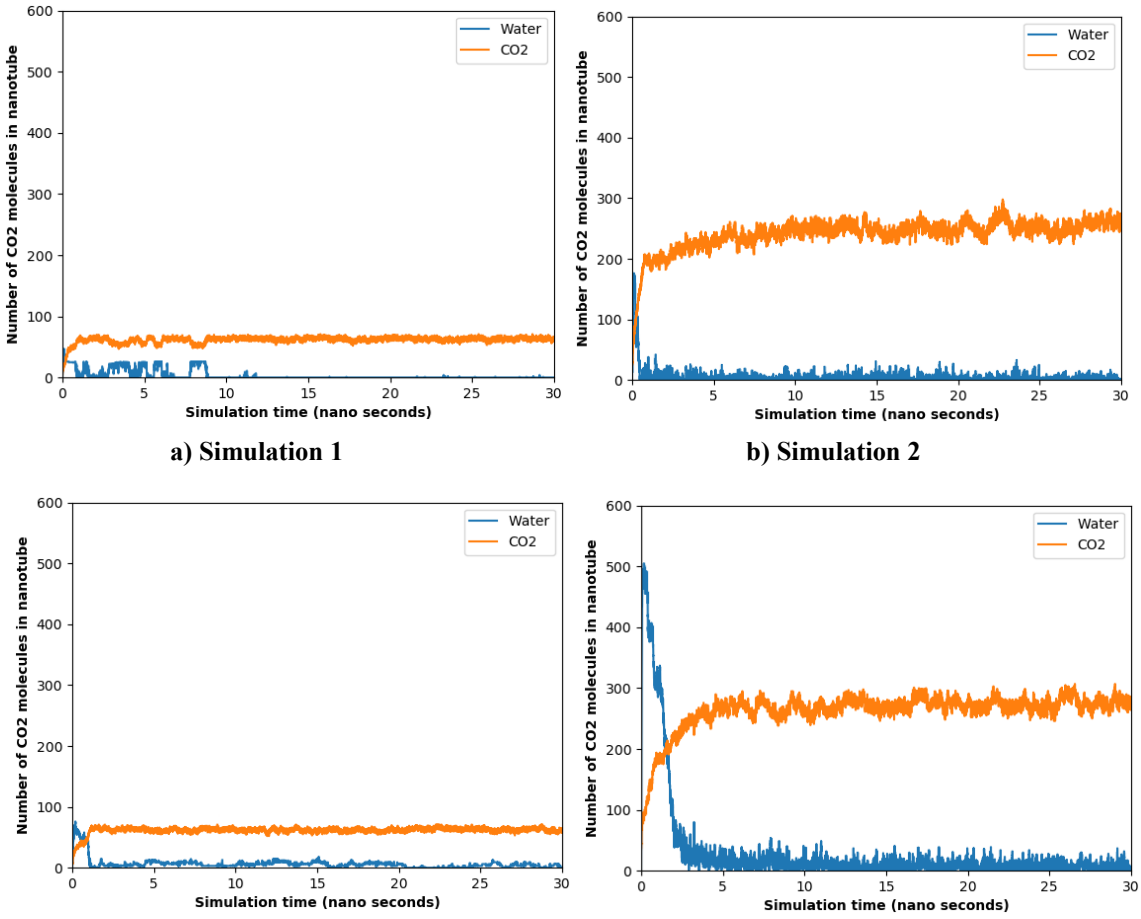

a) Simulation 1 **b) Simulation 2**

c) Simulation 3 **d) Simulation 4**

Figure A.2: Water/CO2 flux profiles in nanotube.

Appendix B

Appendix B comprises supplementary plots and tables used in the discussion and evaluation of capacity of nanotubes (part 2 of this work).

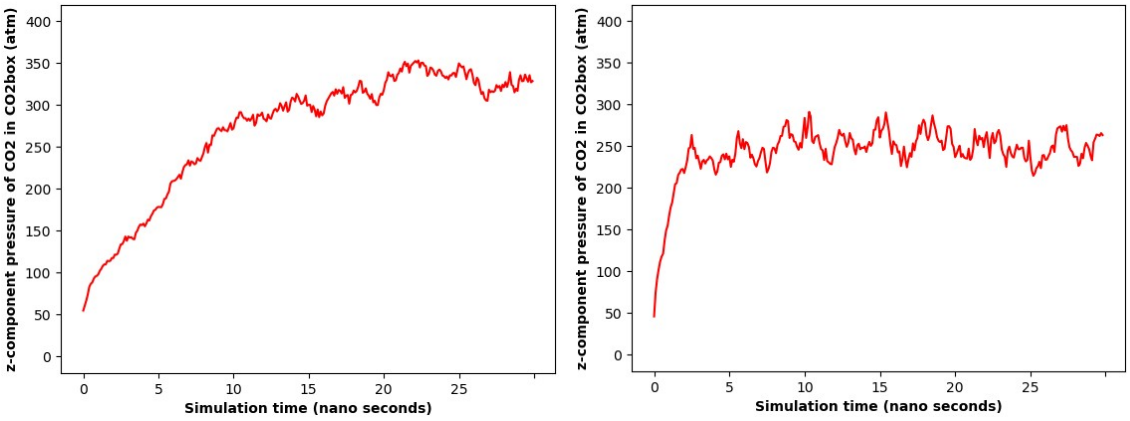

a) Simulation 1 **b) Simulation 2**

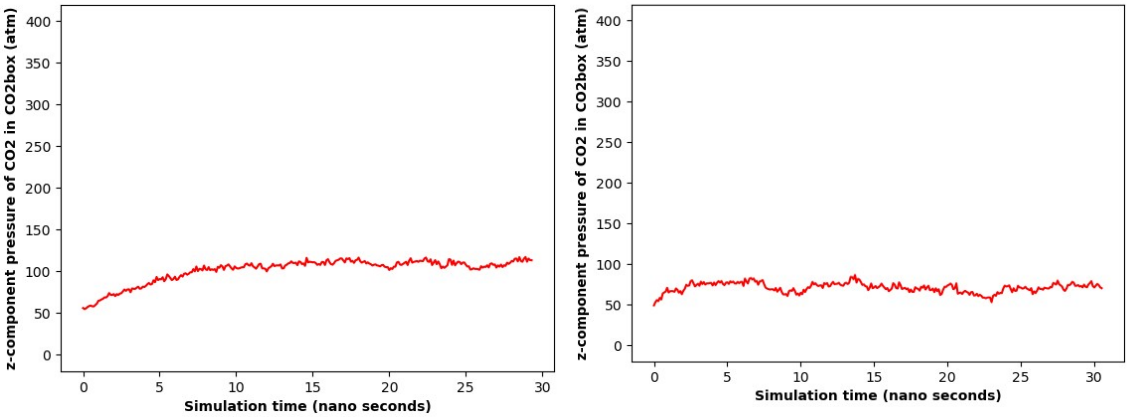

a) Simulation 3 **b) Simulation 4**

Figure B.1: Pressure profile of CO2 in receiving tank for the four simulations in part 2.

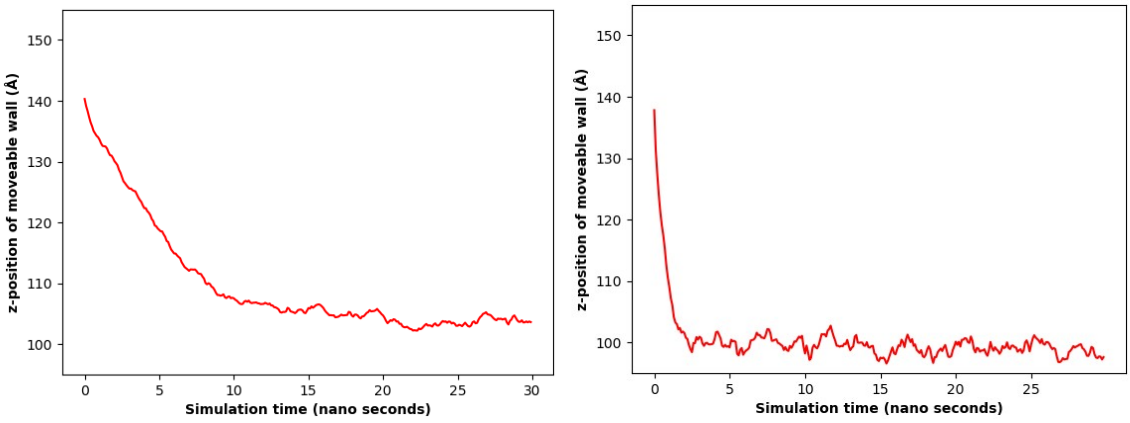

a) Simulation 1 **b) Simulation 2**

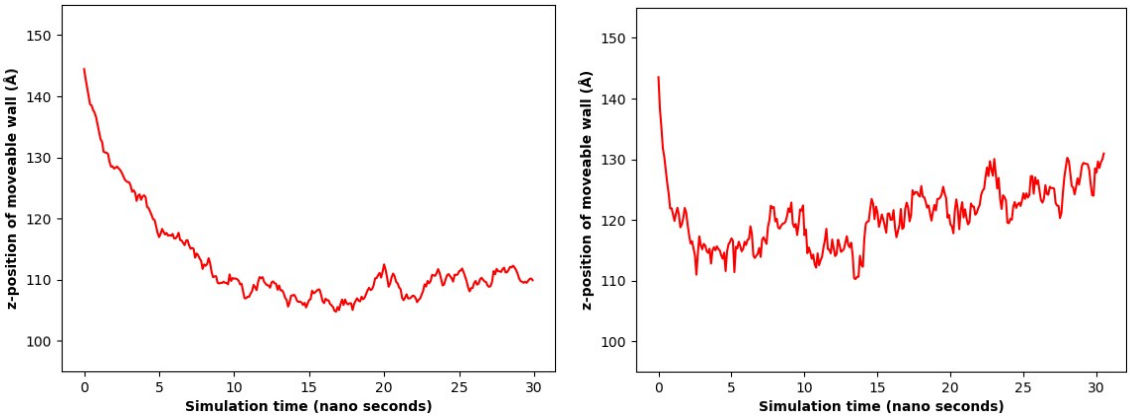

a) Simulation 3 **b) Simulation 4**

Figure B.2: z-position of the moveable wall vs time for all the four simulations in part 2.

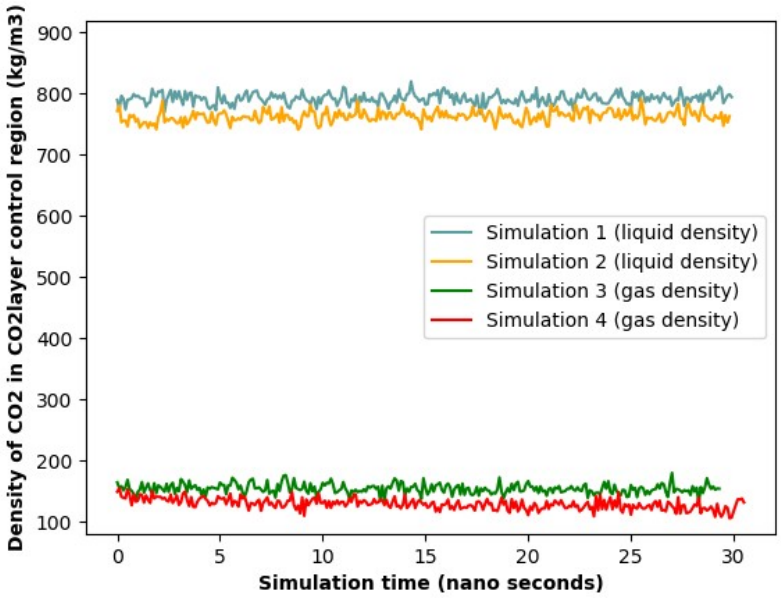

Figure B.3: Density of the CO2 molecules in the CO2layer control region in the water-CO2 mixture container for the four simulations in part 2.

Table B.1: Measured temperature and potential pair energy for simulation of box with pure CO2. Simulation 1 in part 2.

Thermostat temperature (K)	Temperature (K) with relative uncertainty	Pair potential energy (kJ/mole) with absolute uncertainty	Pair potential energy (kJ/mole) with relative uncertainty
298	298.00 +- 0.03%	-6.065 +- 0.008	-6.065 +- 0.1%
331	330.99 +- 0.02%	-5.883 +- 0.007	-5.883 +- 0.1%
...	...	...	...
1490	1490.0 +- 0.02%	-3.301 +- 0.007	-3.301 +- 0.2%
2980	2980.0 +- 0.02%	-1.075 +- 0.009	-1.075 +- 1%

Table B.2: Measured temperature and potential pair energy for simulation of box with pure CO2. Simulation 4 in part 2.

Thermostat temperature (K)	Temperature (K) with relative uncertainty	Pair potential energy (kJ/mole) with absolute uncertainty	Pair potential energy (kJ/mole) with relative uncertainty
298	298.0 +- 0.03%	-1.346 +- 0.009	-1.346 +- 1%
331	330.9 +- 0.03%	-1.271 +- 0.009	-1.271 +- 0.9%
...	...	...	...
1490	1489.9 +- 0.02%	-0.706 +- 0.005	-0.706 +- 0.3%
2980	2979.9 +- 0.02%	-0.373 +- 0.008	-0.373 +- 0.3%

Appendix C

Appendix C includes the Fortran 95 code used to calculate the ideal gas chemical potential for simulations 1-4 in part 2. It was made and provided by the Thermodynamic Modelling research group – Separation, Process Technology at the University of Bergen. The input values are temperature and density because chemical potential is a function of temperature and density. The moments of inertia for a linear CO2 molecule was used, calculated using the 1.149 Å C-O bond length of the EPM2 CO2 model.

```
      program chepotIDGAS
      IMPLICIT REAL*8(A-H,O-Z)
      T=298
      dens=188
      call CO2idr(T,dens,cp)
      WRITE(6,15) temp,dens,cp
15     FORMAT(1X,'TOTAL CHEM.POT. of CO2 at ',F10.3,'K and ',F10.3
     X ,' kg/m^3 =',F10.6,' kJ/mol')
      end

      subroutine CO2idr(temp,dens,cp)
      IMPLICIT REAL*8(A-H,O-Z)
      real*8 kb,qid,ugut
      data hcp/6.626D-34/ ! Heisenberg constant
      DATA anum/6.0225d23/ ! Avogadro number
      common/fucom/fugsat,fugp,psatco,poynt,yco2
      common/ygacom/ygas(65)
      common/comcom/compr03,compr53
      common/ccomp/comprs,compr
      common/tcom/T,P,S,xvec(75),ncomp,id(75),denliq,fmw,dmolek

      pi=3.14159d0
      kb=1.3806d-23 ! Boltzmann's constant
      anm=anum**(1.d0/3.0d0)
      hpcc=anum*hcp
      gc=8.3143d0 ! Gas constant (R)
      rt=gc*temp ! RT
      bkt = kb*temp  !kT
      ws=44.0d-03   ! molar mass of CO2 in kg
      amss=ws/anum ! molecular mass

      qid=hcp*hcp
      qid=qid/(2.0d0*pi*amss*kb*temp)
      qid1=qid**0.5
      qid=qid1*qid1*qid1
      qid=qid*dens/amss
      cid=-rt*dlog(qid)/1000.
```

```
      WRITE(6,*) temp,-cid
15    FORMAT(1X,'IDEAL TRAN.CHEM.POT. of CO2 at ',F10.3,'K ='
     X,F10.6,' kJ/mol')
      cidr=0.0d0

C Following is the CO2 inertia tensor
C This first is for a angle flexible CO2 model
C We do not use that now and jump to 47
      go to 47

      FIxx =7.0140d-46
      FIyy =7.0136d-46
      FIzz =3.9854d-50

      FIxx=FIxx*anum
      qidxx=(fll/Fixx)**0.5d0
      FIyy=FIyy*anum
      qidyy=(fll/FIyy)**0.5d0
      FIzz=FIzz*anum
      qidzz=(fll/FIzz)**0.5d0
      qidzz=1.0d0
      qid=qidxx*qidyy*qidzz
      qid=((qidxx*qidyy*qidzz)/dsqrt(PI))

C Following is the CO2 inertia tensor for linear CO2 molecule
47    continue

      FI =7.0153d-46

      FI=FI*anum
      fll=hpcc*hpcc/(pi**2*rt)
      qid=fll/FI
      cidr=0.0d0
      cidr=-rt*dlog(qid)/1000.
      cidr=-rt*dlog(qid)/1000.
      WRITE(6,5) temp,-cidr
5     FORMAT(1X,'IDEAL ROT.CHEM.POT. of CO2 at  ',F10.3,'K ='
     X,F10.6,' kJ/mol')

676   continue
      cp=cid+cidr
      cp=-cp
      return
      END
```